Novel Applications of Buffer-Gas Cooling to Cold Atoms, Diatomic Molecules, and Large Molecules

Novel Applications of Buffer-gas Cooling to Cold Atoms, Diatomic Molecules, and Large Molecules

A dissertation presented

by

Garrett Korda Drayna

to

The Department of Chemistry and Chemical Biology

in partial fulfillment of the requirements

for the degree of

Doctor of Philosophy

in the subject of

Chemical Physics

Harvard University

Cambridge, Massachusetts

January 2016

Dissertation Advisor: John Morrissey Doyle Author: Garrett Korda Drayna

Novel Applications of Buffer-gas Cooling to Cold Atoms, Diatomic Molecules, and Large Molecules

Abstract

Cold gases of atoms and molecules provide a system for the exploration of a diverse set of physical phenomena. For example, cold gasses of magnetically and electrically polar atoms and molecules are ideal systems for quantum simulation and quantum computation experiments, and cold gasses of large polar molecules allow for novel spectroscopic techniques. Buffer-gas cooling is a robust and widely applicable method for cooling atoms and molecules to temperatures of approximately 1 Kelvin. In this thesis, I present novel applications of buffer-gas cooling to obtaining gases of trapped, ultracold atoms and diatomic molecules, as well as the study of the cooling of large organic molecules. In the first experiment of this thesis, a buffer-gas beam source of atoms is used to directly load a magneto-optical trap. Due to the versatility of the buffer-gas beam source, we obtain trapped, sub-milliKelvin gases of four different lanthanide species using the same experimental apparatus. In the second experiment of this thesis, a buffer-gas beam is used as the initial stage of an experiment to directly laser cool and magneto-optically trap the diatomic molecule CaF. In the third experiment of this thesis, buffer-gas cooling is used to study the cooling of the conformational state of large organic molecules. We directly observe conformational relaxation of gas-phase 1,2-propanediol due to cold collisions with helium gas. Lastly, I present preliminary results on a variety of novel applications of buffer-gas cooling, such as mixture analysis, separation of chiral mixtures, the measurement of parity-violation in chiral molecules, and the cooling and spectroscopy of highly unstable reaction intermediates.

Contents

Citations to Previously Published Work

Portions of the research described in this dissertation were published in the following references:

1. Drayna, G.K., Hallas, C., Wang, K., Domingos, S.R., Eibenberger, S., Doyle, J.M., Patterson, D. "Direct Time-domain Observation of Conformational Relaxation in Gas-phase Cold Collisions." arXiv:1601.03359 [physics.chem-ph] (2016), submitted to Angewandte Chemie.

2. Hemmerling, B., Drayna. G.K., Chae, E., Ravi, A., Doyle, J.M. "Buffer gas loaded magneto-optical traps for Yb, Tm, Er and Ho." New Journal of Physics 16.6 (2014): 063070.

Acknowledgments

I'd like to thank all of the members of the Doyle group who have made my time here an incredible experience. First I'm thankful to John Doyle. Under his guidence I have matured in many ways. I'd like to thank the laser cooling experiment with whom I shared many laughs and good company during the long hours spent stooped over the optical table or getting sprayed in the face with toxic laser dye. I'd like to thank the large molecule group for showing me that best moments in science can happen when you are siphoning gasoline out of a motorcycle. I'd like to thank my colleagues and friends from the CUA to JILA, who provided spare optics on a moments notice, good ideas during my talks, and good times outside of lab. I'd like to thank Stan Cotreau, Jim MacArthur, and Steve Sansone. I would have never made it through graduate school without them. I'd like to thank all of my mentors in the labs over the years, from my first day as a researcher mixing ceramics with Jim Zaykoski at Naval Surface Warefare Carderock, all the way to putting the final touches on my thesis with Sandra Eibenberger, and eveyone in between. I'd especially like to thank David Patterson, who showed me how to build a wood floor over a pit on my first day of graduate school, among other things. I'd like to thank Eun Young Choi for being a wonderful partner for many years of graduate school. Lastly, I'd like to thank my parents, who provided the support and inspiration for me throughout my entire education.

To my family and friends

Chapter 1

Introduction

1.1 Physics of Cold Atoms and Molecules

Despite the simplicity of the atom, the study of its properties is a powerful scientific endeavor. The field of atomic physics has produced countless new physical insights in both the precise study of isolated atoms and the study of interacting ensembles of atoms[1]. Cold, dilute gases of atoms offer the ideal system for such studies. The low temperature of these systems is paramount precision measurements, as well as the manifestations of the effects of interactions. In addition, low temperatures improves the ability to confine and manipulate such gases. A temperature and density regime of interest for cold gases is one where the mean thermal energy is lower than most or all of the internal energy state spacings of the atom or molecule. Also of interest is where the thermal energy is lower than the energy scale of interactions and the energy scale of the trap holding the atoms. The realization of the first magneto-optical trap[2], Bose-Einstein condensate[3, 4], and a dilute atomic degenerate Fermi gas[5] have revolutionized the field of atomic physics. Cold atomic gases in such systems serve as the starting point for countless experiments involving precision measurement[6, 7,

8], quantum simulation[9, 10], exotic quantum phases[11, 12], many and few body systems[13], hybrid systems[14], and applications such as atomic clocks[15, 16] and inertial sensors[17].

In the last decade, research on on simple molecular systems has blossomed[18]. Diatomic molecules have two additional degrees of freedom compared to atoms: rotation and vibration of the two nuclei. Electric charge can be separated across the distance between two nuclei bound together in a diatomic molecule due to chemical bonding. A diverse set of diatomic molecules can be electrically polarized in the lab frame with relatively low laboratory electric fields. Cold gases of electrically polarized molecules are predicted to exhibit molecule-molecule interactions $\alpha^{-1} \approx 137$ times stronger than the interactions between magnetic atoms. These strong interactions, combined with the long natural radiative lifetime of the rotational states of the molecule, make diatomic molecules interesting possible candidates for precision measurement[19, 20], quantum simulation[21], and quantum computation[22, 23] experiments. The ability to interact chemically and exchange nuclei during a collisions in a cold gas of molecules also opens the possibility to study chemistry at cold and ultracold temperatures[18]. At the same time, the difficulty of cooling and trapping diatomic molecules compared to atoms is increased as a result of these additional degrees of freedom. While a small class of closed-shell molecules have been produced at ultracold temperatures and high density[24, 25], work is on-going to diversify the number and types of molecules which can be produced at ultracold temperatures. Current efforts are focused on two general classes of methods. The first class is composed of direct cooling methods such as laser cooling[26], magneto-optical trapping[27], and evaporative cooling[28]. Indirect methods are those where the cold molecules are assemble from pre-cooled constituent atoms[29].

While ultracold diatomic molecular experiments have been envisioned as extensions of experiments with atoms (albiet very complicated extensions), it is fruitful to also consider experiments on cold, large polyatomic molecules and their possible uses for new chemistry and spectroscopy experiments. Most of our understanding of chemistry is derived from experiments at room temperature, where molecules may exist in a vast number of rotational and vibrational states, and may even exist in a large number of geometries (e.g. conformational states) at room temperature. As the geometry of the molecule is a major determining factor in its chemical and biological properties, the ability to study molecules in a single state, including geometry, is critical[30]. At temperatures tepid compared to atomic or diatomic systems, large molecules occupy an immensely reduced number of these states and the study of their properties can be much more powerful. Just as the presence of the rotational and vibrational degrees of freedom in diatomic molecules significantly increases the difficulty of cooling, the larger number of degrees of freedom of a large molecule might seem to render gas-phase cooling hopeless. Nevertheless, methods to cool large molecules have been found[31, 32, 33, 34, 35].

1.2 Buffer-gas cooling

Buffer-gas cooling is a technique in which a warm or hot source of atoms or molecules is cooled by elastic collisions with a cold inert buffer gas, typically helium or neon. It is a robust and versatile method for producing large volumes ($V \gg 1$ cm^3)and high density ($n \geq 10^{12}$ cm^{-3}) atomic and diatomic molecular gases cooled in nearly all degrees of freedom to temperatures as low as $T \approx 200$ mK[36] . Buffer-gas cooling has been used to cool a great variety of atoms and diatomic molecules, accounting for half of all atomic species studied at low temperature. Remarkably, buffer-gas cooling

of large organic molecules without cluster formation has also been demonstrated[33]. Buffer-gas cooling has been used to load magnetic traps of atoms and molecules. However, in order to cool molecules or atoms below $T = 200$ mK, alternative methods are required. For example buffer-gas cooling has been used to initially cool and load a magnetic trap of metastable helium, which was then cooled to a BEC using evaporative cooling[37].

Buffer-gas cooling typically takes place in a closed cell. However, the contents of such a cell can be extracted into a beam by the construction of an aperture in the cell. Atomic and molecular beams are often used to transport atoms from a source region (i.e. the cell) to an experimental region free of effects such as collisions. Cold beams can be used for measurements performed directly in the beam, and for measurements made once the particles in the beam have been trapped. Such beams have a rich history in the development of modern AMO physics. The buffer-gas beam is an ideal beam source for many experiments[38]. Cold large molecules, which have an extensive history of study in supersonic expansion jets[31], can also be studied in buffer-gas beams[39]. In addition to generally favorable properties, such as high flux and low internal temperature, the low forward velocity of the buffer-gas beam in the laboratory frame makes it highly compatible with stationary traps. For example, a deep superconducting magnetic trap has been loaded with molecules from a slow buffer-gas beam using optical pumping[40]. In particular, a buffer-gas beam is attractive when methods for the deceleration of the beam are technically challenging.

1.3 Summary of Work Presented in This Thesis

The work in this thesis describes novel applications of buffer-cooling. In one set of experiments, we for the first time interface buffer-gas cooling with the magneto-optical

trap (MOT), a traditional workhorse of atomic physics. In Chapter 2 of this thesis, I will describe how slow buffer-gas beams of rare-earth atoms are used to directly load a magneto-optical trap. Due to the very high flux and slow velocity of the buffer-gas beam used in the experiment, we achieve unprecedentedly high loading rates of the MOT. Additionally, this work paves the way for the production of a molecular MOT. In Chapter 3, I will discuss laser slowing and other progress towards a MOT for calcium fluoride (CaF) molecules. CaF is a candidate molecule for quantum simulation and ultracold chemistry experiments. We successfully demonstrate a proposed trap for CaF using an analogous system in ^{6}Li atoms, as well as laser slowing of a slow buffer-gas beam of CaF molecules to velocities needed to capture them in our proposed trap.

The next section of the thesis focuses on buffer-gas cooling of large molecules. Large molecules offer the largest increase in phase space density upon cooling, which I discuss in Chapter 4. In Chapter 5, I look more deeply into the cooling of large molecules in a cold buffer-gas. In particular, we directly observe conformational (geometric) cooling of the molecule 1,2-propanediol in a buffer-gas cell. In Chapter 6 of this thesis, I discuss a number of future directions using buffer-gas cooling of large molecules that I find exciting. In particular, I will discuss preliminary results towards the separation of chiral molecules using Moire deflectometry, a measurement of parity violation in chiral molecules, and the creation and spectroscopy of highly unstable and reactive molecules.

Chapter 2

Buffer-Gas Loaded MOTs for Exotic Atoms

2.1 Laser Cooling

2.1.1 Concepts and History

The most common technique for the production of ultracold (< 1 mK) gases of atoms is via laser cooling and trapping[41]. Laser cooling utilizes the velocity dependence of the radiation of pressure of a monochromatic optical field on an atom. An atom on resonance with a laser will experience an average force in the direction of $\overrightarrow{\mathbf{k}}$, the wavevector of the incident laser field. If the frequency of the laser, as seen in the frame of the atom, moves off-resonance, radiation pressure ceases to exert a force on the atom. This naturally happens as an atom is decelerated via the Doppler effect. When counter-propagating lasers are applied to a gas of atoms, the result is a narrowing of the velocity distribution of the gas. This narrowing, which occurs without significant increase in the spatial extent of the gas, results in phase-space compression, or cooling

of the gas. The optical force on an atom from the radiative cycling of photons is

$$F = \hbar k \Gamma \tag{2.1.1}$$

, where $\hbar$ is the reduced Planck's constant, $k = 2\pi/\lambda$ is the magnitude of the wavevector with wavelength λ, and Γ is scattering rate of the transition, dependent on the line-width of the atomic transition and the intensity of the applied laser field. For a typical atomic MOT, $\lambda \approx 400 - 800$ nm, $\Gamma \approx 10^7$ s^{-1}, and a species mass of $m \approx 100$ amu $\approx 10^{-25}$ kg, this gives an acceleration of the atom of $a \sim 10^4$ m/s^2.

The final temperature of a laser cooled gas is approximately determined only by the width of the atomic resonance. Photons emitted by the atom have some distribution of frequencies, which can result in a stochastic force on the atom. The momentum distribution resulting from this force is described by the $Doppler - limit$ on the temperature of a laser cooled gas. This temperature is typically on the order of $T \sim 100$ μK, with the mean speed of an atom being $|v| \sim 1$ m/s. For a large class of atoms, a more complex cooling mechanism can be present, which relies on the composite structure of atomic states. Even with this $Sub - doppler\ cooling$, the ultimate limit to the temperature of a laser cooled cloud is set by the stochastic jitter of the emission of a single photon, which is on the order of $T \sim 1$ μK, with the mean speed of an atom being $|v| \sim 1$ cm/s.

Laser cooling was first proposed in 1975 in the context of trapped ions by Wineland and Dehmelt[42], and for free atoms by Hansch and Schawlow[43]. Laser slowing of an atomic beam was first demonstrated in 1982 by Phillips and Metcalf[44]. In 1985, ultracold atoms were first produced in a so-called optical molasses by Dalibard and Phillips[45], and separately by Chu et al.[46]. Shortly thereafter in 1985, ultracold atoms were trapped in a magnetic trap by the Migdall et al.[47]. Then, in 1987,

the Raab et al. demonstrated the first magneto-optical trap (MOT)[2]. This rapid growth of progress in the field of ultracold atoms has driven the development of many of the ideas and technologies described in the introductory chapter of this thesis.

2.1.2 The Magneto-Optical Trap (MOT)

The MOT is a simple modification of the general principle of laser cooling described above. A schematic of a MOT is shown in Figure 2.1.1. Consider an atom with a total angular momentum $J' = 1$ in the excited state and $J = 0$ in the ground state. In the presence of a linear magnetic field gradient dB/dz, the three different projections of the excited angular momentum state $|J' = 1, m_{J'} = \pm 1, 0\rangle$ experience a spatially dependent Zeeman shift in their energies. This spatially dependent Zeeman shift is used to apply a linearly dependent restoring force on the atoms. The cooling lasers are red detuned from the zero-field transition frequency by an amount δ. As a moving atom travels away from the center of the trap, the Zeeman shift brings the atom into resonance with the cooling lasers. In order to provide confinement, the correct beam of the counter-propagating pairs must be resonant with the atom. This is accomplished by using circularly polarized cooling beams with opposite helicity. Due to the different sign of the g-factor and angular momentum selection rule for each projection state, only the laser pointing towards the center of trap will be on-resonance with the atom. This results in a light-force based trapping and simultaneous cooling of the atom gas in the trap. The typical temperature of a MOT is between the Doppler limit and sub-Doppler limit, depending on the exact configuration of the trap and the experimental conditions. The MOT provides additional power over an optical molasses in that the achieveable phase space compression is higher. In particular, a MOT can achieve a phase space compression of $\rho_f/\rho_i \sim 10^{-7}$ compared to a room temperature vapor.

The trap restoring force is $F_r = -kx$, where k is the spring constant of the trap, along with a viscous damping force to make a total force of $F = -\gamma v - kx$. The damping of the trap is given by

$$\gamma = -\frac{8\hbar k^2 s_0 \delta}{\Gamma\left(1 + 2s_0 + (2\delta/\Gamma)^2\right)} \tag{2.1.2}$$

, where s_0 is the saturation parameter for the transition given by the power of the laser beams, k is the wavevector of the laser light, and Γ is the natural line-width of the state. The spring constant is given by

$$k = m\omega^2 = \frac{8\hbar k (dB/dz) s_0 \mu \delta}{\Gamma\left(1 + 2s_0 + (2\delta/\Gamma)^2\right)} \tag{2.1.3}$$

, where μ is the magnetic moment of the excited state of the atom. For a values of $\delta = \Gamma$, $\mu \times (dB/dz) \times 10^{-3}$ m$/h = \delta = \Gamma$, and $k = \frac{2\pi}{6\times 10^{-7}}$, this formula produces $\omega \approx 2\pi \times 10^3$ Hz. The capture velocity of the MOT can be estimated from

$$v_c \approx \sqrt{ar} = \sqrt{\frac{\hbar k \Gamma r}{2m}} \tag{2.1.4}$$

, where r is the radius of the MOT laser beam and m is the mass of the atom. For the typical values above and $r \approx 1$ cm and $m \approx 100$ amu, this yields $v_c \approx 50$ m/s. The MOTs described in this thesis are estimated to have a capture velocity of $v_c \approx 25$ m/s.

2.1.3 Ultracold rare-earth atoms

Laser cooling of rare-earth atoms has led to considerable progress in the fields of metrology, quantum gases, and quantum simulation. Notable examples include Yb[48],

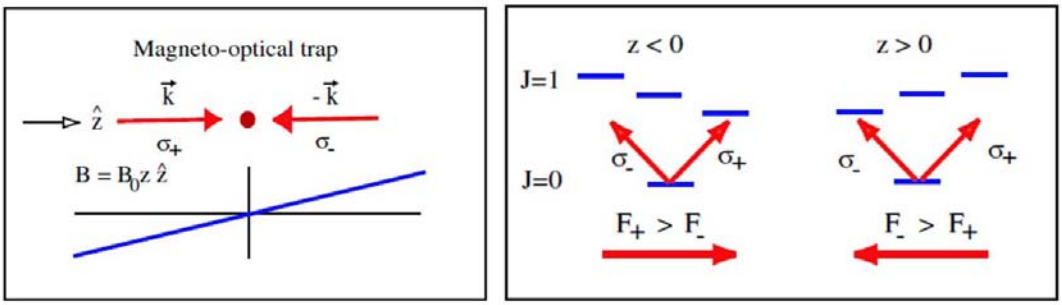

Figure 2.1.1: The magneto-optical trap. Top: A typical configuration of red-detuned laser beams and magnetic field. Bottom: Trapping forces for a $J = 0 \rightarrow J = 1$ atomic transition. Adapted from M. Lukin's Ph 285b course notes.

Cr [49, 50], Tm[51], Er [52, 53] and Dy [54]. The latter four have large magnetic dipole moments, suitable for the study of systems with long-range dipole-dipole interactions [55] and the testing of fundamental theories [54], while Yb has been used in quantum simulation studies [56, 57, 58]. Other possible uses for ultracold non S-state atoms could include the creation of exotic quantum phases and quantum magnetism. In these works, laser cooling does not proceed via closed-cycle transitions. Rare-earth atoms, with the exception of Yb, have a multitude of intermediate electronic states between the electronic ground state and the short-life time excited states used for laser cooling to which the atom can decay during laser cooling. For example, in the case of Er, 110 intermediate states need to be considered [53], many of which have long lifetimes compared to the excited state. However, these states somewhat improbably filter back into the ground state within a relatively short time period. This has led to the laser cooling, trapping, and condensation of several species of rare-earth atoms. In this work, we achieved magneto-optical trapping of Yb, Tm, Er, and Ho.

The relevant level structures for the rare-earth species cooled in this thesis are shown in Figure 2.1.2. The common feature of all of these species is the large line-width blue transition near 400 nm. These transitions have a line-width of $\Gamma \approx 2\pi \times 30$

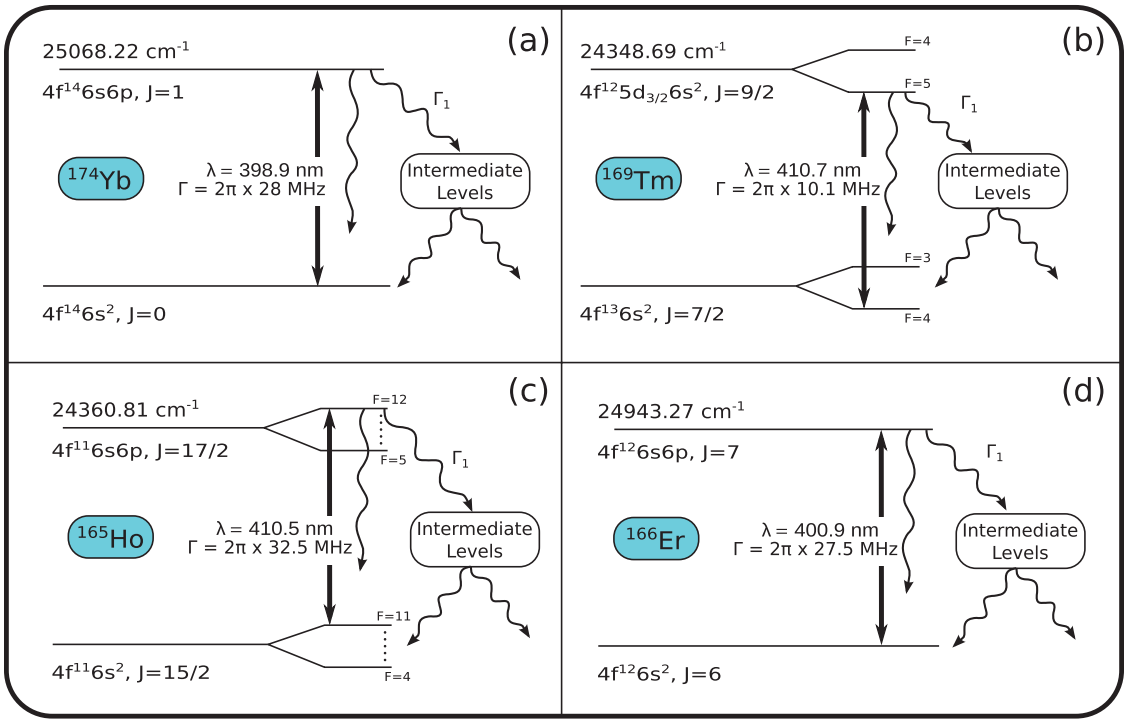

Figure 2.1.2: Partial level scheme of all species with their corresponding laser cooling transition. The schemes correspond to a) Yb, b) Tm, c) Ho, and d) Er. Only the decay to metastable states Γ_1 is considered for modeling the detuning dependent decay as shown in equation 2.4.11. The values are taken from [59, 60, 61].

MHz, which leads to a Doppler temperature $T_D \approx 1$ mK. The laser power required to saturate these transitions is $P \approx 50$ mW/cm^2, and the field gradient required to make a MOT using 1 cm diameter beams is $dB/dz \approx 20 - 40$ Gauss/cm.

2.1.4 Towards Direct Laser Cooling of Molecules Using a MOT Loaded with a Slow Buffer-gas Beam

As discussed in the preceeding chapter, one potentially useful source of some ultracold molecules is laser cooling, including magneto-optical trapping. At the time of this work, recent experiments employing hydrodynamically enhanced cryogenic buffer gas beam sources [38, 62] had reported several advances toward the direct production of

ultracold molecules via laser cooling. Specifically, the optical slowing and laser cooling of SrF [26, 63], the creation of a two-dimensional magneto-optical trap (2D-MOT) for YO [64], and laser slowing of CaF [65] in a supersonic jet had been achieved. However, all of these experiments were performed in freely propogating beams. A MOT loaded from a buffer-gas beam had never before been achieved. Since the time of this work, magneto-optical trapping of SrF[27] and the laser slowing of CaF in a slow buffer-gas beam (Chapter 3 of this thesis) have been achieved.

In this chapter, we discuss the successful use of a two-stage, slow buffer-gas beam for loading MOTs, including species that have leaky optical cycling transitions. At the time of the work, this was a significant step toward loading polar diatomic molecules into a MOT. Employing a two-stage helium buffer-gas beam [62, 66], we created cold, slow atomic beams of lanthanide atoms and loaded them directly into a MOT. The effects of the collisions between residual helium from the buffer-gas beam source and the trapped atoms were characterized.

We also studied for the first time the feasibility of loading a MOT for molecules using this source. The low mean forward velocity of our beam source is $v \approx 60$ m/s, which renders a Zeeman slower unnecessary and thus allows for a direct loading of the MOT. This demonstrated a possible experimental path to a MOT for molecules; this beam is slower than the hydrodynamic buffer-gas beams used in other laser cooling experiments and thus requires a shorter distance to slow the molecules to velocities which can be capture in the MOT. The initial cooling stage of our experiment relies only on collisions with He atoms, and thus is not dependent on the internal structure of the species. The results of this work were confirmed with the first loading of a MOT for SrF molecules, and all subsequent known experiments working towards a MOT for molecules are now using this method.

2.2 Experimental Apparatus

The experimental apparatus for the buffer-gas loaded MOTs of rare-earth atoms is a compact apparatus which, for the first time, mates cryogenic buffer-gas cooling technology with room temperature ultracold atom technology. A full schematic and photograph of the experimental apparatus is shown in Figure 2.2.2.

2.2.1 Vacuum Chamber and Dewar

The vacuum chamber of the apparatus is divided into two general regions - a cryogenic region and a room temperature region. A CAD schematic of the vacuum chamber and dewar are shown in Figure 2.1.1. The primary challenge of designing this apparatus was the effective removal of the residual helium buffer-gas from the MOT region of the chamber. While robust and large magneto-optical traps were achieved, the limiting factor in highly closed-cycling transition atoms was loss due to 300K background helium gas collisions. This apparatus was also used for initial spectroscopy and photon-cycling measurements on CaF, and remains in use by the Doyle laboratory by the SrOH laser cooling experiment, and was designed and constructed from scratch (minus the out vacuum can frame) during my thesis work. I machined and fabricated all parts in the cryogenic region, and partially or fully machined all of the parts in room temperature region.

The entire dewar is elevated above an optics table via optical posts and allows both lateral and vertical optical access to all sections of the apparatus. The outer vacuum can is constructed from 8"x8"x17"x1/2" Al 6061 extruded tube stock. Side plates were custom machined out of 1/2" and 3/4" thick Al 6061 plate stock. The core of the cryogenic section of the apparatus is an IR labs 'mini-dewar', which holds ~ 1 liter of both liquid nitrogen and liquid helium, and achieved a base temperature of

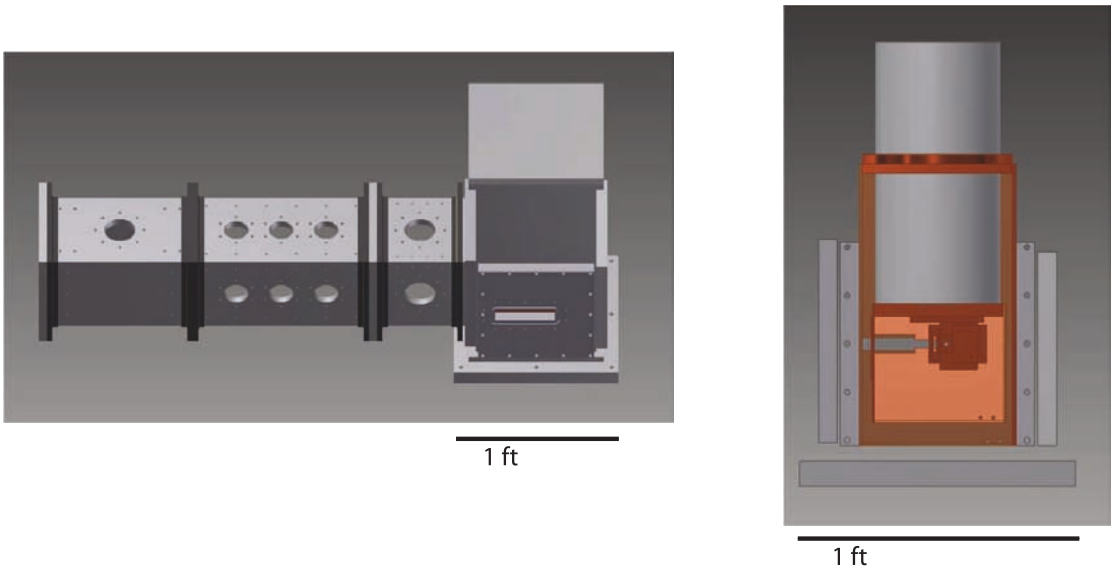

Figure 2.2.1: CAD schematic of the experimental vacuum chamber and dewar. Left: Full external view showing room temperature region on the left side and cryogenic region on the right side. Right: Cross section of cryogenic region showing buffer-gas cell and cryogen pots. Gray material represents Al 6061 alloy and burnt orange colored material represents Cu 101 alloy.

$T = 2$ Kelvin upon application of a high pumping-speed vacuum to the liquid helium pot of the dewar. A Cu 101 cold plate is mounted to the bottom of the IR labs dewar. The Cu 101 '4K' radiation shields are mounted to the side faces of the cold plate. The 77K radiation shields are mounted to a Cu101 round-to-square collar around the liquid nitrogen pot. Cryo-pumping achieved by charcoal sorb, which covers the interior and exterior of the 4K shields. Optical access into the 4K environment is achieved with cryogenic windows attached to both lateral sides of the 77K shields and the bottom of 77K shields and via open holes in the corresponding 4K shields.

A two-stage buffer-gas cell is mounted directly to the bottom of the cold plate. This cell is directly based on the design in Lu et al. [66]. The cell is loaded with buffer-gas in the rear of the cell through a 1/4" Cu 101 fill line, which is heat sunk first to 77K, and then to 2K via brazed Cu101 bobbins. The buffer-gas flows through

a diffuser plate into the center bore of the cell, which is a 1 inch diameter cylinder 1 inch in length. The main cell block has a 1 cm window for an in-cell absorption laser measurement and a small snorkel with a 532-nm AR coated window for optical access for the 2nd-harmonic YAG laser used for ablation of the target. The front aperture on this main cell block was a 3 mm diameter circular aperture. Four Cu101 2.8 mm thick spacers connect the main cell block to a 1/2" long, 1" inner diameter 2nd state cell. Four lateral apertures exist on each side of the cell and are covered in 37% transparency Cu 'coarse' mesh. The final aperture is 1 cm in diameter aperture and covered by the same mesh. The mesh is heat sunk using an compressed ring of indium wire. Just down stream from the aperture of the cell and facing vertically down is a 1/2"x1/2" square dielectric mirror to allow for 2D laser collimation or spectroscopy of the atomic beam.

The beam first exits a 1.5 cm diameter aperture in the 4K shields and then a 1 inch diameter aperture in the 77K shields into the first of three sections of the room temperature region of the vacuum chamber. The room temperature section of the vacuum chamber is constructed from 6"x6"x28"x1/2" Al 6061 extruded square tube. The three sections seal with Viton O-ring seals and are held together with flanges welded on to the chamber body. Each section is separated by an intermediate plate containing an aperture. The first upstream section, called the beam region, contains a KF 50 port which is expanded out conically to a Varian V-301 turbo-molecular pump with a pumping speed of $\sim$ 300 l/s. The first aperture plate contains a 1" diameter aperture and has several mounting screws onto which a Uniblitz VS-14 fast mechanical shutter is mounted. This shutter opens to allow the atomic beam through, and then closes to prevent residual helium gas from entering the next chamber. The next chamber is the MOT chamber, and has 3 KF 40 ports on each side. One port

contains a Varian 80 l/s turbo-molecular pump. The MOT coils are mounted above and below this section. The final aperture plate, with a 2 inch diameter hole, connects to the final region pump region. This region has an ISO 80 hole on top that is conically expanded and connected to a Varian V-550 turbo-molecular pump.

When the cryogenic section of the buffer-gas chamber is at operating temperatures, the typical background pressure in the dewar is $P \approx 1 \times 10^{-7}$ Torr throughout the chamber. With $f = 1$ SCCM Helium flow, the pressure in the beam region is typically $P \approx 1 \times 10^{-6}$ Torr and $P \approx 2 \times 10^{-7}$ Torr in the MOT region. With a single 1 liter liquid He fill, the dewar has a run time of 3 hours. Under house vacuum application to the bath, the run time was approximately 2 hours.

2.2.2 MOT Coils

The MOT coils were wound from hollow core Kapton-insulated copper wire with a square profile of cross-sectional area 6 mm x 6 mm. Each coil has an inner radius of $R = 9.9$ cm, an outer radius of $R = 16.0$ cm and thickness of $T = 4$ cm, with 10 turns, 8 wires across. The center coil is located $z = 11.9$ cm from the geometric center of the MOT chamber. In practice each coil has a few more turns to ensure meeting our design specification of a maximum field gradient of 40 G/cm, bringing the total number to about 11.5 turns. Each coil was powered by a separate 8V, 220 A superconducting magnet power supply model HP 6671A. The upper and lower coils had final resistance of $R = 0.045\ \Omega$ and $R = 0.043\ \Omega$ and were run at a current of $I = 176.0$ Amps and $I = 158.0$ Amps respectively. The lower coil required less current because the optical table surface just below the coil was made of ferromagnetic steel. Active water cooling was achieved with a Neslab System I heat exchanger to building chilled water. The coils provided a radial magnetic field gradient of 38 G/cm at the

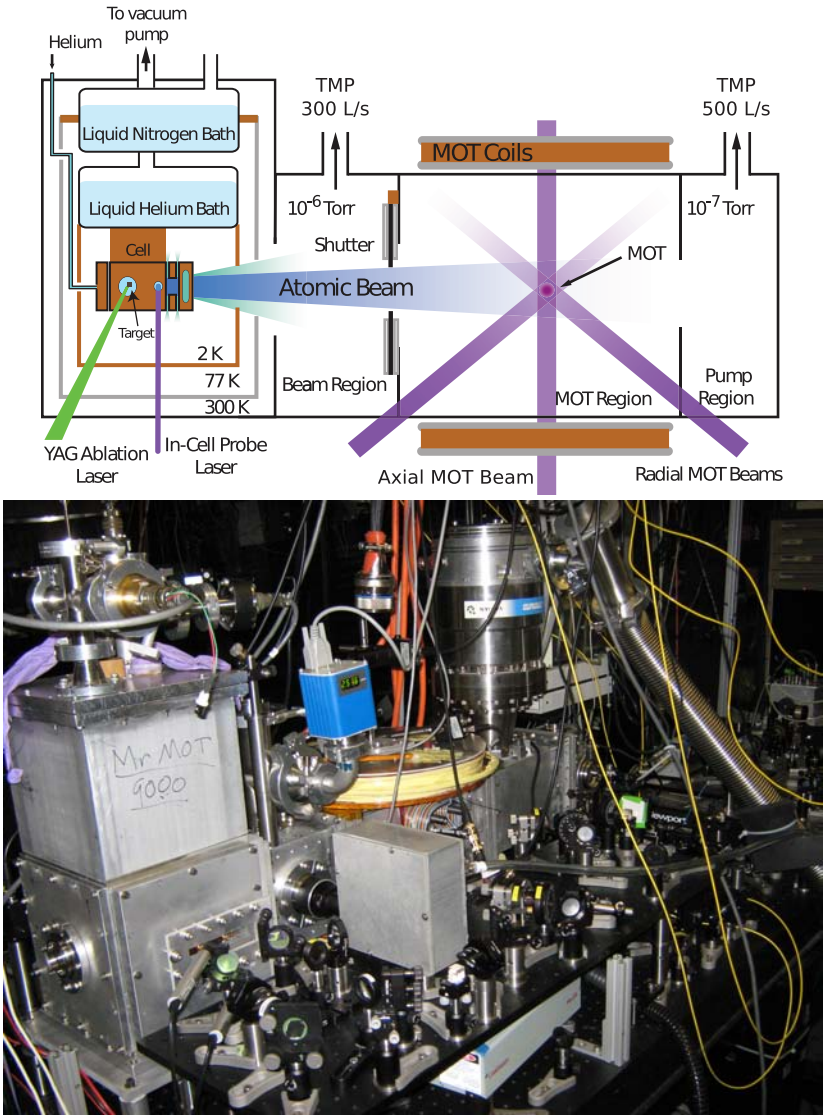

Figure 2.2.2: Schematic and photograph of the apparatus used for the buffer-gas loaded MOTs of atoms. A cryogenic buffer gas beam source (left, labeled 'Mr. MOT 9000') opens into a room-temperature MOT section, separated by a differential pumping region. The photomultiplier tube, which is located transversely to the atomic beam, is visible in the photo as the metal box with lens tube system (photo center, lower). The imaging system, which is also located transversely to the atomic beam, is not visible. The distance between the exit of the cell and the MOT is 42 cm. The MOT coils are visible as the mylar tape-covered wire assembly above the chamber. The lower coil is not visible in the photograph.

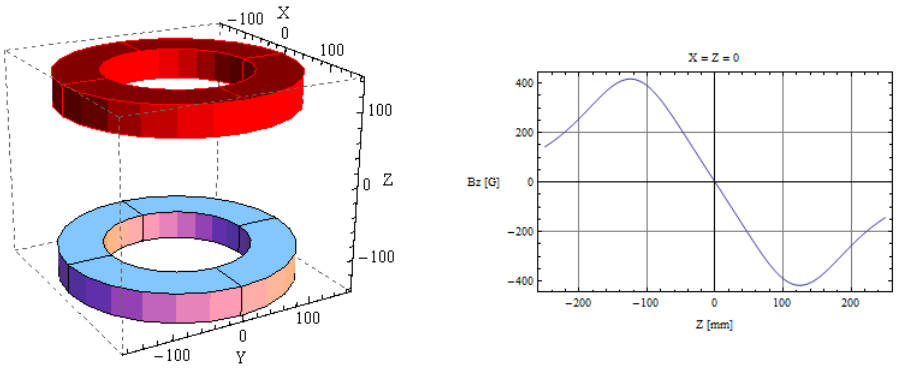

Figure 2.2.3: Finite element simulation of the MOT coils using the Radia software package. On the left is the model of the coils built in Radia, and on the right is a plot of the z-component of the magnetic field along the z-axis (vertical) of the experiment.

aforementioned currents, as determined by finite element simulations which are shown in Figure 2.2.3. This relatively high gradient is necessary to make MOTs using the strong blue transitions of the rare-earth atoms. The maximum field amplitude of the coils was $B_r \approx 400$ Gauss.

2.2.3 Laser System

MOT laser beams for each atomic species are derived from the same frequency-doubled Coherent 899 Ti:Sapphire ring laser. The 899 is pumped by a Verdi V-10 laser, and emits up to 2 W output power at a wavelength of $\lambda = 798$ nm. This light is coupled into a modified bow-tie cavity based on a Spectra-physics Wavetrain dou-

bling unit using an LBO crystal. Approximately 100 mW of frequency-doubled light is produced out of the doubling unit, which is propagated free-space to the apparatus optical table where it is split into individual MOT beams. Each MOT beam has 15 mW power with a $1/e^2$ diameter of 9.8 ± 0.5 mm. The Ti:Saph laser is locked to a HeNe laser via an optical Fabry-Perot transfer cavity, providing MHz laser line-width, which is used to determine the error in the lifetime measurements.

A Toptica DL100 diode laser system with Nichia 399 nm diode (Type NDHV310ACAE1 - lot 4114AA) was used for spectroscopy, as well as seeding a 0 degree Celsius master-slave laser system based on a Nichia 400 nm ($P = 120$ mW output power) diode (Type NDV4313). This master-slave laser system was used in some cases as a slowing laser. Atoms are introduced into the gas phase by laser ablation of solid precursor targets with 4 ns long pulses and mJ energy from a Continuum Minilite 532 nm Nd:YAG laser.

2.2.4 Detection system

We detect atoms in the MOT by imaging fluorescence onto a calibrated photomultiplier tube (Hamamatsu R8900-20U). To reduce background due to scattered laser light, we spatially filter the collected fluorescence using an objective that focuses the MOT image through a variable intermediate aperture with a minimal diameter of ~ 600 μm. Simulation of the imaging system using commercial ray-tracing software (LightTools), determined the collection efficiency to be $(2.5 \pm 0.5) \times 10^{-3}$. A pixeLINK USB CCD camera provides imaged fluorescence detection of the beam and MOTs, which was crucial for the alignment and fine-tuning of the MOT.

2.3 The Slow Buffer-gas Beam

The two-stage buffer-gas cell is a crucial technology for mating cold molecular beams with lab frame stationary traps. In this particular work, it allows direct loading of the MOT without the need for a Zeeman slower, which is a technically difficult and species dependent component of an ultracold atom apparatus. The two-stage buffer gas cell, invented by Dave Patterson and studied in detail by Hsin-I Lu[66], use a second cell of lower density to minimize collisions which boost the forward velocity of the beam upon exiting the cell. Briefly, the cell, operating at 2.5 K, uses a combination of hydrodynamic extraction and a second slowing stage to produce a cold and effusive-like beam with a peak forward velocity of $60 - 70$ m/s and FWHM of ≈ 70 m/s. A plot of the forward velocity distribution of our beam upon arrival in the MOT region of the apparatus is shown in Figure 2.3.1. A considerable fraction of atoms move below the capture velocity of the atomic MOTs, which is estimated to be 25 m/s for all species we trap here. In addition to the lower forward velocity, the two-stage cell is adept at re-directing residual He buffer-gas off of the main axis of the buffer-gas beam. This reduces the residual He load in the room temperature region in comparison to a single-stage buffer-gas cell.

2.4 MOTs of Rare-earth Atoms Loaded via a Buffer-gas Beam

MOTs of Yb, Tm, Er, and Ho atoms are successfully loaded from the slow buffer-gas beam source described above. Of particular interest are two things. First is the compatibility of the MOT with the buffer-gas beam source. The figures of merit for this are the lifetime of the MOT and the total number of trapped atoms in the

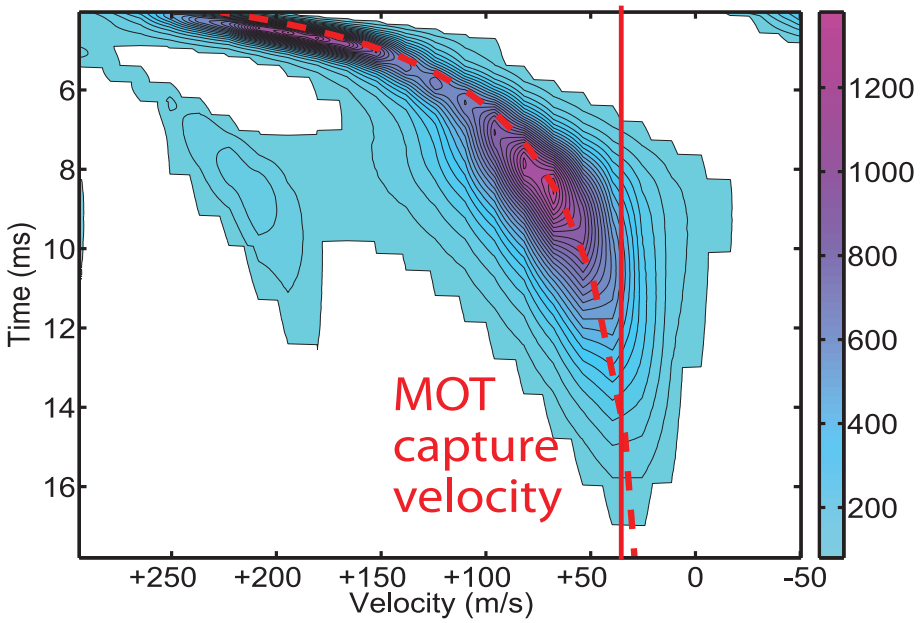

Figure 2.3.1: The forward velocity distribution of the Yb beam from the two-stage cell as a function of arrival time as measured 42 cm downstream in the MOT region of the chamber using Doppler spectroscopy. The second peak visible near +200 m/s is due to another isotope. The color scale is in arbitrary units.

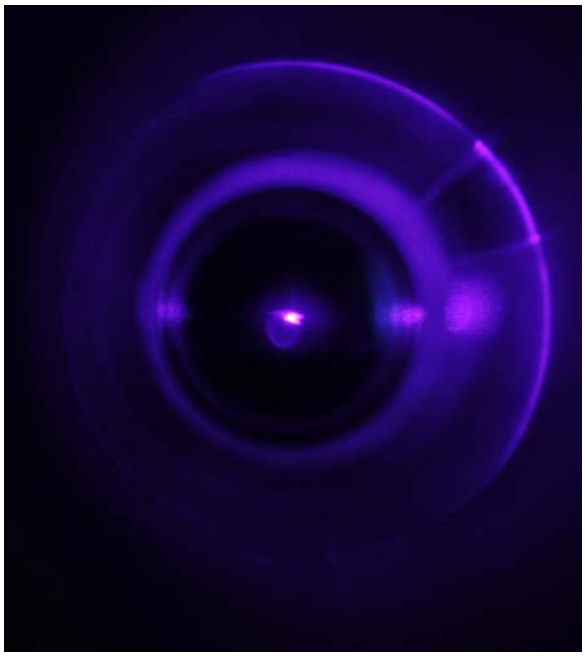

Figure 2.4.1: A snap-shot photo of the YB buffer-gas loaded MOT (center). The outer rings are scattered light off of the vacuum chamber viewports.

MOT. The parameter of interest is the absolute loading rate of the trap, as the high flux and slow velocity of the buffer-gas beam could allow for very high loading rates. This could make the buffer-gas loaded MOT a useful starting point for ultracold atom experiments involving exotic atoms or multi-species traps where high number is required for the ultimate experiment.

2.4.1 Dynamics of MOT Loading From a Pulsed Buffer-gas Beam

The loading process of the MOT can be described by a phenomenological differential equation for the number of trapped particles $N(t)$,

$$\frac{dN}{dt} = R_l(t) - \alpha N(t) - \beta N(t) \tag{2.4.1}$$

where $R(t)$ is the loading rate, α the loss due to background gas collisions and β the intra-particle two-body loss. In our measurements, no evidence for two-body effects is observed and, thus, the corresponding term is henceforth neglected ($\beta = 0$). The loading rate is time-dependent due to the pulsed nature of the loading process. We find that approximating the loading pulse by a Gaussian function as

$$R_l(t) = \frac{n_{tot}}{\sqrt{2\pi}w} e^{-\frac{(t-t_0)^2}{2w^2}} \tag{2.4.2}$$

yields very good agreement with our measured data. The total number of atoms is defined by the normalization $\int_{-\infty}^{\infty} R_l(t)dt = n_{tot}$, where is t_0 the pulse arrival time and w the pulse width. The solution to the loading equation is Equation

$$N(t) = \frac{1}{2} n_{tot} \cdot e^{\frac{1}{2}\alpha(-2(t-t_0)+\alpha w^2)} \cdot \left(\mathrm{erf}\left(\frac{t_0 + \alpha w^2}{\sqrt{2}w} \right) - \mathrm{erf}\left(\frac{-t + t + \alpha w^2}{\sqrt{2}w} \right) \right) \tag{2.4.3}$$

with the error function defined as $\mathrm{erf}(x) = \frac{2}{\sqrt{\pi}} \int_0^x e^{-t^2} dt$.

Examples of the measured time traces of the MOT loading process are shown in Figure 2.4.2 along with a fit to the pulsed loading model. Note that only the tail of the buffer gas beam signal between $t = 20 - 30$ ms is loaded into the MOT. While the beam signal represents only a velocity class corresponding to a certain detuning, the much larger MOT signal stems from particles from a range of velocities which have been actively cooled and trapped.

Fitting to this model allows us to not only determine what part of the beam is loaded into the trap, but to also determine our two parameters of interest, α for the lifetime of the MOT, and $n_{tot}/2w$, which is the loading rate of the MOT.

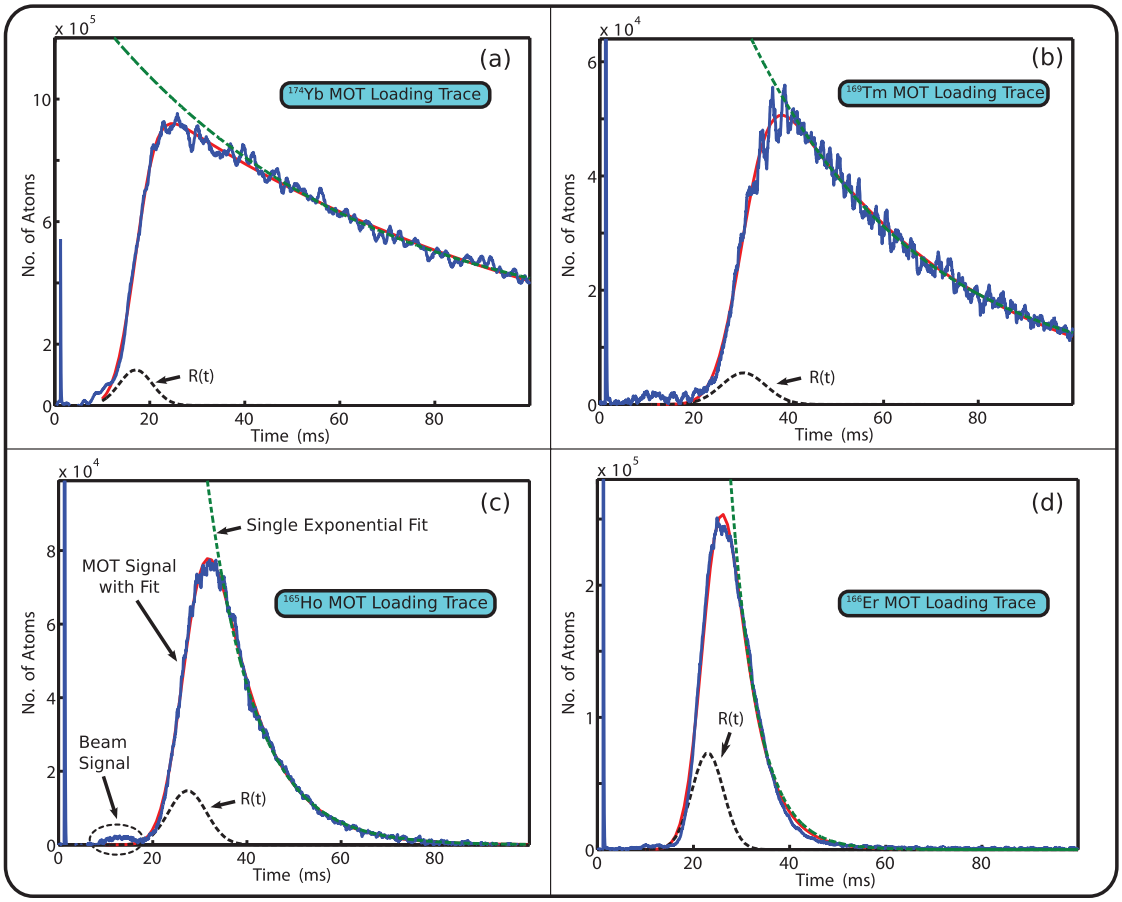

Figure 2.4.2: Example time traces of the MOT loading process for each species with a He flow rate of 0.3 sccm and a repetition rate of the ablation laser of 1.1 Hz. The fit (solid red line) to our pulsed loading model agrees well with the data. The resulting fit parameters can be found in table 1. Also shown is the loading rate R(t) corresponding to the fit and a single exponential fit for comparison.

2.4.2 MOT number determination

Determining the absolute number of atoms in the MOT at any one point in time is a challenging task. Our method to do this is to use the fluorescent signal of the MOT combined with careful calibration of the optical environment of the trap, the collection optics, and the detection system and electronics. Ultimately, the number is based on a reference to an optical power standard, in this case a Coherent laser power meter. See Appendix A.1 for a full analysis of the MOT number determination in our system. Briefly, consider an ensemble of N_{MOT} trapped atoms in a near-resonant light field. Given the detuning (δ) and the intensity of the laser light that the atoms see (I), the excited state fraction (f) can be calculated from the Optical Bloch Equations for a 2-state system.

$$f(s, \delta, \gamma) = \frac{s}{2(1 + s + (2\delta/\gamma)^2)}, \tag{2.4.4}$$

with $s = I/I_0$ being the saturation parameter, and I_0 being the saturation intensity for the transition. The total number of photons per second being emitted from the cloud is given by the product of the number of trapped of trapped atoms N_{MOT}, f, and the natural linewidth (γ),

$$\Gamma = N_{MOT} \cdot f \cdot \gamma \tag{2.4.5}$$

A fraction of these photons strike a detector, a photo-multiplier tube (PMT). This fraction, a combined factor given as β, is determined by the collection efficiency of the detection optics. A fraction (η) of the photons striking the photocathode of the PMT produce an electron that is liberated from the photocathode material into the inner volume of the PMT. η is called the "Quantum Efficiency". Thus, the number of electrons being liberated into the inner volume of the PMT per second is given by

the product

$$\dot{n} = \Gamma \cdot \beta \cdot \eta. \tag{2.4.6}$$

Electrons liberated into the inner volume of the PMT are accelerated through an electric field, striking dynodes and giving rise to a pulse of electrons at the PMT anode. The ratio of the number of electrons arriving at the anode to the original number liberated from the photocathode is called the gain (G). The gain is determined independently by a calibration to an optical power standard in a procedure described below. These electrons leave the PMT anode into a transmission line over the course of a few nanoseconds. From there, the current pulse enters a low-noise current pre-amplifier, which converts the current pulse to a voltage pulse with an amplification of K (V/electron/sec). Additionally, the pre-amplifier serves as a low pass filter for the current pulse. This voltage pulse is measured and logged by a DAQ card in our computer. Thus, the relationship between $\dot{n}$ and the measured output voltage measured by the DAQ is

$$V_{out} = \dot{n} \cdot G \cdot K = N_{MOT} \cdot f \cdot \gamma \cdot \beta \cdot \eta \cdot G \cdot K \tag{2.4.7}$$

We can invert this to write the MOT number as

$$N_{MOT} = \frac{V_{out}}{f \cdot \gamma \cdot \beta \cdot \eta \cdot G \cdot K} \tag{2.4.8}$$

We find from our measurements that typically $V_{out} \approx 1$ Volt, $f \approx 10^{-1}$, $\beta \approx 10^{-3}$, and $G \approx 10^2 - 10^5$. Additionally γ is determined from literature values and is typically $\gamma \approx 10^8$/second, η is determined from the specification sheet of the photocathode material is $\eta = 10^{-1}$, and K is determined from the specifications sheet of the device to be $K = e \cdot 10^6$ V/electron/second $\approx 10^{-13}$ V/electron/second. This results in

$N_{MOT} \approx 10^5 - 10^8$.

2.4.3 High loading rates

The total atom number in the trapand the loading rate are important figures of merit for ultracold atom experiments. Many experiments require a minimum number of ultracold atoms or a minimum phase-space density for technical reasons. After magneto-optical trapping, it is common to have additional cooling and trap loading stages, each with their own loss of atoms. For example, one may load atoms into a far off-resonance trap (FORT), perform evaporative cooling, and then followed by loading into an optical lattice. Starting with the highest possible number in trap reduces the difficulty of achieving these experiments.

The total number of atoms loaded into each trap is summarized in Table 2.1. Note that the variation among the different species is not only caused by the cooling efficiency, but also by the ablation yields, which vary strongly between the species. The number of trapped atoms can be increased by applying low repetition rates of the ablation laser, leading to smaller heat loads on the buffer gas cell and more atoms below the capture velocity, and by using a single-frequency slowing laser. This allows us to achieve a peak number of Yb atoms in the trap of $n = (1.3 \pm 0.7) \times 10^8$ atoms.

In addition to the absolute number, the loading rate of the MOT can be a technically important parameter. Some technical applications requiring high loading rates include atom trap trace analysis (ATTA) studies[67] and high bandwidth atom interferometry sensing applications [68]. In particular, in working with a MOT system with high background pressure, high loading rates enable high MOT numbers despite the background gas loss. This is because the MOT is loaded much faster than the loss time scale. In this work, we achieve the highest ever loading rates yet reported

Species	N_{MOT} (#/Volt)	δN_{MOT} (#/Volt)	N_{Peak} (#)	R_{avg} (#/sec)
^{174}Yb	$2.3 \cdot 10^7$	$1.2 \cdot 10^7$	$(9.0 \pm 4.7) \cdot 10^6$	$(8.0 \pm 4.2) \cdot 10^8$
^{174}Yb w/slowing	$2.3 \cdot 10^7$	$1.2 \cdot 10^7$	$(1.3 \pm 0.7) \cdot 10^8$	$(2.0 \pm 1.0) \cdot 10^{10}$
^{169}Tm	$6.4 \cdot 10^4$	$3.5 \cdot 10^4$	$(5.0 \pm 2.7) \cdot 10^4$	$(6.5 \pm 3.6) \cdot 10^6$
^{165}Ho	$6.6 \cdot 10^4$	$2.7 \cdot 10^4$	$(7.7 \pm 3.1) \cdot 10^4$	$(1.8 \pm 2.5) \cdot 10^6$
^{166}Er	$8.0 \cdot 10^4$	$5.2 \cdot 10^4$	$(2.5 \pm 1.6) \cdot 10^5$	$(9.3 \pm 6.0) \cdot 10^7$

Table 2.1: Summary of MOT numbers and loading rates for each species.

for rare-earth atoms. A few experiments have higher loading rates for species in different groups of atoms, in particular meta-stable noble gas atom MOTs [69] and the occasional alkali vapor cell - atomic funnel experiment[70], but ours is the highest for this family of atoms.

Using the fit of the time dependent MOT fluorescent signal and our calibration of the absolute MOT number, the loading rate, which is defined as

$$R = n_{tot}/2w \tag{2.4.9}$$

, can be determined. Using a single frequency slowing laser, we achieve a loading rate of Yb of $R = (2.0 \pm 1.0) \times 10^{10}$ atoms/sec, along with high loading rates for the other species even without the slowing laser. If we used re-pump lasers or the yellow transition for some of these species, I hypothesize that similar loading rates for the other rare-earth species could be achieved.

2.4.4 Loss due to collisions with background helium gas

Our system has a background helium gas load inherent to the buffer-gas beam source. The helium gas in the chamber can be divided into one of two categories: cryogenic or room temperature. During operation of the buffer-gas beam, helium atoms leave

the cell with roughly a 2K thermal distribution of speeds. This 'beam' of helium is constantly present in the experiment and is incident on the MOT during its loading. The other population of helium atoms has a 300K thermal distribution, and consists of atoms which have scattered off of the outer vacuum chamber of our experiment.

Before undertaking this study, it was unclear how either population of background helium collisions would affect the MOT. It was not known if loading a MOT with a 2 Kelvin helium beam shining onto the MOT would even permit initial trapping. A quick kinematics calculation shows that a head-on collision with a 2 Kelvin helium atom should only change the velocity of a previously stationary Yb atom by $\Delta v = 4$ m/s, which is well below the capture velocity of the trap. Loss due to collisions with room-temperature background helium and out-gassing molecules are known to be a problem that would need a managed solution. A head on collisions between a 300 Kelvin He atom and a stationary Yb atom results in $\Delta v = 50$ m/s, well above the capture velocity of our MOT. Heavier species such as O_2 yields $\Delta v > 100$ m/s for a head-on collision, which would also certainly cause trap loss.

One can estimate the trap loss rate due to room temperature background gas collisions using a simple collision model. The loss rate is

$$\Gamma_0 = n_{He}\sigma_{He-Atom}\bar{v_{He}} \tag{2.4.10}$$

, where $n_{He} = \frac{P}{k_B T}$, $\sigma_{He-Atom} \approx 10^{-14}$ cm^2, and $v_{He} \bar{\approx} 1120$ m/s at $T = 300$ K. This yields $\Gamma_0 \sim 10$ s^{-1} for pressures of $P \sim 10^{-7} - 10^{-6}$ Torr. We characterized the buffer-gas loaded MOTs as a function of the buffer-gas flow rate into our chamber with the shutter always-open, which is shown in Figure 2.4.3. All measurements were taken at the laser detuning which results in the maximum MOT fluorescent signal. The lifetime of the MOT is affected by helium buffer-gas, as seen in the decreasing

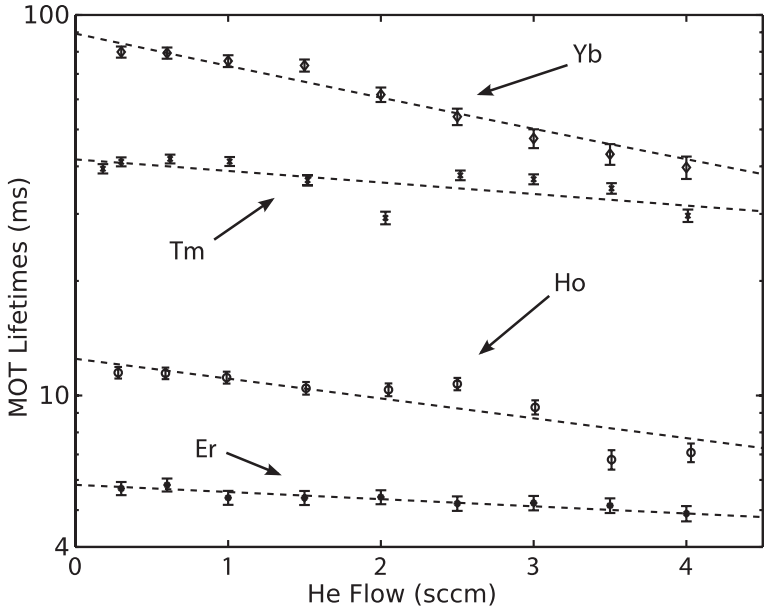

Figure 2.4.3: MOT lifetimes (α) for every species from fitting the time traces to our loading model. The dashed lines are exponential fits and act as a guide to the eye only.

slope of each species, with the highest lifetime at $f = 0.3$ SCCM. However, each species has a very different low-flow lifetime. This is because Tm, Ho, and Er all have loss to meta-stable stables in the intermediate electronic manifold. Yb has a single meta-stable loss channel with $\Gamma_0 \approx 3\ \mathrm{s}^{-1}$. Using the shutter, we are able to achieve lifetimes which are limited by this loss mechanism. For the species experiencing loss to meta-stable states, we are able to characterize this loss as follows.

2.4.5 Loss to meta-stable states

In a simplified model where the presence of the intermediate electronic states is modeled as a loss rate Γ_1 from the system, this loss is the dominant loss rate for the system for Tm, Ho, and Er. As this loss only occurs if the atom is excited to the electronic excited state, the rate will depend on the excited state fraction. Thus, our

	^{174}Yb	^{169}Tm	^{165}Ho	^{166}Er
$\Gamma_0(\mathrm{s}^{-1})$	10 ± 2	20 ± 2	38 ± 7	113 ± 16
$\Gamma_1(\mathrm{s}^{-1})$	-	-	1510 ± 203	2071 ± 753
$1/\alpha$ (ms)	80 ± 4	41 ± 2	-	5.7 ± 0.4

Table 2.2: Summary of measured loss rates for the species trapped in this work. The entries denoted '-' refer to statistically compatible with a null measurement.

model is

$$\alpha(\Delta) = \Gamma_0 + \Gamma_1 \left(\frac{s_{0,eff}/2}{1 + s_{0,eff} + 4\Delta^2/\Gamma^2} \right) \tag{2.4.11}$$

, where $\kappa \cdot s_0$is the effective saturation parameter, Δ is the laser detuning, and $\Gamma = 2\pi \times \Delta v$, where Δv is the natural line-width of the excited state. The effective saturation parameter takes averaging over Zeeman substates and random light polarization in the MOT region into account, where $\kappa \approx 3 \cdot \frac{2F+1}{2F'+1}$ and F corresponds to the hyperfine quantum number of the ground state. This simplified model omits any population which gets recycled back into the ground state after the decay to the metastable state reservoir, but allows for the determination of a lower limit of the decay rate into the intermediate states.

The measurements for each species are shown in Figure 2.4.4. In the case of Ho, for example, we observe the largest MOT fluorescence signal with a red-detuned laser at $\Delta = -1.3\Gamma$. Although this is the optimal detuning for creating high numbers of trapped atoms, the longest MOT lifetime is observed at detunings further to the red. This effect is explained by the lower population in the excited state and, consequently, a lower probability of decaying into a metastable dark state. Increasing the excited state population by moving the laser frequency closer to the transition line center decreases the MOT lifetime almost by a factor of three. The strength of this effect is governed by the decay rate Γ_1. The measurement results obtained for each atomic species are summarized in Table 2.2. For the fitting, Γ_0 and Γ_1 were free parameters.

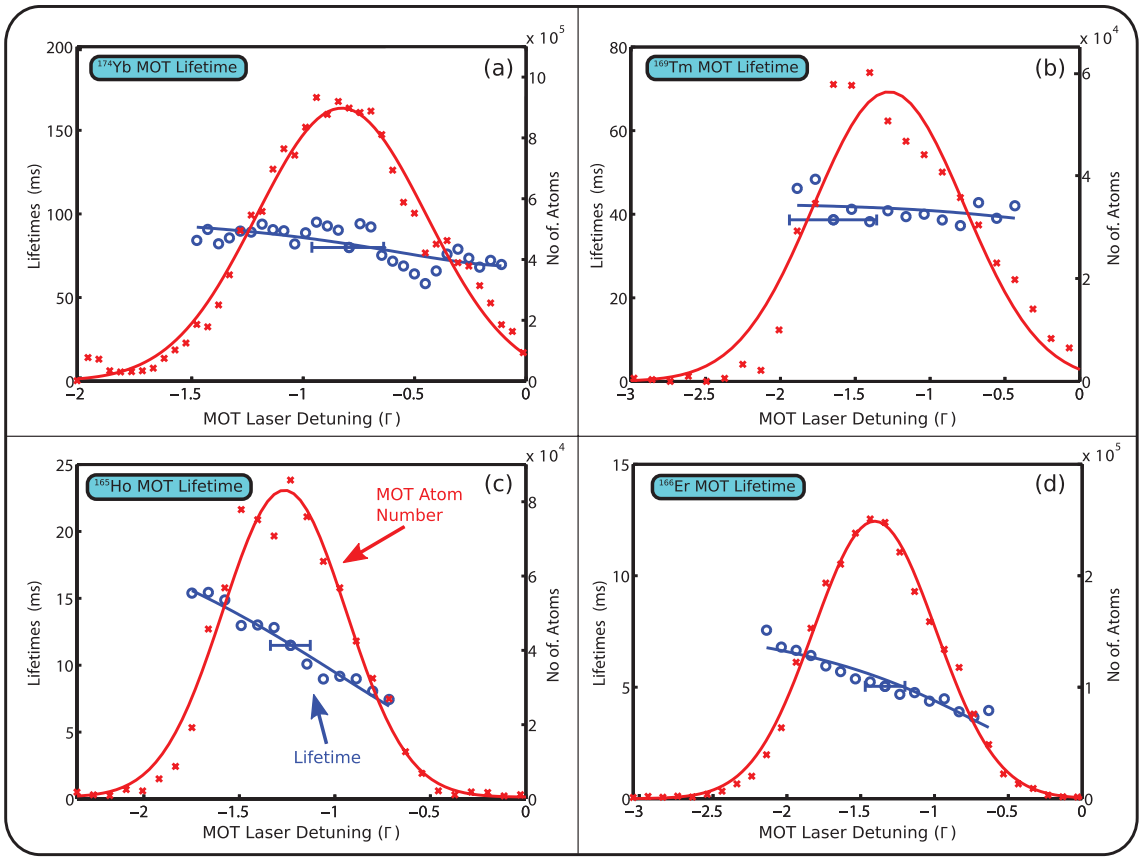

Figure 2.4.4: MOT lifetimes α of all species as function of the laser detuning in units of the natural line-width with a He flow rate of 0.3 sccm and a repetition rate of the ablation laser of 1.1 Hz. Negative values are red-detuned with respect to the line center. The solid line is a fit to eq. 2.4.3. Also shown is the relative atom number in the MOT, including a Gaussian fit as a guide to the eye.

Our measurements indicate an increase of the decay rates with an increase of the He flow rate for all species. In Table 2.2, we list values of the decay rates which are extrapolated to zero He flow. The results for for Yb, Tm and Er are in agreement within the errors described in previously reported work. For Ho, both our measurement and the result of the Saffman group [71] are currently the only experimental estimates of the decay rate to metastable states. At present, no theoretical prediction is available.

Chapter 3

Progress Towards a MOT for CaF

3.1 Molecular Structure

Diatomic molecules have two additional degrees of freedom in comparison to atoms. As there are two nuclei instead of one, the new degrees of freedom arise due to the presence of an internuclear axis with rotational symmetry about only this axis. The result is two distinct degrees of freedom in diatomic molecules - rotations/vibrations around/along the internuclear axis. In comparison, atoms have three degrees of rotational symmetry. The molecular internuclear axis is a *de facto* quantization axis, and this axis may be rotating in space. This leads to the distinct of lab-frame and molecule frame quantum numbers. Molecule-frame quantum numbers must be either parallel or perpendicular to this internuclear axis. The coupling of the electron's orbital and intrinsic angular momentum to this axis determine the structure of the molecule and are in general divided into groups called Hund's cases. The properties of diatomic molecules as they relate to laser cooling and to our molecular species, CaF, are discussed here.

The degree of freedom corresponding to oscillations in the inter-nuclear distance is

called the vibrational degree of freedom. In a diatomic molecule, there typically exist several low lying molecular orbitals with bonding character. For alkali/alkali-earth - halogen diatomic radicals, all states below the highest occupied molecular orbital (HOMO) typically result in a strongly bonding character. Even with the promotion of the unpaired electron to the next several highest states, the orbital remains bonding. The result is that a locally harmonic potential exists near the internuclear distance which minimizes the energy of the orbital. The eigenstates of this potential are quantum harmonic oscillator eigenstates with energies given by

$$E_v = \omega_e(v + 1/2) - \omega_e x_e(v + 1/2)^2 + \omega_e y_e(v + 1/2)^3 + ... \tag{3.1.1}$$

, where v is the vibrational quantum number, ω_e is the vibrational constant, and x_e and y_e are anharmonic corrections which account for actual global structure of the potential energy curves. Under the Born-Oppenheimer approximation, this vibrational degree of freedom is uncoupled from the electronic degree of freedom. Thus, transitions between electronic states with different vibrational wavefunctions have a moment that is proportional to the between the two vibrational wavefunctions $\mu_{ab} \propto \langle\psi_{v_a}|\psi_{v_b}\rangle$. The probability of the transition is then proportional to $|\langle\psi_{v_a}|\psi_{v_b}\rangle|^2$, which is called the Frank-Condon factor.

The rotations of a molecule approximately obey the rigid rotor Hamiltonian. The wavefunctions are given by the solutions to the following Schrödinger equation

$$\frac{\hbar^2}{2\mu R^2}\mathbf{R}^2\psi(\theta,\phi) = E\psi(\theta,\phi), \tag{3.1.2}$$

where $\mathbf{R}$ is the total rotational angular momentum operator, μ is the reduced mass of the atomic nuclei and R is the equilibrium separation of the atomic nuclei. The

wavefunctions which solve this equation are the spherical harmonics $Y_{RM}(\theta, \phi)$with energies

$$E_R = \frac{\hbar^2}{2I} R(R+1) = BR(R+1), \tag{3.1.3}$$

where the prefactor B is called the rotational constant. The eigenfunctions$Y_{RM}(\theta, \phi)$ have well defined parity (reflection about the origin) which alternates as R increases. This rotor is not perfect as it lengthens due to centrifugal distortion. To account for this, we can write the energy as

$$E_R = B_e R(R+1) - D_e R^2 (R+1)^2 + ... \tag{3.1.4}$$

In reality, the rotational constant also depends on the vibrational state of the molecule, such that the rotations have effective constants

$$\begin{aligned} B_v &= B_e - \alpha_c (v + 1/2) + ... \\ D_v &= D_e + \beta_e (v + 1/2) + ... \end{aligned} \tag{3.1.5}$$

And likewise, the vibrational state of the molecule also depends on the rotational state through centrifugal distortion.

A convenient hybrid description of the ro-vibrational energies of the diatomic molecule is accomplished using the Dunham expansion

$$E = \sum_{kl} Y_{kl} \left(v + \frac{1}{2} \right)^k \left(R\left(R+1\right) \right)^l \tag{3.1.6}$$

where $Y_{10} \approx \omega_e,\ Y_{20} \approx -\omega_e x_e,\ Y_{02} \approx -D_e,\ Y_{11} \approx -\alpha_c,\ Y_{12} \approx -\beta_c$ and so forth.

The rotational degree of freedom of the nuclei can then couple to the various other angular momentum present in the molecule, both orbital and intrinsic. In addition

to the rotation angular momentum of the nuclei **R**, these momenta include: **L**, the electron orbital angular momentum, **S**, the electron spin angular momentum, and **I**, the nuclear spin angular momentum. The following 'direct' interactions determine the couplings of these angular momenta, generally through a magnetic coupling:

1. $\mathbf{L} \cdot \mathbf{S}$−the spin-orbit interaction.
2. $\mathbf{L} \cdot \mathbf{R}$−the rotation-orbit interaction.
3. $\mathbf{L} \cdot \mathbf{I}$−the orbital hyperfine interaction.
4. $\mathbf{S} \cdot \mathbf{I}$−the spin-spin hyperfine interaction
5. $\mathbf{S} \cdot \mathbf{R}$−the spin-rotation interaction
6. $\mathbf{I} \cdot \mathbf{R}$−the nuclear-spin rotation interaction

The good quantum numbers under these interactions depend on their relative strengths. The relative strengths lead to different cases called Hund's cases. Most states in most molecules fall into one of five general Hund's cases. An in depth explanation of the Hund's cases are described in [72] as well as excellent discussions in the thesis of Nick Hutzler and Eunmi Chae. The two primary Hund's cases of relevance to our species, CaF, are (a) and (b). Most of the laser cooling schemes for various molecules fall into either of these states, and many of the low lying molecular states of a very broad class of diatomic free radicals are also in either case (a) or (b).

In Hund's case (a), the spin-orbit interaction is stronger than the pure rotation interaction. In this case, both the orbital angular momentum **L** and the spin **S** are strongly coupled to the internuclear axis. The result is that the good quantum numbers are $\Lambda$and Σ, which are the values of their projection along the internuclear axis, along with $\Omega = \Lambda + \Sigma$. Ω then couples with the rotational angular momentum of

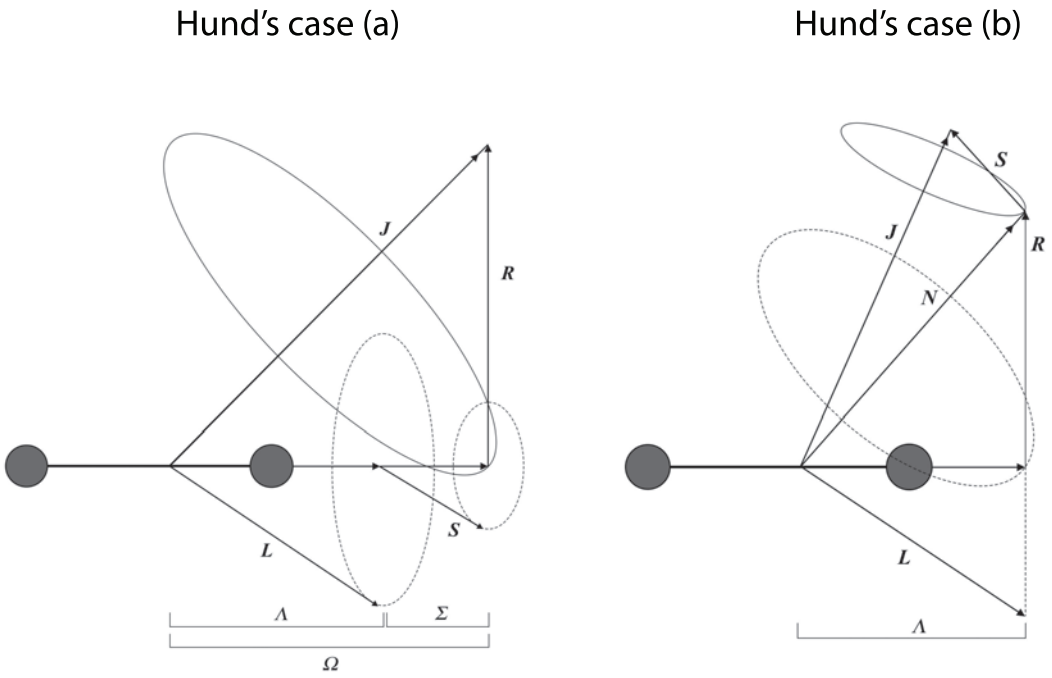

Figure 3.1.1: Vector coupling diagram for Hund's cases (a) and (b)

the nucleus $\mathbf{R}$ to form $\mathbf{J} = \mathbf{R}+\Omega$. Lastly $\mathbf{J}$ couples to $\mathbf{I}$ to form $\mathbf{F} = \mathbf{J} + \mathbf{I}$. A diagram of this coupling is shown in Figure 3.1.1. In Hund's case (b), the rotational spacing is larger than the spin-orbit interaction. While $\mathbf{L}$ is still pinned to the internuclear axis to form Λ, the spin $\mathbf{S}$ is free. The result is that Λ first couples to $\mathbf{R}$ to form $\mathbf{N} = \mathbf{R}+\Lambda$. Next, $\mathbf{N}$ couples to the spin to form $\mathbf{J} = \mathbf{N} + \mathbf{S}$. Lastly, $\mathbf{F} = \mathbf{J} + \mathbf{I}$ is formed by coupling to the nuclear spin. A diagram of this coupling is also shown in Figure 3.1.1. Molecular state are then denoted via the term symbols ${}^{2S+1}\Lambda^{p}_{\Omega}$ in case (a) and ${}^{2S+1}\Lambda^{p}$ in case (b), where p is parity of molecular wavefunction under reflection across a plane containing the internuclear axis and is either $p = \pm 1$. Conventionally, the value of $\Lambda$is reported using a capital Greek letter $(\Sigma, \Pi, \Delta, ...)$ for $(L = 0, L = 1, L = 2, ...)$. In both cases, the vibrational quantum number, which is not associated with any rotational symmetry in a diatomic molecule, is always a good quantum number.

Transitions between molecular states of different rotational quantum numbers proceed according to single-photon selection rules. In case (b), these rules are that $\Delta N = \pm 1$, $\Delta J = \pm 1, 0$, $\Delta M_J = \pm 1, 0$, and lastly that the parity of the state must change. A derivation of these selection rules is found in section 6.11.4 of [72]. For the vibrational transitions, there are no selection rules as the vibrational degree of freedom has no associated symmetry. The only factor influencing the probability various vibrational transitions is the Frank-Condon factor $|\langle\psi_{v_a}|\psi_{v_b}\rangle|^2$. As a result, even for the best choice of states, constant irradiation of a diatomic molecule with a single frequency optical field will result decay to a dark state in time

$$\tau = \frac{1}{\Gamma\left(1 - |\langle\psi_{v_a}|\psi_{v_b}\rangle|^2\right)} \tag{3.1.7}$$

, where Γ is the effective scattering discussed in Chapter 2. An comprehensive reference for this section is found in [72]

3.2 CaF and Laser Cooling Scheme

The primary difference between laser cooling molecules and laser cooling atoms is the ability to cycle a large enough number of photons to remove sufficient quantities of momentum and entropy. The total possible amount of momentum transfer, on average, is

$$\Delta v = \frac{\hbar k}{m\,(1 - |\langle \psi_{v_a} | \psi_{v_b} \rangle|^2)} \tag{3.2.1}$$

. In order to perform laser cooling for molecules as we have for atoms, we need a way to defeat the Frank-Condon factor on the bottom. The first way to accomplish is by carefully choosing a species. Free radicals where the lone electron occupies and orbital with predominantly ionic character exhibit large Frank-Condon factors for on-diagonal transitions ($v" = v'$) due to the weak coupling of the orbital to the nuclear motion of the molecule. M.D. Di Rosa was the first to point out that for surprisingly large set of molecules, the Frank-Condon factors on the diagonal are large enough to permit last cooling with a technical feasible number of laser sources [73]. Our species, CaF, is well studied diatomic free radical with this property. It has a number of additional ideal properties for laser cooling and trapping as well as quantum simulation[21] and cold collisions/chemistry[74, 75] experiments which could be performed following cooling and trapping.

3.2.1 CaF properties

The following are general properties of CaF which are critical to laser cooling, trapping, and dipolar physics:

- Electric dipole moment of the ground state X ($^2\Sigma^+$): 3.07 Debye [76]
- X state magnetic dipole moment: $\mu \approx 1\ \mu_B$[77]

v''	$v' = 0$	$v' = 1$	$v' = 2$
0	$0.987^{+0.013*}_{-0.019}$	0.036	2×10^{-4}
1	< 0.03	0.90	0.07
2	1.3×10^{-3}	0.065	0.83
3	4×10^{-5}	$3.7\times^{-3}$	0.092
4	10^{-6}	2×10^{-4}	0.073

Table 3.1: Franck-Condon Factors for the $X^2\Sigma^+\left(v"\right) - A^2\Pi_{1/2}\left(v'\right)$ transition. If an experimental number is available it is used and denoted with an asterik[78], otherwise the number is calculated via quantum chemistry calculation ([80]) .

- Lifetime of excited state $\mathrm{A}\left(^2\Pi_{1/2}\right)$ $1/\gamma = 19.2$ ns [78].
- X-A transition ($\lambda = 606$ nm) recoil per photon: 1.1 cm/s.

In summary, CaF is a highly polar, magnetically trappable molecule with a strong transition optical electronic transition and high recoil per photon. The $X^2\Sigma^+ - A^2\Pi_{1/2}$ is ideally suited for laser cooling and the analogous transition in SrF has been used for laser slowing and trapping[26, 27]. A $B^2\Sigma^+$ state also exists which could support laser cooling[79]. Critically, the Franck-Condon factors of this molecule are quite favorable and are listed for the lowest few states in Table 3.1. As is visible in the table, this set of factors is called diagonal because the off-diagonal elements are much small than the on-diagonal elements. We can use a simple scheme driving from ($v" = 0 \rightarrow v' = 0$) and with two re-pumping lasers to close vibrational leaks to the level of 25,000 photon scatters.

The rotational and vibrational structure of CaF has been very well studied by various precision spectroscopy methods and its spectroscopic parameters are listed in Tables 3.2 and 3.3., which are drawn from [81] and [82] respectively. The vibrational spacing is on the order of $\Delta E \sim 10^{13}$Hz and the rotational spacing is on the order of $\Delta E \sim 10^{10}$ Hz. The ground state is best described in a Hund's case (b) basis and the excited A state is best described in a Hund's case (a) basis due to a large spin orbit

Dunham Coefficient	Value (cm^{-1})
Y_{10}	588.67608(29)
Y_{20}	−2.91259(12)
$10^3 \cdot Y_{30}$	8.514(2)
$10^6 \cdot Y_{40}$	−6.1(1.1)
Y_{01}	0.3437181(12)
$10^3 \cdot Y_{11}$	−2.444671(93)
$10^6 \cdot Y_{21}$	4.917(20)
$10^7 \cdot Y_{02}$	−4.6954(20)

Table 3.2: The Dunham coefficients for the $X^2\Sigma^+$state in CaF[81]

Parameter	Value (cm^{-1})
T_e	16526.750(3)
A_e	29.15
ω_e	594.513(50
$\omega_e x_e$	3.031(2)
B_e	0.348781(5)
$10^7 \cdot D_e$	4.8078(3)
r_c []	1.9374(1)

Table 3.3: The vibrational and rotational parameters for the $A^2\Pi_{1/2}$ state in CaF, as well as the transition energy[82].

interaction which turns on.

There is additional structure in the ground X state from the spin-rotation interaction (no. 5 Section 3.1), which takes the form

$$H_{\text{spin-rotation}} = \gamma_{v,N}\mathbf{S}\cdot\mathbf{N} \tag{3.2.2}$$

which is on the scale of $\gamma \sim 10^7$Hz. The fluorine atom in CaF contains an $\mathbf{I} = 1/2$ nucleus and therefore the ground state also exhibits a hyperfine structure, which has both isotropic and non-isotropic contributions is. This structure is given by the Hamiltonian

$$H_{\text{hyperfine}} = b_{vN}\mathbf{S}\cdot\mathbf{I} + c_{vN}S_zI_z + C_{vN}\mathbf{N}\cdot\mathbf{I} \tag{3.2.3}$$

Parameter	Value (MHz)
b_{00}	109.1839(5)
b_{10}	$-1.41521(3)$
c_{00}	40.119(1)
c_{10}	1.0562(15)
C_{00}	$2.876(37) \times 10^{-2}$
γ_{00}	39.65891(2)
γ_{10}	$-3.21668(25) \times 10^{-1}$

Table 3.4: The dominant spin-rotation and hyperfine parameters for CaF in the ground X state, drawn from [83]

. This interaction is also on the order of $b, c, C \sim 10^7$ Hz. The spin-rotation and hyperfine parameters have been studied to high precision and their values are listed in Table 3.4.

The resulting ground state substructure within a given rotation-vibration level is four hyperfine states with quantum numbers $F = 0, 1, 2$ roughly spaced by $20 - 70$ MHz, as shown in Figure 3.2.1. The A state has negligible and hyperfine structure, but has Λ-type splitting on the order of $\Delta E \approx 1$ GHz and a very substantial spin-orbit splitting of $\Delta E \approx 30$ GHz , which is discussed in various references, and is described by the Hund's case (a) basis set. Each Λ-doublet has an alternating parity so only one of these states can be addressed from a given rotational level in the X-state.

3.2.2 Laser slowing scheme

Given this knowledge of the structure and Franck-Condon factors, a optimal laser cooling scheme can be designed. Our laser cooling scheme is shown in Figure 3.2.2. We use a main cycling transition on the $X^2\Sigma^+(v" = 0, N = 1, -) \rightarrow A^2\Pi_{1/2}(v' = 0, J = 1/2, +)$ transition at $\lambda = 606$ nm, with a Franck-Condon factor of nearly 99%. We use two vibration re-pumping lasers. The first vibrational re-pump is on the transition $X^2\Sigma^+(v" = 1, N = 1, -) \rightarrow A^2\Pi_{1/2}(v' = 0, J = 1/2, +)$ at $\lambda = 628$

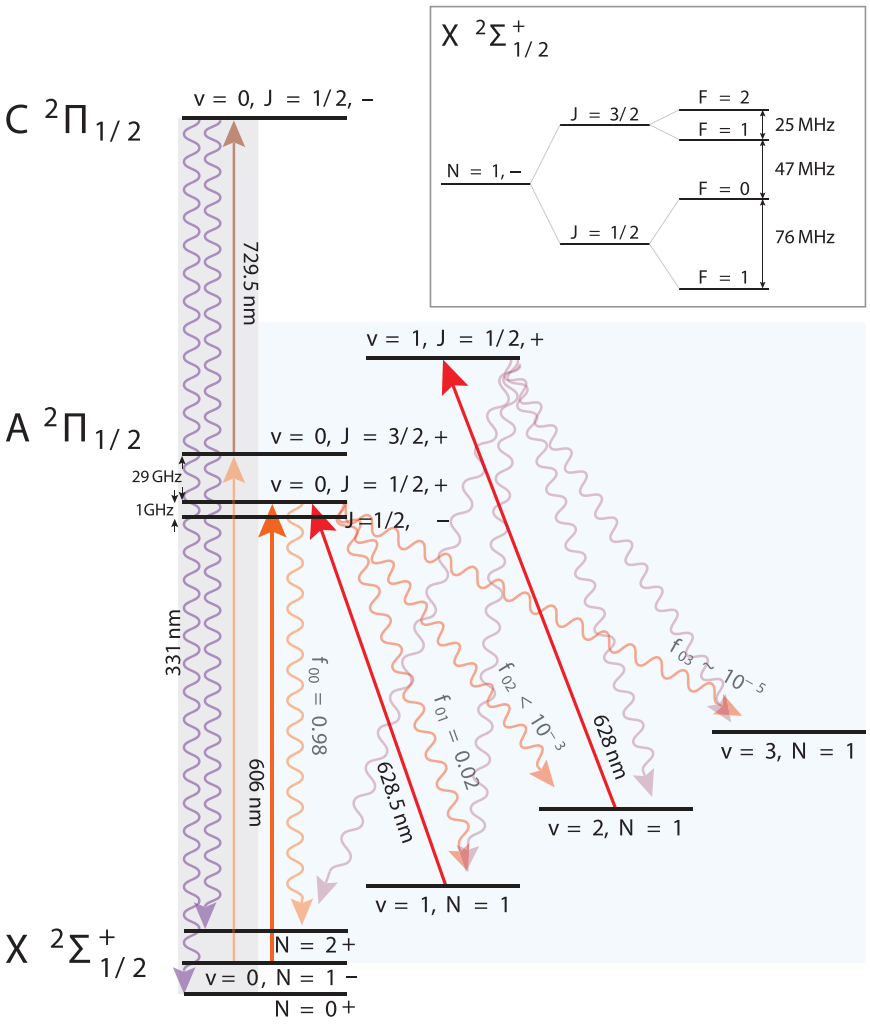

Figure 3.2.1: The CaF structure and laser cooling scheme. The detection scheme is also shown in the shaded gray region. The spin-orbit and hyperfine structure is shown in the inset in the upper right of the figure. The main line is denoted by the orange arrow and the two vibrational re-pump lasers are denoted the red arrows. Decay paths, both those re-pumped and those leading to loss, are denoted by the partially transparent curved arrows and have their respective Franck-Condon factors also denoted. This scheme should allow cycling of $\sim 10^5$ photons on average per molecule before decaying to a dark state.

nm with a Franck-Condon factor of $\sim 90\%$. The second vibrational re-pump laser is off-diagonal on the $X^2\Sigma^+(v" = 2, N = 1, -) \rightarrow A^2\Pi_{1/2}(v' = 1, J = 1/2, +)$ at $\lambda = 628.5$ nm. For a given laser, the spin-rotation and hyperfine structure in the ground state is individually addressed using an AOM set-up. This scheme should allow for scattering of at least 25,000 photons before decay to a vibrational dark state. This number is likely even larger as the experimentally measured main line Franck-Condon factor was found the be significantly better than the theoretical calculation. A number of potential limits to the estimate have been investigated, including two-photon transitions and magnetic dipole transitions, and have all been determined to be smaller than the loss to the third vibrational state. In the magneto-optical trap, as discussed below, additional loss channels will be present.

The laser power required for the scheme is significantly higher than what intuition from 2-level atomic systems would predict. For a two level system the saturation intensity is given by

$$I_s = \pi hc \frac{1}{\lambda^3 \tau} \tag{3.2.4}$$

, which for the main laser cooling line is about $I_s = 14$ mW/cm^2. However, the molecular laser cooling scheme involves a significantly reduced excited state fraction due to the many ground state levels. In addition to increasing the saturation intensity, this decreases the effective scattering rate. Estimates of this factor are $\approx 1/10$, and multi-level rate equation analysis of the CaF laser cooling transition place the effective saturation intensity at $I_s \approx 50$ mW/cm^2[78].

As there are states in the ground state manifold whose total angular momentum quantum number exceeds that of the states in the excited state manifold, certain stretched states states will be dark during laser slowing. In the case of linearly polarized laser cooling light, the stretched states $|F = 2, m_F = \pm 2\rangle$ will be dark. There are

multiple ways in which these states could be remixed back into the cooling cycle[84]. Our method follows that of deMille [63]. We apply a magnetic field transverse to the direction of propagation of the laser. So long as the angle between the magnetic field and the polarization vectors is neither 0 degrees nor 90 degrees, the magnetic field will admix the different projection states with a remixing time set by the Zeeman shifted energy difference.

The last part of the scheme is the detection of the slowed or trapped molecules. This is accomplished by a two-photon transition through the $A^2\Pi_{1/2}(v' = 0, J = 3/2, +)$ state to the higher lying $C^2\Pi_{1/2}(J = 1/2, -)$ state using the main a laser to drive a laser with a wavelength of $\lambda = 729.5$ nm[85, 63]. The photons emitted from the C state have a wavelength of $\lambda = 331$ nm. These UV photons are can then be detected background free and with very low dark counts on a PMT.

3.2.3 MOT for CaF

The presence of dark projection states as discussed above makes a traditional MOT scheme infeasible. After a few photon cycles at the edge of the trap, the molecule would fall dark and drift out of the trap. These types of MOTs do exist in atomic systems and are called type II MOTs. A natural re-mixing mechanism for type II MOTs does exist, but is poorly understood and weak. Nevertheless, type II MOTs and optical molasses of several alkali species[86, 87], and recently for SrF molecules, has been achieved. In alkali atoms, these MOTs have ~ 2 orders of magnitude fewer atoms and a restoring force ~ 1 order of magnitude lower [88]. Our solution to this is the alternating current MOT (AC-MOT) [89]. In this scheme, the magnetic field and polarization of the MOT lasers are simultaneously reversed on the time scale of a single photon scatter. This turns any dark state directly into a bright state after

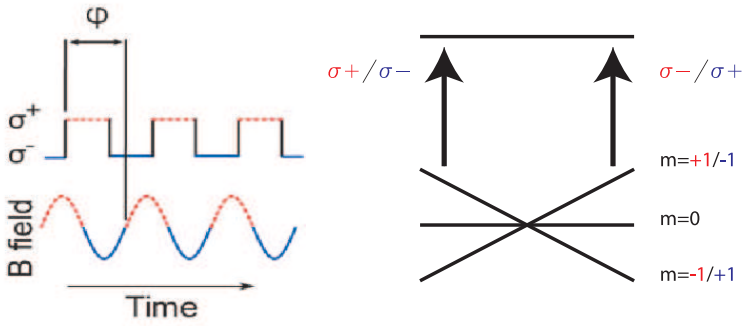

Figure 3.2.2: The AC-MOT. The polarization and magnetic field are simultaneously switched to remix population which decays into an off-resonant projection state at the side of the trap. This figured is partly adapted from [64].

every photon scatter. A schematic of this MOT is down in Figure 3.2.2.

3.2.4 ^{6}Li simulation

The alkali atom Lithium, in particular the isotope ^{6}Li, has an optical transition which has an angular momentum structure similar to CaF. The structure of ^{6}Li is shown in the Figure 3.2.3. The $^2S_{1/2}$ and $^2P_{1/2}$ states both have total angular momenta either of $F = 3/2$ or $F = 1/2$. As scattering from the MOT beams requires a change of $\Delta m_F = \pm 1$, the fully stretched $m_F = \pm 3/2$ in the ground state will be dark. Thus, a MOT on the line connecting these states at $\lambda = 671$ nm, called the D1 line, is a type II MOT. In particular, we ran our MOT on the line connected only to the $J' = 1/2$ level in the excited state. In order to test our white light slowing and our AC-MOT, we made and studied AC-MOTs on this line.

3.3 Apparatus

The apparatus used for this experiment is a 2nd generation apparatus designed to improve upon the original apparatus used for the buffer-gas loaded MOTs described

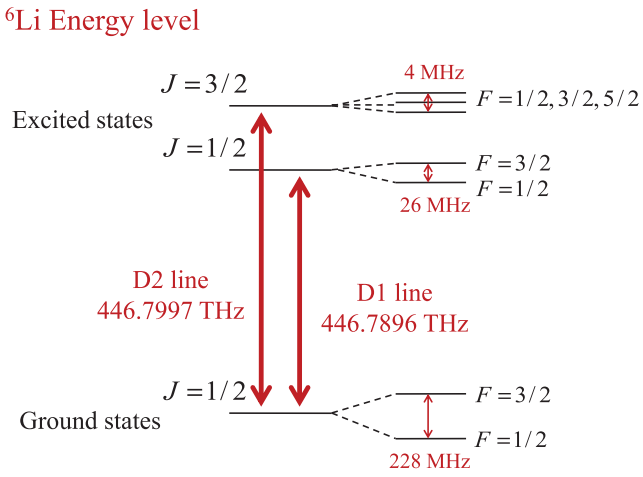

Figure 3.2.3: Energy levels of ^{6}Li with D1 and D2 lines denoted. Figure courtesy of Eunmi Chae.

in Chapter 2 of this thesis.

3.3.1 Dewar and Vacuum Chamber

The vacuum chamber again has two distinct sections - a cryogenic dewar and a room-temperature sections. In this generation, the cryogenic region was based off the standard Doyle group cryogen-free beam box design with closed cycle pulsed tube cryocooler and 1K Pot. After an intermediate stem region which was ultimately discarded, the room temperature section is a UHV section, which I had the pleasure of designing after having spent nearly 2 years with the previous generation experiment. Eunmi was in charge of the cryogenic section, which was much more involved than in the 1st generation. Her dewar was beautifully designed and performs flawlessly!

The cryogenic section of this apparatus is described at length in Eunmi's thesis, and previous generations were used for the optical loading of CaF and CaH, the eEDM experiment, and even the early generations of the large molecule experiment

described in the latter half of this thesis[66, 40, 19, 90]. Briefly, a rectangular Al 6061 vacuum chamber with dimensions approximately 21"x21"x25"x0.5" is supported from below by an extruded Al 80-20 support structure. The chamber features removable side panels with transverse optical access. All seals are made from Viton o-ring seals. The top plate of the chamber is a 1" thick Al plate with all vacuum and cryogenic feed-through. The front plate of the dewar has a bulkhead mount KF port which serves as the junction to the room-temperature section of the apparatus. A Cryomech PT415 closed cycle pulsed tube refrigerator is mounted on the top plate, with 50K and 4K stages extending into the vacuum chamber. 77K radiation shields made from Al 6061 and 4K radiation shields are made from Cu101 and are separately heat-sunk the 50K and 4K stages of pulsed tube respectively. A 1K Pot, also mounted to the top plate, is connected to a long Cu101 bar. A 2-stage buffer-gas cell similar to the one described in Chapter 2 of thesis is mounted to this 1K bar. Cryo-pumping is accomplished by multiple sheets of activated coconut charcoal sorb, which are arranged in a 'protected' configuration. ^{4}He is again used as the buffer-gas, and the cell has a temperature of 1.5K-2K and a hold time of 4-6 hours during normal operating conditions. The typical pressure in the cryogenic beam box during operation is $P \sim 10^{-9}$ Torr. Molecules are introduced into the buffer-gas via ablation of a solid, hot-pressed CaF_2 target using a Continuum Minilite 2nd Harmonic YAG laser.

The junction to the room temperature section is accomplished by a gate valve and a flexible bellows with KF sealing on the cryogenic side and CF-sealing on the UHV side. In the first experiments described in thesis, an additional intermediate region with its own Agilent V-551 turbo-pump called the stem was also in place, although this has since been removed. From this gate-valve on is the UHV section. The UHV section was designed on three key figures of merit:

1. Good Vacuum.

2. Optical access.

3. Modularity and availability.

This was accomplished with an all CF system based around a Kimball physics 6" spherical Octagon (MCF600-SphOct-F2C8), which is off the shelf for $3100 and made of electro-polished stainless steel. Pumping is accomplished through a 6" CF Tee out the bottom of the octagon using an Agilent V-551 Turbo-pump which was matched in pumping speed to the molecular conductance of all apertures. Viewports were BBAR coated for 400-700nm, with two viewports being adaptable with Kimball physics groove-grabber chamber mounting pieces. The top of the octagon can either house a full sized 6" CF viewport or a zero-length adapter to a long CF-2 3/4" snorkel for minimizing scattered light. A tee on the farthest downstream end allows a vacuum gauge, RGA, and Ti-sublimation pump to be connected to the chamber. Pressures of $P \sim 10^{-9}$ Torr and $P \sim 10^{-8}$ Torr are achieved in this region with and without buffer-gas flow respectively. Imaging optics outside of the vacuum chamber can be placed as close as 3" from the center for the chamber. The distance from the cell to the center of the MOT chamber is 50 cm. A diagram of the entire apparatus is shown in Figure 3.3.1.

3.3.2 Laser and Optical System

I was extremely fortunate to have the opportunity to do a significant development of the optical systems involved with this experiment. The end result was the fabrication from scratch of 3 full laser systems (6 total lasers), a design and (assistance of) construction of a custom high-index electro-optic device, the set-up of the infamous

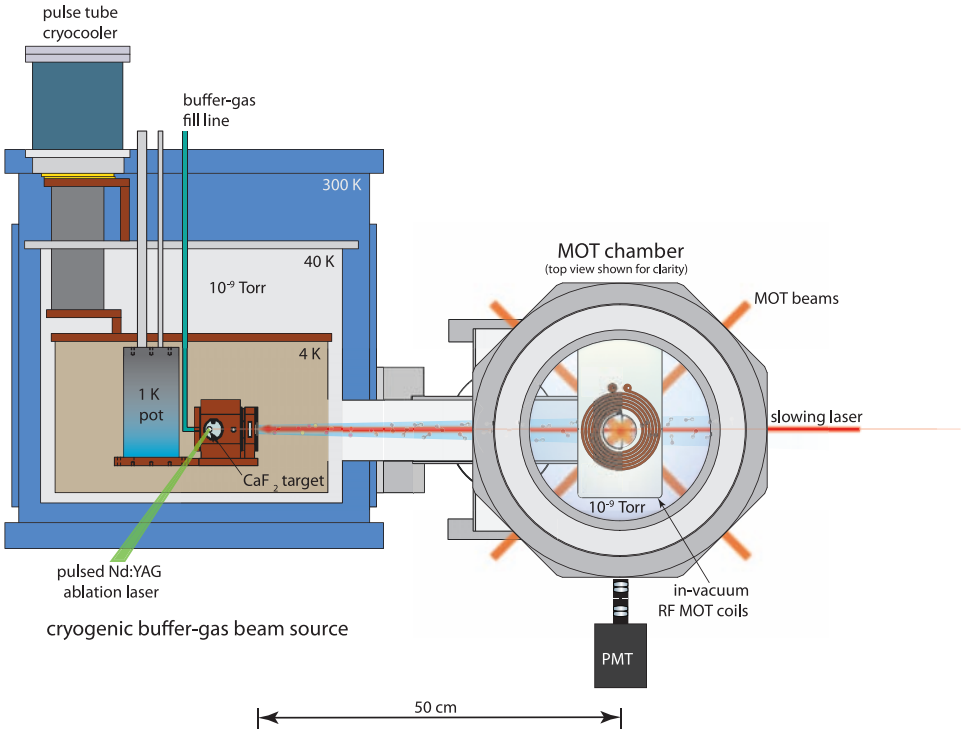

Figure 3.3.1: A schematic of the experimental apparatus dewar and vacuum chamber. The cryogenic section is in the blue beam box on the left and the right side is the room temperature UHV section, which is depicted here artificially enlarged and with a rotated top view for clarity.

Function	Main line	1st re-pump	2nd re-pump	2 photon
Slowing	899 Dye laser	899 Dye laser	Cold ECDL system	Ti-Saph
MOT	Aculight OPO+SFG	899 Dye laser	Cold ECDL system	-
^{6}Li Slowing	Li tapered amplifier	-	-	-
^{6}Li MOT	Ti-Saph	-	-	-

Table 3.5: The laser system to accomplish the laser slowing and cooling of CaF and of ^{6}Li.

Coherent 899 ring dye laser and the set-up of the sleek Aculight OPO+SFG system. The following table summarizes the lasers involved in the slowing and trapping experiments on ^{6}Li and CaF.

3.3.2.1 Coherent 899 Dye and Ti:Sapphire Laser

The Coherent 899 dye laser is a beautiful optical system when running stably. It provides high power, narrow linewidth, large mode-hop free tuning range, and an excellent Gaussian mode over wavelengths ranging from the blue to the IR. As a molecular laser cooling experiment, the ability to reach any wavelength and with high power is crucial, and the dye laser is the only system with such capability. This laser typically produces 500-1000 mW of orange or red light with either Rhodamine 6G or Rhodamine 640 laser dye when pumped with a Verdi V-10 laser at 532 nm. While this laser can achieve all of those wonderful properties described above, its reliance on a liquid jet of dye as a critical optic in the cavity renders it's long term reliability and alignment relatively poor. Slight changes in the shape or pointing of the liquid dye jet, even on the scale of a single wavelength of light, can take the laser from working well to hopelessly misaligned overnight. Additionally, the dye tends to only last a few hundred to a few thousand pump Watt-hours and is toxic. This makes maintenance often and difficult. I set up the laser Bert, which is luckily relatively well behaved. Bert was first manufactured in 1991 and has aged well over

the years, making him relatively reliable and stable. Thanks to Radiant Dyes, which still supports the 899, we were able to keep all our 4 dye lasers functional (although rarely all at the same time!)

The 899 can also be run with a Ti:Sapphire crystal as the active gain medium. This crystal achieves gain in the range from 700 nm-1100 nm and has similar output power and spectral properties as the dye configuration of the laser. Unlike the dye laser, however, this laser lacks the reliability and maintenance problems of the liquid dye laser. We used this laser to produce the MOT beams for the ^{6}Li MOT and we currently use the laser to drive the $A \rightarrow C$ transition in CaF.

3.3.2.2 Li Tapered Amplifier system

In order to produced the laser light for white light slowing and magneto-optical trapping of ^{6}Li using the D1 transition at $f_{\mathrm{D1}} = 446.78900$ THz ($\lambda = 671$ nm), I built a laser system based on a tapered amplifier. A tapered amplifier (TA) is an electrically pumped semiconductor gain medium capable of amplifying as little as $P = 10$ mW of input optical power to as much as $P = 5$ W output power, depending on the frequency range. The tapered amplifier consists of a single channel of gain medium with a width which scales linearly with distance traveled through the channel by the seed light. This tapering allows the local optical intensity to not exceed the damage threshold for the material during amplification. The tapered amplifier can be easily seeded with a narrow linewidth external cavity diode laser and, in practice, a tapered amplifier system is a relatively inexpensive and reliable way to produce several hundred mW of laser light suitable for laser cooling and trapping applications. The Fermi Gas Microscope of Markus Greiner's group uses Li as the atomic species and derives their laser cooling light from such a system. Florian Huber and Max Parsons

from that experiment were extremely helpful in my construction of the Li TA system, and even provided a finished TA mount for my construction. The resulting system I constructed had an output power of $P \approx 300$ mW with a laser linewidth of a few MHz. Ultimately, the Li TA system suffered from slow degradation due to insufficient initial seed power and the relatively poor output mode rendered the utility of the system limited to white light slowing applications. Simple improvements would allow a higher output power of $P \approx 500$ mW and long term reliability of the system.

The seed was based on an Optnext HL6756MG diode ($P_{\max} = 15$ mW output) and was constructed by converting a pre-existing diode laser system. At room temperature, single mode operation at 671 nm was achieved with tuning from the grating, although a substantial mode-hop free tuning range is only achieved with the diode at relatively lower output power of $P \approx 5$ mW. The tapered amplifier itself is a 500 mW output unit at 670 nm (EYP-TPA-0670-00500-2003-CMT02-0000). The tapered amp is mounted a large copper mounting piece, designed by the Greiner group and fabricated at the SEAS shop. The TA mount is designed to mount on a 30 mm cage mount system with the TA center facet in the center of the cage mount system. The TA mount is cooled by TECs (TE tech TE-71-1.4-1.5 TEC 8.9V/6.1A max) needed to maintain the TA at the correct operating temperature (18.5 C). These TECS output a lot of waste heat., which is dissipated by an extruded Al6061 heat sink (http://www.newark.com/h-s-marston/890sp-02500-a-100/heat-sink-extrusion/dp/15J9647). In order to get the collimation lenses very close to TA chip for maximum NA (power) and easier, more stable alignment, a pair of custom collimation adapters from 1" lens tube to M9 is used. These adapters have an outer diameter of 0.990" to allow for a small amount of room in case the TA is slightly off center. Mounted aspheric lenses sit inside the adapter with the rear of

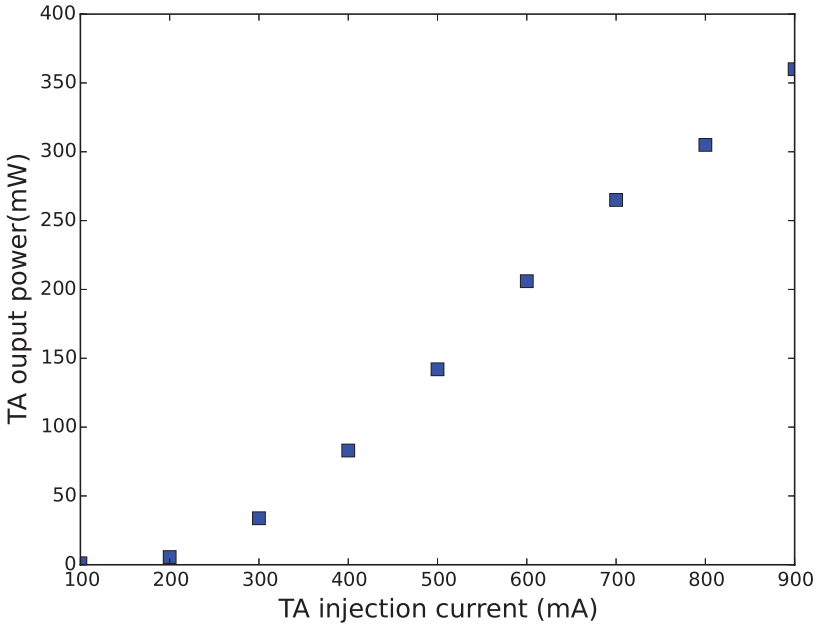

Figure 3.3.2: The output of the TA chip as a function of injection current. This data was taken with a seed laser power of 12 mW.

the lens facing the TA. These adapters fit inside a cage mounted z-translation stage threaded for a 1" lens tube.

The procedure for mounting the TA is tricky and delicate. Please refer to the laser cooling lablog if you mount a TA in a similar set-up. The alignment of the TA is also tricky and unique, although not dissimilar from coupling a laser into a single mode fiber, except the TA can be damaged if not enough seed light is coupled into the chip. Again, refer to the laser cooling lablog for the procedure I used when aligning the TA.

The final output of the TA system with an input power of $P = 12$ mW is plotted versus injection current below in Figure 3.3.2.

The output mode of the TA is highly astigmatic. Proper collimation and mode shaping is essential to producing a usable laser beam. Using a number of cylindrical

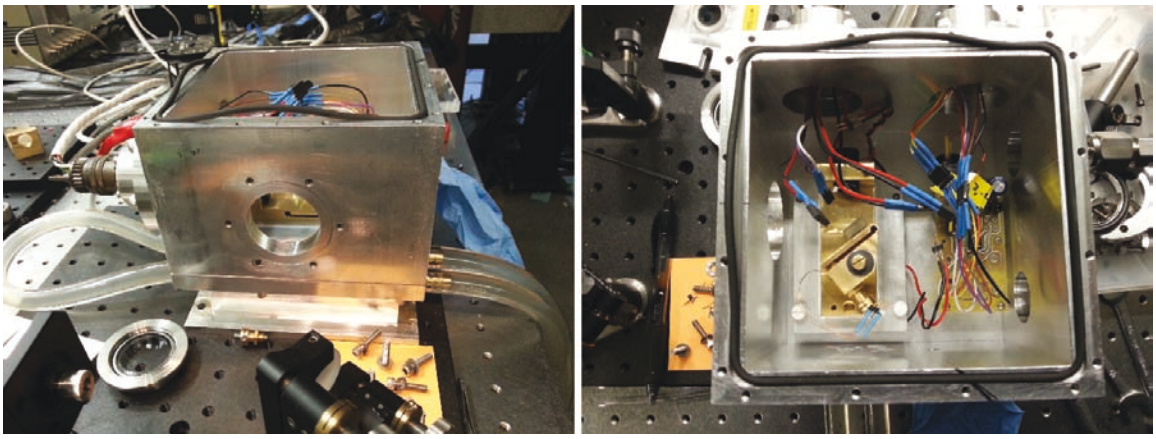

Figure 3.3.3: Side view and top view of single cold ECDL during assembly and alignment showing the water cooled based, vacuum compatible body, and internal layout of the electronics and ECDL.

lenses, I was able to couple the output of the system into a single mode fiber with 45% coupling efficiency.

3.3.2.3 Cryogenic ECDL system

In order to generate laser light for either the 1st or 2nd re-pumping transitions v_{10} and v_{21}, I constructed a pair of cold ECDL systems. The cold ECDL system is based on the HL63133DG diode from Thorlabs, which is rated for single mode operation at $\lambda = 638$ nm with a maximum output of $P_{\max} = 170$ mW. When cooled down to temperatures of $T = -20 - -40$ degree Celsius, the peak of the gain curve of this diode can be shifted to range of $\lambda = 626 - 629$ nm. This allows construction of a relatively high power solid state laser system suitable for use as a re-pumper. This system has the particular advantages of cost (<10k per system) and ease of maintenance when compared with the alternative dye laser system. My construction of these systems was based in a large part on [91]. This system is operated at 1 psi over pressure using dry nitrogen gas. It can also be operated in a vacuum environment for even lower

operating temperatures.

The laser enclosure is a fully vacuum compatible Al 6061 chamber with vacuum viewports and electrical feed-throughs. The enclosure is composed of three sections and have general dimensions approximately 6"x6"x6". The first is a base plate with four tapped and bored large diameter holes for water cooling. The second is the chamber body, with o-ring grooves for sealing on the top and bottom faces. On the sides of the chamber body are electrical, vacuum and gas, and optical feed-throughs/viewports. The top piece is either a 6"x6"x1/2" plexiglass cover for ambient pressure hermetically sealed operation, or a 6"x6"x1/2" Al 6061 piece for vacuum operation. Counterbored, tapped holes are made in the chamber body at 45 degrees and with normal incidence in the top plate for inserting of a 5/64" ball driver for alignment during cold operation. Sealing of these holes is accomplished used o-ring sealing screws. Purging the enclosure with dry gas during this procedure prevents water vapor from entering the enclosure.

Inside the enclosure is a modified version of the standard ECDL design used in the lab. The electronics PCB sits inside the enclosure and next to it is the diode mount. The diode mount is a standard Hänsch-style design used in the lab[92]. This mount sits on top of an adapter plate, which sits on top of two 2-stage high performance TECs (TE-2-(127-127)-1.15, max $\Delta T = 84$ K and $Q_{max} = 34$ Watts) which are wired in either parallel for Thorlabs ITC4005 driver, or in series for the Oven Industries home built current controller. The adapter plate is secured to the base plate using 4 thermally isolating Nylon screws. The TECs have the waste heat side down such that the heat can be carried away by water cooling of the base. The enter diode mount and grating holder are cooled by the TEC, and the laser light which bounces off the grating leaves the enclosure via the vacuum viewport. The TECs typically draw a

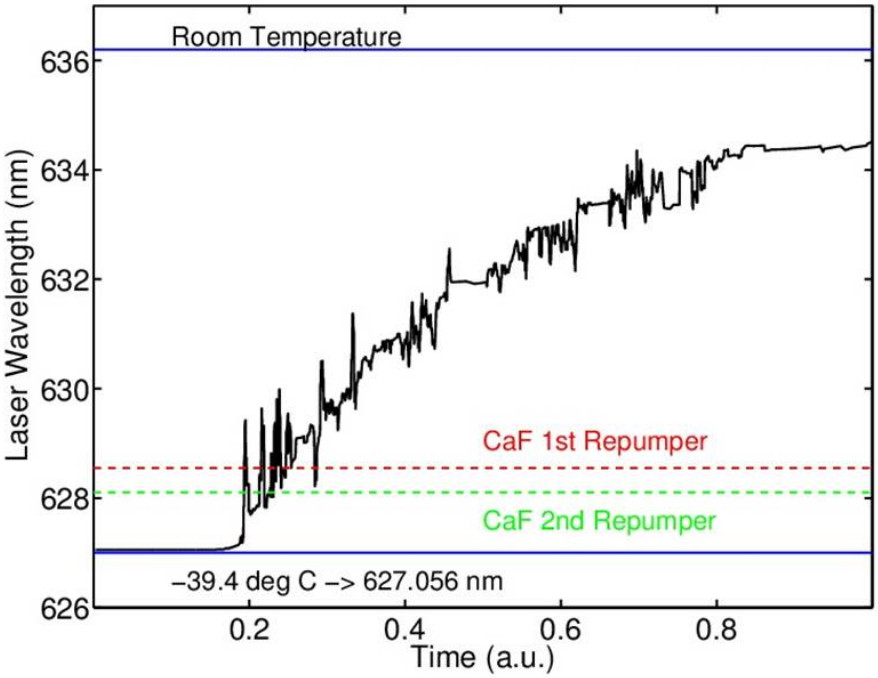

Figure 3.3.4: The temperature dependence of the output of a cold ECDL which is aligned at $\lambda = 627$ nm when the laser is cooled to a temperature of $T = -39.4$ degrees Celcius.

total current of $I = 5.5$ Amps to cool the diode and mount to $T = -30$ degrees C.

A single cold ECDL generates about $P = 100$ mW output power at current of $I \approx 180$ mA. The mode hop free tuning range is $\approx 2 - 5$ GHz. Using this system in a master-slave configuration allows the generation of nearly full power. A photograph of the master-slave system is shown in Figure 3.3.4.

3.3.2.4 Aculight OPO-SFG system

We recently purchased a commercial OPO-SFG system for the production of 606 nm light for the main line of the CaF MOT laser beams. The wonderful system by the company Aculight first generates a NIR photon via OPO using a periodically polled $LiNbO_3$crystal inside a bow-tie cavity. The OPO process is pumped with a

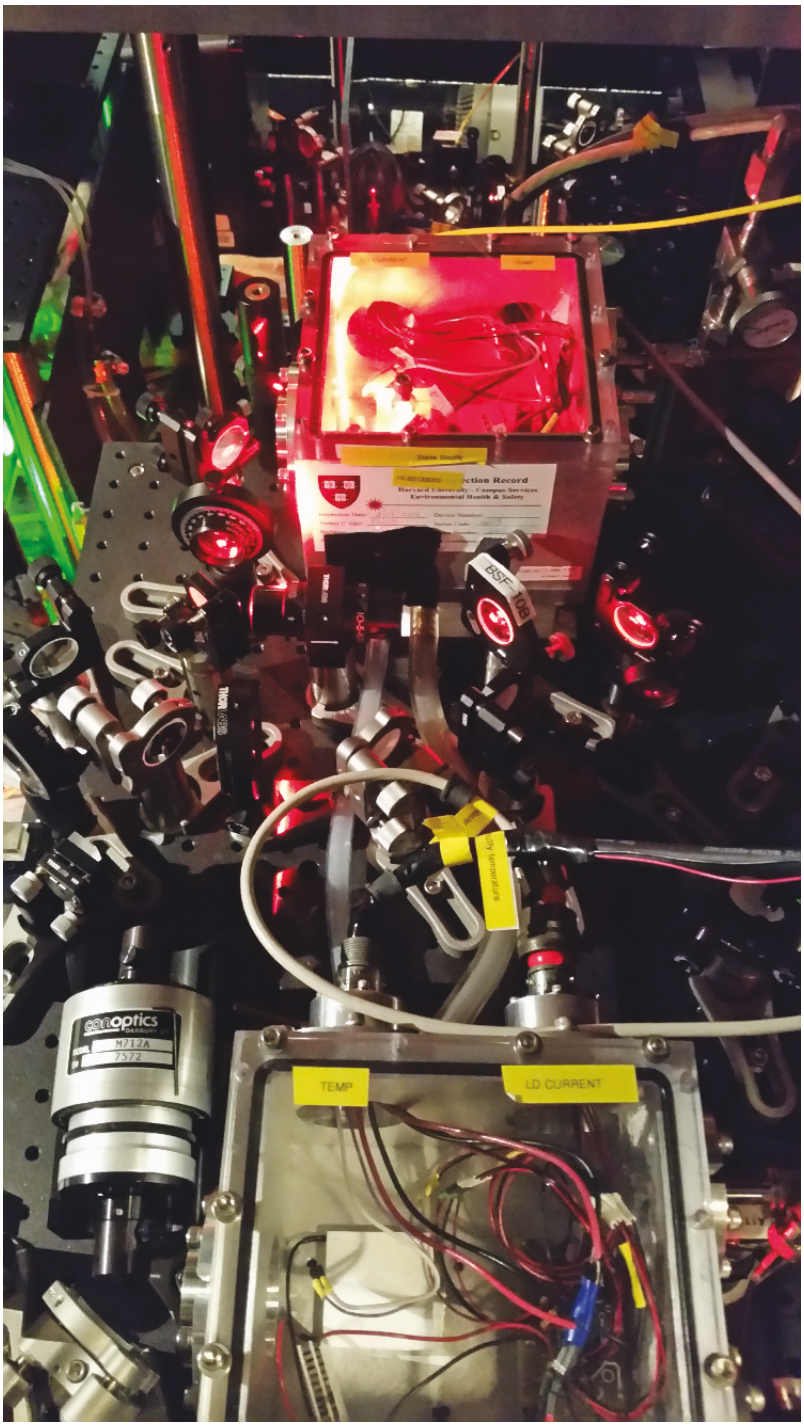

Figure 3.3.5: A photograph of the cold ECDL master-slave system. In the picture, the master laser (upper) is active, while the slave laser (lower) is inactive due to maintenance.

very narrow linewidth 1064 nm fiber laser which amplified by an IPG 15 W 1064 fiber amplifier. The OPO photon is then summed with the remaining pump light via sum-frequency generation using a second periodically poled stage on the crystal. The result is 1-2 Watt output at $\lambda = 606$ nm which is very stable and reliable, with line-width of less than 1 MHz and a mode-hop free tuning range of up to 20 GHz. Should additional funding be present, all dye lasers would be replaced with this type of system.

3.3.2.5 A very high index EOM for white light slowing

In order to achieve continuous slowing of CaF molecules, we decided to use the white-light slowing technique demonstrated by [63, 93]. Since fiber-EOMs are not available at the CaF main line wavelength of $\lambda = 606$ nm, we needed to design a free-space optical crystal high-index EOM. Thanks to helpful discussions with Phil Battle at Advr, we were able to design and produce such an EOM. I designed the crystal and driving circuit and I purchased the crystal. Aakash did most of the construction and testing of the EOM assembly - an impressive first project in the lab!

The white-light slowing techniques requires a coherent laser field with a frequency spectrum several hundred MHz in width with no gaps larger than the CaF A state natural linewidth of $\gamma = 6$ MHz. In order to accomplish this, we drive an EO crystal with a resonant frequency of $f \approx 5$ MHz with a modulation depth high enough to produce a spectrum a few hundred MHz wide. Consider a plane wave field which acquires phase at one position

$$E(t) = Ae^{-i\omega t}, \tag{3.3.1}$$

where A is the amplitude and ω is the frequency. An EOM can imprint additional phase onto the laser field by adjusting the index of refraction of the solid crystal

through which the field propagates. In particular, a sinusoidal modulation of amplitude β and at frequency Ω of the index of refractions modulates the phase of the field as

$$E(t) = Ae^{i\omega t + i\beta sin(\Omega t)}, \tag{3.3.2}$$

which, in the limit of small modulation depth β, produces sidebands at $\pm\Omega$ according to

$$E(t) = A\left(e^{i\omega t} + \frac{\beta}{2}e^{i(\omega+\Omega)t} - \frac{\beta}{2}e^{i(\omega-\Omega t)}\right) \tag{3.3.3}$$

. However, we are in the high modulation limit, and to solve for modulation spectrum, we can use the Jacobi-Anger expansion

$$E(t) = Ae^{i\omega t}\left(\sum_{k=-\infty}^{k=\infty} J_k(\beta)e^{ik\Omega t}\right), \tag{3.3.4}$$

where $J_k(\beta)$ is the kth order Bessel function of the first kind. For a modulation depth of $\beta = 15$ and a modulation frequency of $\Omega = 5$ MHz, the predicted line spectrum is shown in Figure 3.3.5.

This suggests that a modulation depth of $\beta \approx 10$ is sufficient to cover the estimated maximum slowing range of interest of $\Delta v \approx 200$ m/s.

For the design of our high-index EOM crystal, we need to calculate the modulation depth as a function of a applied field and length of the crystal. In a crystal lattice, the electric fields $\mathbf{D}$ and $\mathbf{E}$ are related by the dielectric permeability tensor ϵ as:

$$D_i = \Sigma_j \epsilon_{ij} E_j. \tag{3.3.5}$$

Along the principle axes of the crystal, this dielectric permeability tensor is diagonal with elements ϵ_{XX}, ϵ_{YY}, ϵ_{ZZ}. Normalizing the components of of the $\mathbf{D}$ field by

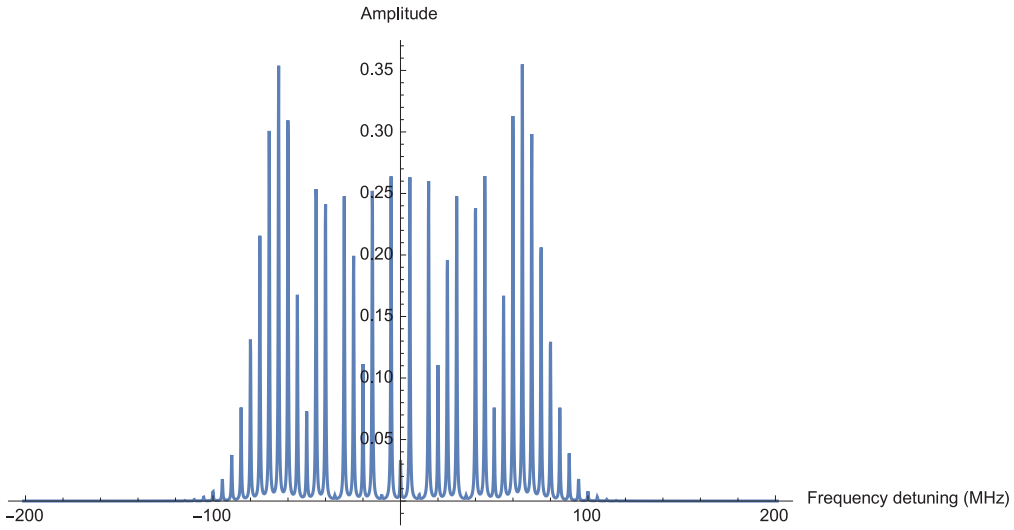

Figure 3.3.6: The predicted line spectrum of a highly modulated slowing laser beam using an input power of $P = 2$ Watts and $\Omega = 5$ MHz, assuming a $Q = 90$. This spectrum's width is approximately 200 MHz, which is sufficient to cover slowing across a range of $\Delta v \approx 200$ m/s.

the total energy of the wave, U,

$$X = \left(\frac{1}{8\pi U}\right)^{1/2} D_X \tag{3.3.6}$$

and so forth for Y and Z, we can write the surfaces of constant total energy in D-space as

$$\frac{X^2}{\epsilon_{XX}} + \frac{Y^2}{\epsilon_{YY}} + \frac{Z^2}{\epsilon_{ZZ}} = 1. \tag{3.3.7}$$

In an coordinate system not along the principle axes of the crystal, we can still write a similar equations using the indices of refraction n_i

$$\left(\frac{1}{n^2}\right)_1 x^2 + \left(\frac{1}{n^2}\right)_2 y^2 + \left(\frac{1}{n^2}\right)_3 z^2 + \left(\frac{1}{n^2}\right)_4 yz + \left(\frac{1}{n^2}\right)_5 xz + \left(\frac{1}{n^2}\right)_6 xy = 1 \tag{3.3.8}$$

The indices of refraction are modified by an applied electric according related to the electric permeability tensor. Specifically, using the reciprocal dielectric imperme-

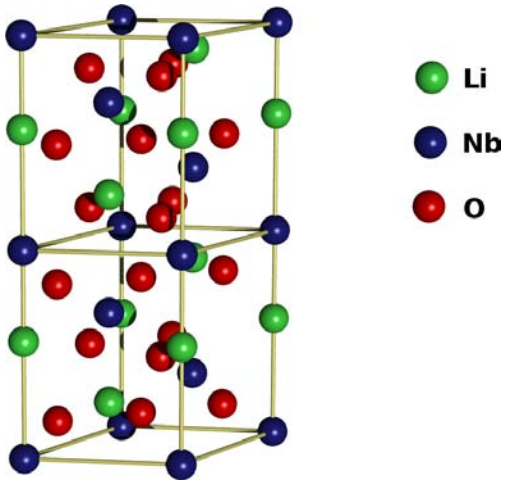

Figure 3.3.7: The unit cell of the material $LiNbO_3$ used for our custom high-index electro-optic modulator

ability tensor $\eta_{ij} = (\epsilon^{-1})_{ij}$ is altered by an electric field according to

$$\eta_{ij} = \eta_{ij}^0 + \Sigma_k r_{ijk} E_k + \Sigma_{kl} s_{ijkl} E_k E_l, \tag{3.3.9}$$

where $r_{ijk}$is the linear electro-optic tensor and s_{ijkl} describes the quadratic electro-optic effect, called the Kerr effect. This alters the index of refraction according to

$$\Delta \left(\frac{1}{n^2}\right)_i = \Sigma_j r_{ij} E_j \tag{3.3.10}$$

where r_{ij} is the contracted form of r_{ijk} using its real and symmetric properties, as described in [94].

The material $LiNbO_3$ is our choice for the EOM crystal. It has a large on-axis electro-optic $r_{33} = 30.9$ pm/V, a large dielectric constant of $\epsilon_1 = \epsilon_2 = 85$ and $\epsilon_3 = 29$, high extra-ordinary index of refraction of $n_e = 2.24$. It is generally prevalent in the electro-optics community due to these properties and is easily commercially available. The unit cell for $LiNbO_3$ is shown in Figure 3.X.X . $LiNbO_3$ has a crystal point group

$3m$. According to Boyd eq. 11.2.15, the contracted electro-optic tensor is

$$r = \begin{pmatrix} 0 & -r_{22} & r_{13} \\ 0 & r_{22} & r_{13} \\ 0 & 0 & r_{33} \\ 0 & r_{42} & 0 \\ r_{42} & 0 & 0 \\ r_{22} & 0 & 0 \end{pmatrix} \tag{3.3.11}$$

, where $r_{13} = 9.6$ pm/V, $r_{22} = 6.8$ pm/V, $r_{33} = 30.9$ pm/V, $r_{42} = 32.6$ pm/V, and the ordinary index of refraction is $n_0 = 2.34$. Returning to our optical index ellipse formalism above, we can compute the change in the ellipse due to an applied field using the contract tensor r_{ij}. For a static electric field applied along the z (3) axis of the crystal, the optical index ellipse is modified to

$$\left(\frac{1}{n_o^2} + r_{13}E_z\right)x^2 + \left(\frac{1}{n_o^2} + r_{13}E_z\right)y^2 + \left(\frac{1}{n_e^2} + r_{33}E_z\right)z^2 = 1 \tag{3.3.12}$$

I derived this calculation based off of a similar calculation for a different point group in Boyd chapter 11.2. In the case of z-polarized light, which attains the maximal electro-optic coefficient, the effective index of refraction is

$$\left(\frac{1}{n_e^2} + r_{33}E_z\right)z^2 = \frac{1}{n_z^2} \tag{3.3.13}$$

Solving this equation for n_z, we get

$$n_z = \frac{n_e}{\sqrt{1 + n_e^2 r_{33} E_z}} \tag{3.3.14}$$

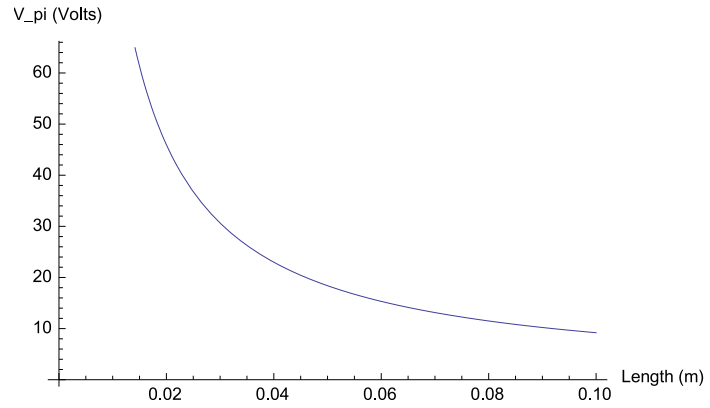

Figure 3.3.8: The modulation depth of a crystal of $LiNbO_3$for applied field along the z-axis with z-polarized light at $\lambda = 606$ nm and a thickness of $d = 1$ mm.

Assuming that $n_e^2 r_{33} E_z \ll 1$, which can use a Taylor expansion of $\frac{1}{\sqrt{1+x}} \approx 1 - x/2 + \ldots$ to get

$$n_z = n_e - \frac{1}{2} n_e^3 r_{33} E_z \tag{3.3.15}$$

Now, the differential phase accumulated by the laser field traveling in the x or y directions and polarized along the z direction through the crystal of length L, with an applied electric field E_z is

$$\phi = -n_e^3 r_{33} E_z \omega \times L/c \tag{3.3.16}$$

For a light field of frequency ω, which for the CaF main transition at $\omega = 2\pi \times 4.76 \times 10^{14}$ rads/sec. Thus, for a crystal of thickness d, the modulation depth in terms of V_π is

$$V_\pi = \frac{\pi d c}{n_e^3 r_{33} \omega L} \tag{3.3.17}$$

For a crystal thickness of $d = 1$ mm, this curve is plotted below in Figure 3.3.7.

Our design criteria was a modulation depth of $V_\pi = 20$ Volts, which is easily satisfied with a crystal length of $d = 5$ cm. We ordered a crystal $d = 6$ cm long just

to be sure.

The actual crystal which we ordered from Advr was a 0.9mm x 0.9 mm x 6 cm z-cut $LiNbO_3$ crystal with BBAR coating for a wavelength range of $\lambda = 500 - 700$ nm. The crystal has a thin (thickness $\sim$ 100 nm) gold coating on the z-facet with a thick copper layer (thickness $\sim$ 100 μm) on top for electrical contact, which was deposited by Advr.

Next, we require a resonant driving circuit which is capable of driving the crystal with a reasonable heat load. The conservative design goal for heat load was $P \lesssim 1$ Watt, based on discussion with Advr and Newport corporation. The basic design is to use a series RLC circuit driven using an impedance matching transformer. The capacitance of the EO crystal is given by

$$C = \frac{\epsilon_0 \epsilon_r A}{d}, \tag{3.3.18}$$

where $\epsilon_r = 78$, $A = 5 \times 10^{-5}$ m^{2}and $d = 1$ mm. This gives a crystal capacitance of $C = 3.8 \times 10^{-11}$ F. The crystal and contacts should have a resistance of $R = 10\,\Omega$ according the Advr. For our design frequency of $\Omega = 5$ MHz this give a required inductance of $L = 28.6$ μH and estimated $Q = 90$. To achieve a modulation depth of $\beta = 10$, this requires an input power of $P = 0.9$ Watts, within our design criteria. To calculate the required impedance matching transformer, we can calculate the impedance of the resonant circuit on resonance

$$Z = R + i\omega L + \frac{1}{i\omega C} = R + i\sqrt{\frac{L}{C}} - i\sqrt{\frac{L}{C}} = R = 10\,\Omega \tag{3.3.19}$$

Thus from a 50 Ohm BNC drive, we need a 5:1 impedance matching transformer. Aakash constructed the final EOM assembly and we took RF spectra of the resonant

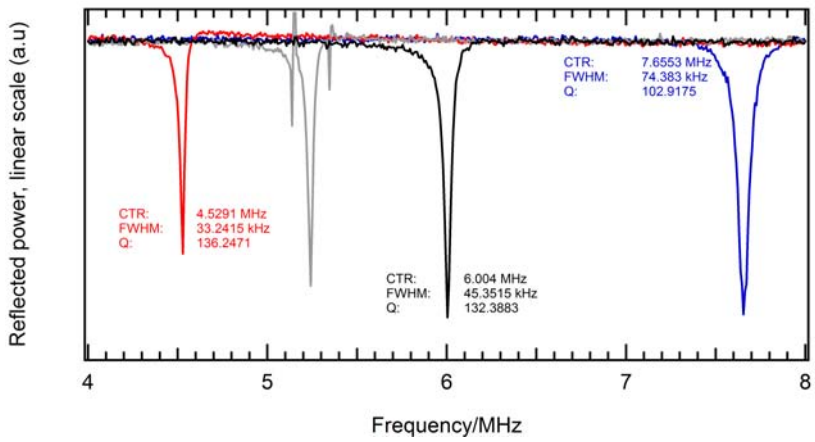

Figure 3.3.9: RF spectrum of EOM drive circuit at various resonant frequencies, which are set by a tunable capacitor.

circuit, which are shown in Figure 3.3.8

The actual construction of the EOM assembly is as follows. The EO crystal is placed in a 1/4 thick Al 6061 box approximately 8 cm x 4 cm x 6 cm (LxWxH). The resonant circuit is located inside the assembly along with the crystal. Electrical contact is made with the copper field layers using large gold coated spring loaded pogo pins. The pogo pins are mounted to the PCB board, which contains the resonant circuit, which itself is mounted to a vertical translation stage with accessible via a knob outside of the EOM box. This allows external actuation of the pogo pin compression force. The other copper field layer is directly contacted to the base of the Al box, which is grounded. The orientation of the crystal was initially controlled by PEEK shims, although in a later version those were removed due to damage from the laser when misaligned. A photograph of the assembly is shown in Figure 3.3.9.

We measured the spectra of the white light slowing laser broadened using the EOM driven at $\Omega = 4.5$ MHz as measured via a beat-note against a reference beam at a frequency shift of $\delta = 207$ MHz. The spectra is show in Figure 3.3.10.

To make sure that smaller peaks in the spectrum do not pose a 'hole' for the white

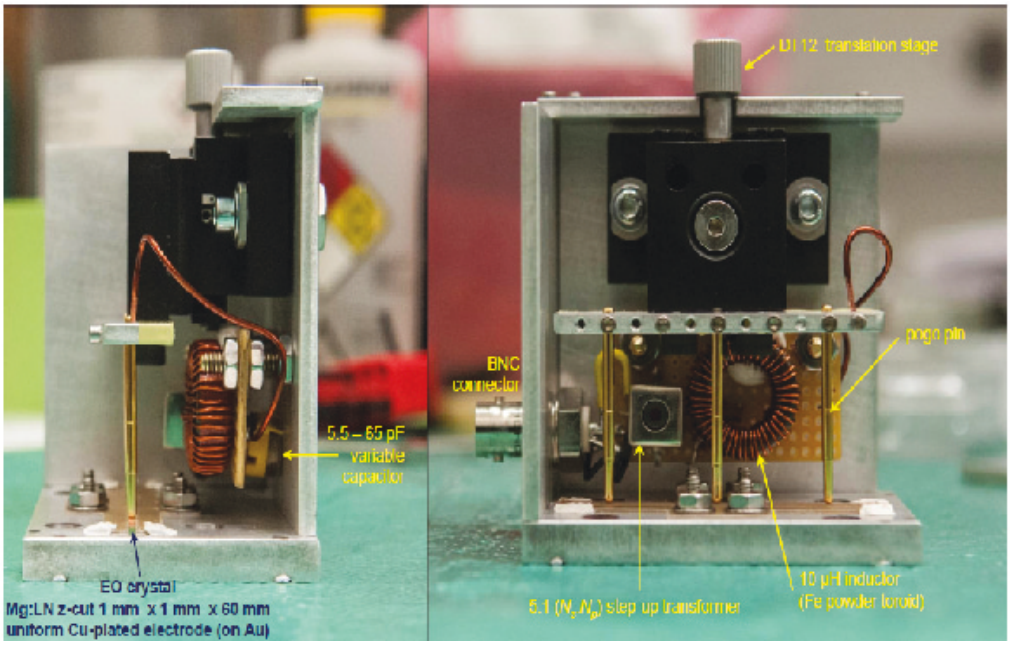

Figure 3.3.10: Photograph of the white light slowing EOM assembly with important components labeled. Photo credit: Aakash.

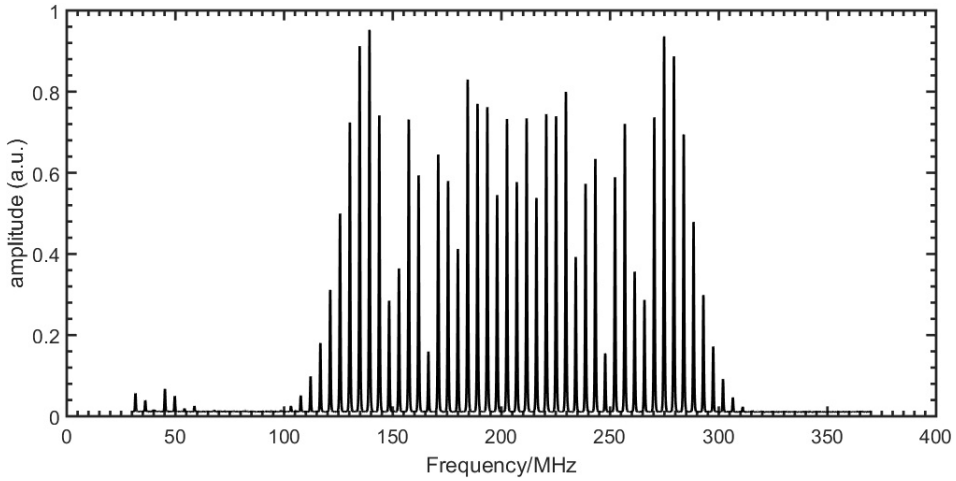

Figure 3.3.11: Spectrum of the 'white light' slowing laser produced by passing through the EOM at a drive frequency of $\Omega = 4.5$ MHz and a drive power of $P \approx 500$ mW.

light slowing, this light is passed through a second, low-index EOM at $\Omega = 25$ MHz to further broaden the spectrum and fill in an potential holes in the spectrum.

3.3.2.6 Detection system.

Detection is accomplished by imaging light from the MOT region onto two different detectors. A photo-multiplier tube (PMT) allows for high sensitivity and fast time response detection of emitted photons. An electron multiplying CCD (EMCCD) camera provides decent sensitivity spatial imaging at the cost of fast detection time. Two PMTs were used depending on whether we were collecting signal from the $A \rightarrow X$ transition or $C \rightarrow X$ transitions. For the visible orange photons of the $A \rightarrow X$ transition, we use a Hammamatsu R8900-U and for the UV photons of the $C \rightarrow X$ transition, we use a low dark-count Hamamatsu R7600P. The two detectors can function simultaneously as light from the imaging system is split on either a 50:50 beam splitter or dichroic mirror. Spatial filtering is accomplished by imaging the MOT onto a variable iris before re-imaging onto the detector. A 2" lens has been placed in the vacuum to improve collection efficiency, and the rest of the imaging optics are placed outside of the vacuum chamber. The signal can be processed both in a continuous current mode or a photon-counting mode. In the continuous current mode, the signal is sent through an SRS low noise pre-amplifier and then digitized with a NI DAQ system. If the PMT is being operated in photo counting mode, the signal is sent through a fast amplifier before being digitized and counted using an NI DAQ system.

3.3.3 In-vacuum magnetic field coils.

The rapidly oscillating anti-Helmholtz magnetic field for the AC MOT is provided by a pair of inductively coupled in-vacuum field coils which form part of a resonant circuit. The requirement of a substantial field gradient of ($\partial B/\partial z \gtrsim 10$ G/cm) in the 1-10 MHz range with low heat load to prevent out-gassing presents a challenging design requirement. The resonant frequency of the circuit is given by the familiar equation from high-school physics

$$\omega_0 = \sqrt{\frac{1}{LC}} \tag{3.3.20}$$

, where L is the inductance and C is the capacitance. For $\omega_0 = 2\pi \times 6 \times 10^6$ rads/s, this requires $LC = 7 \times 10^{-16}$ H $\cdot$ F. In addition, we want a Q as high a possible to reduce the heat load. The Q of an RLC circuit is

$$Q = \frac{\omega_0 L}{R} \tag{3.3.21}$$

. For a given resonant frequency, we want to have as small of resistance and as large of inductance as possible. This sets a clear design strategy - choose the smallest possible C and largest possible L whose combination gives $LC = 7 \times 10^{-16}$ H $\cdot$ F. This strong inductive coupling of the coils is accomplish by placing the coils within a few cm of each other. These coils were designed initially by Jun Ye's group at JILA and later modified in several stages by our group. An initial design of the coils was based on copper traces on an FR-4 PCB. Each coil was composed of two boards with traces on both sides (4 total traces) with 1/16 inch boron nitride (BN) layer sandwiched in between for thermal conductivity. Amorphous α-BN is an electrical insulator with a thermal conductivity of 3 $\mathrm{Wm^{-1}K^{-1}}$. In this design, heat was conducted away from

boards to an in-vacuum water cooling block.

In our re-design, the BN layer was replaced by a sintered Alumina board with thermal conductivity ten times higher than that of BN. Additionally, a fully UHV compatible design was achieved by fabricating the coils directly from bulk copper using electric discharge milling. These coils were cut from a bulk copper sheet 0.85 mm in thickness, which is much thicker than the printed FR-4 copper traces. The newer coils had 6 turns for each coil with an inner diameter of 1.5 cm, an outer diameter of 3 cm, and only two coils per board. The distance between each board is approximately 1.2 cm. This allows for small MOT beams of diameter $d \approx 1.0$ cm. Bonding of the coils to the board was tested using various methods, including UV-curing UHV compatible Opto-cast epoxy and Torr-seal epoxy. However, the most robust bonding was achieved with Stycast 2850, which remarkably turned out to be UHV compatible! The combination of these design features results a substantially reduced heat load and allows cooling to occur using an ultra-high current electrical feed-through as a thermal feed-through to air. Under normal operating conditions, the coil temperature increases by no more than 1-3 degrees C over room temperature. To ensure optimal vacuum properties, the coils are baked at 120 C for several hours before use in the chamber.

The resulting electrical properties of the coils are estimated to be a capacitance of $C = 10^{-10}$ F, an inductance of $I = 2.8 \times 10^{-6}$ H, and a resistance of $R = 0.3$ Ohms. Impedance matching is accomplished by a vacuum high voltage variable tuning capacitor and a tuning inductor. Under optimal impedance matching, a roughly 2 A input current gives a peak to peak voltage of 55 Volts. The field gradient in the MOT region was measured with a Hall probe to up to 20 Gauss/cm along the inter-coil axis at this input current. This gradient is enough to even trap Yb atoms in the AC

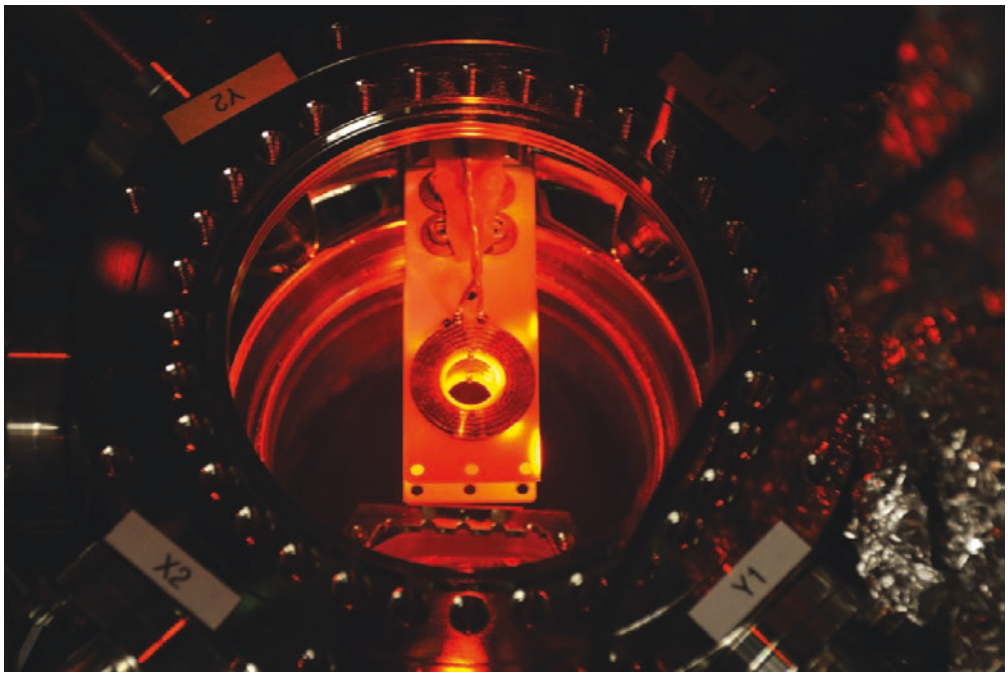

Figure 3.3.12: A photograph of the MOT coil assembly inside the UHV MOT chamber. The coils are illuminated by the MOT cooling beams.

configuration. Figure 3.3.11 shows the MOT coil assembly instead in the UHV MOT chamber.

3.3.4 Pockels-Cell for polarization switching

The Pockels-Cell for polarization switching was a commercial system from Conoptics. In particular, the cell itself is a Model 350-160-01-RP EO Modulator which is driven by a Model 25D driver, both from Conoptics. This cell works perfectly and the results of a switching test are shown in Figure 3.3.12

3.3.5 AOM breadboard for hyperfine structure

In order to close the hyperfine structure of CaF, we use a system of AOMs to generate frequency components on the laser with the exact hyperfine splittings. A schematic

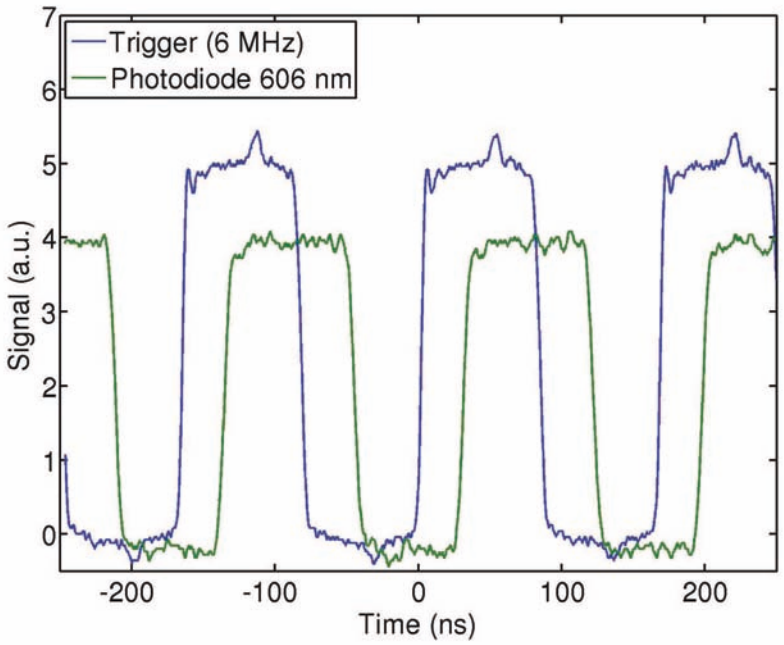

Figure 3.3.13: The output of the Pockels cell after the built-in polarizing beamsplitter cube when driven by the Conoptics driver at 6 MHz. In practice, a quarter-wave plate rotates this into polarization which switches from $\sigma+$ to $\sigma-$ polarization. Extremely high extinction of over 95% can be achieved.

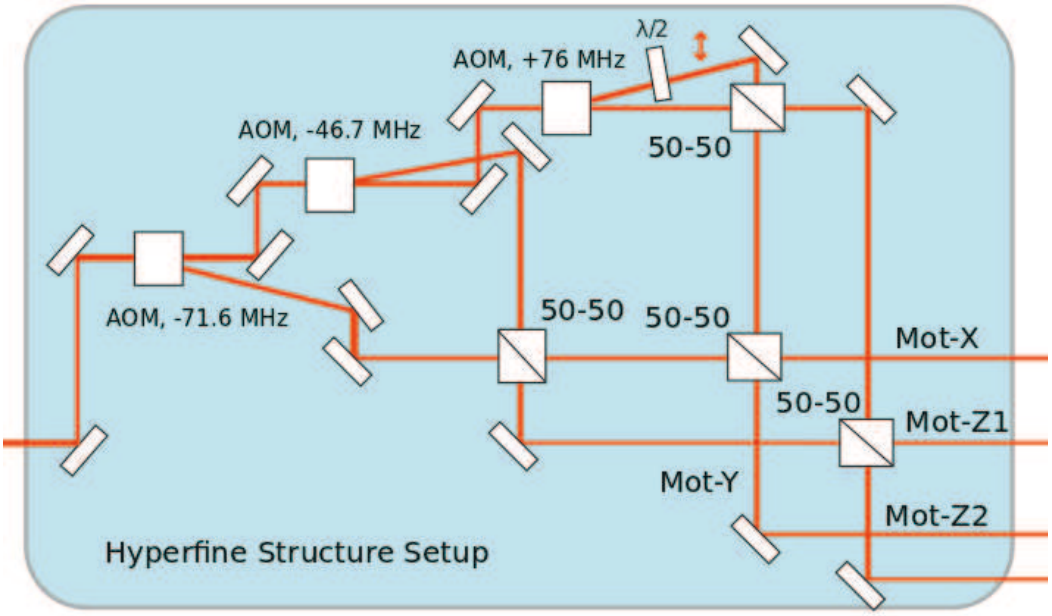

Figure 3.3.14: A schematic of the AOM optical system for re-pumping the different hyperfine states in the ground electronic state of CaF,

of this system is shown in Figure 3.3.13.

3.4 White light slowing of ^{6}Li

White light slowing of ^{6}Li was achieved using the D2 line from both a thermal oven source and a buffer-gas beam source. The first indication of what light slowing came from a longitudinal slowing measurement from the thermal oven. A forward velocity measurement of the oven source was made with the slowing laser applied. The slowing laser was modulated using the white light EOM at varying RF powers and we observed a depletion of faster molecules and an accumulation of slower molecules. Additionally, a hyperfine re-pump was added to this beam with an AOM at $f = 228$ MHz. The range over which is depletion grows as a function of the driving power (frequency width) of the white light EOM. Figure 3.4.1 shows the velocity spectrum of the

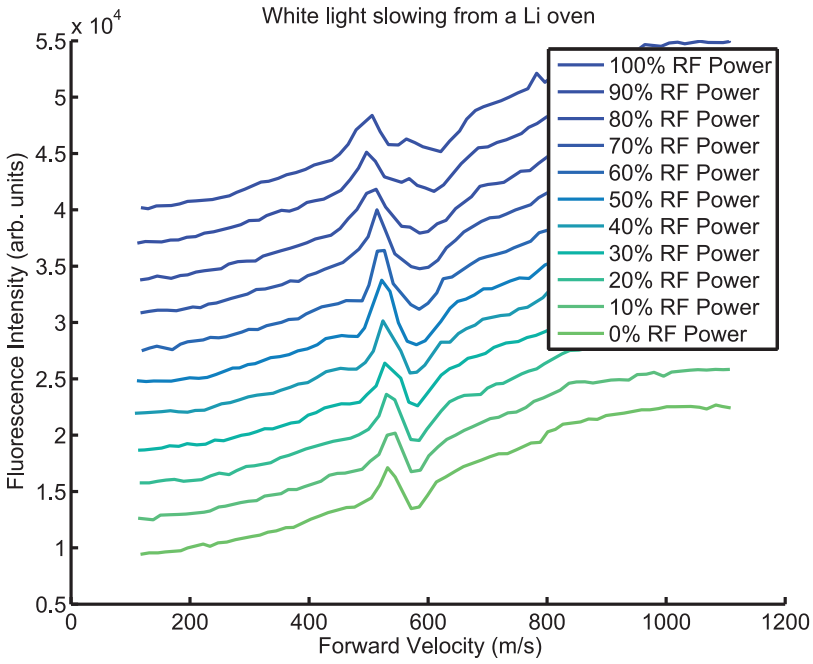

Figure 3.4.1: White light slowing of ^{6}Li from a thermal beam as a function of RF drive power to the white light EOM. A separate re-pumping beam was used as driven by an AOM at $f = 228$ MHz.

thermal ^{6}Li beam as a function of the EOM RF drive power. The slowing laser power for this measurement was approximately $P \approx 7$ mW with 10% at the re-pumping frequency.

As a result of the very small mass of a lithium atom, the thermal velocity of a lithium atom is very high ($v_f \approx 100$ m/s at 4K). A buffer-gas beam has a forward velocity which is strictly higher than the thermal velocity, and the light lithium atom is strongly boosted by collisions with the helium atoms of the buffer-gas cell. We produced a buffer-gas beam at $T = 2$ K using a two-stage cell with a peak forward velocity of $v_f \approx 150$ m/s. In order to test the AC-MOT on ^{6}Li, white-light slowing was needed to achieve a trappable forward velocity. The very next day after observing white-light slowing in the thermal beam, we observed white light slowing of the buffer-

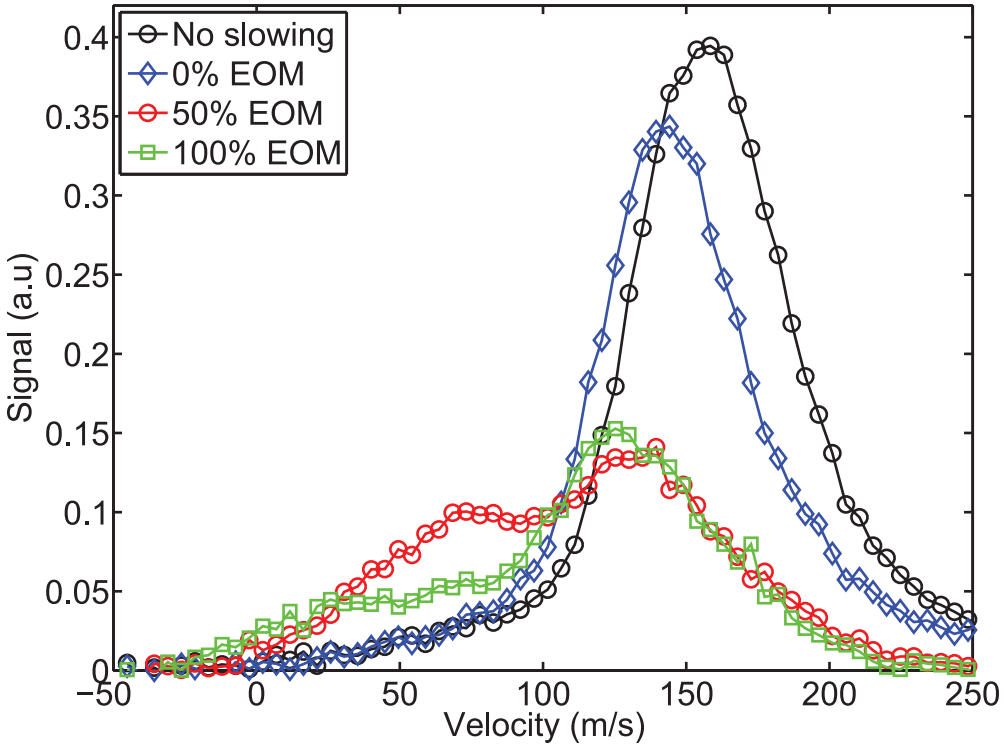

Figure 3.4.2: Velocity spectrum of a ^{6}Li buffer-gas beam undergoing white light slowing as measured in the MOT region approximately 1 m in distance from the cell. The percent EOM corresponds to the fraction of the full RF drive power of the EOM, which is approximately $P \approx 500$ mW. The velocity spectrum is integrated from approximately $t = 500$ μs

gas beam. The results are shown in Figure 3.4.2 and Figure 3.4.3. An unbroadened slowing laser makes a small shift in the velocity distribution. Turning on the EOM to 50% and then 100% of full power, for lack of a better technical term, blows the beam away. Very slow atoms are present, and we even detect atoms turned completely around when using the full drive power of the EOM. The laser power used for this measurement was 35 mW total.

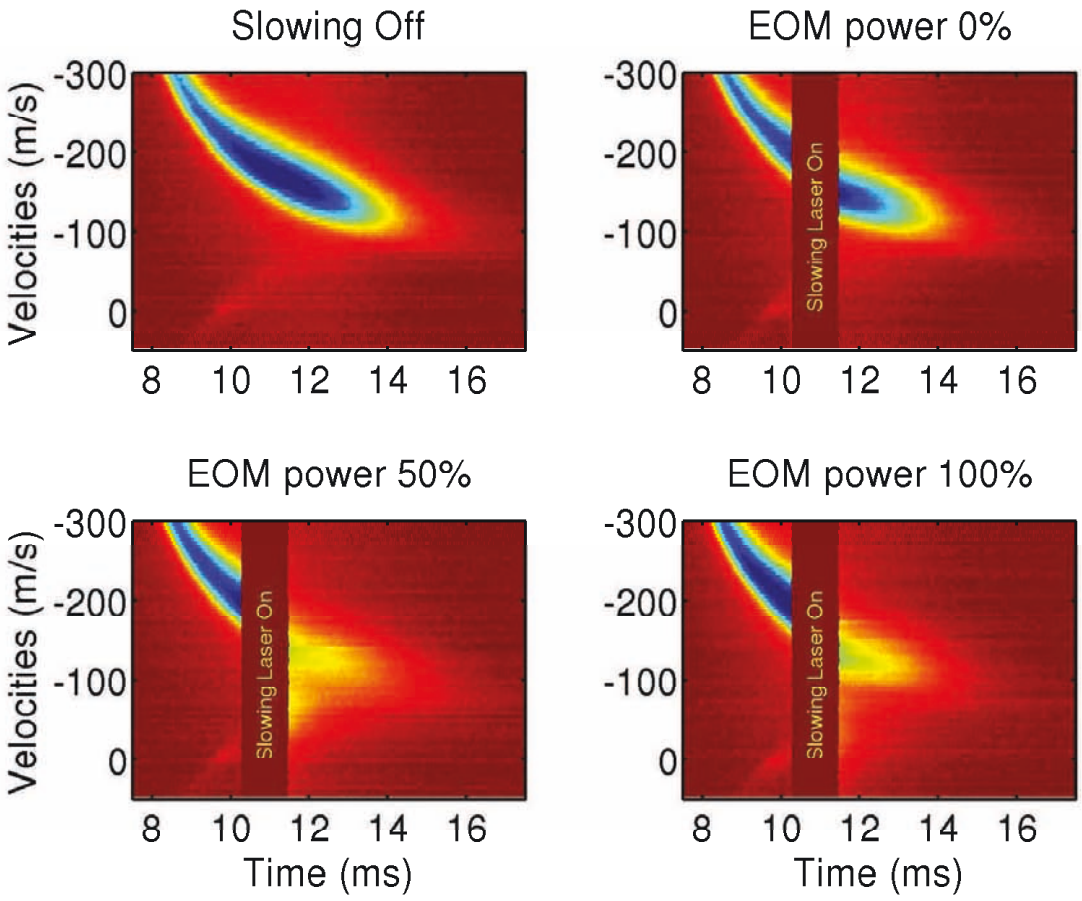

Figure 3.4.3: The velocity spectrum of the^{6}Li buffer-gas beam in the MOT center as a function of arrival time after YAG pulse. Blue corresponds to atomic signal. The dark red region labeled 'Slowing Laser On' represents the time window for the application of the slowing laser. Notice that very slow molecules are only seen immediately after the application of the slowing laser. This suggests that the slowing only occurs in the longitudinal distance immedeatly before the MOT center.

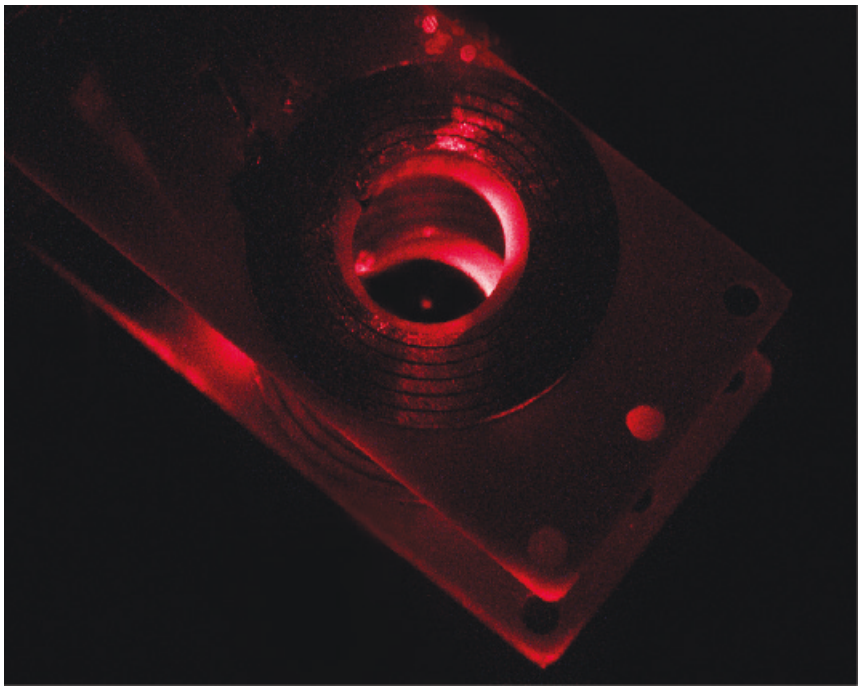

Figure 3.5.1: Camera imagine of a ^{6}Li DC-MOT on the D2 line from a buffer-gas beam source using the in-vacuum MOT coils. The MOT is visible as the small red sphere in the center of the coils.

3.5 AC-MOT of ^{6}Li

Using the very slow Li beam that we created using the white light slowing, we were able to then achieve an AC-MOT of ^{6}Li from a two stage buffer-gas beam source. Our goal was to study the properties of the AC-MOT of lithium on the D1 line, as well as try to make a DC-MOT of lithium on the D1 line. First, we were able to load a DC-MOT on the D2 line using the white light slowing. Figure 3.5.1 shows a cell-phone camera image of the ^{6}Li DC-MOT on the D2 line. After optimizing the parameters here, we moved on to studying MOTs on the D1 line. We successfully achieved both an AC-MOT and a DC-MOT on the D1 line. The time traces of the Li beam, the DC-MOT, and the AC-MOT using the D1 line are shown in Figure 3.5.2. The AC-MOT is substantially stronger and more robust than the DC-MOT. We trap an order of magnitude more atoms (est. 10^6 atoms in the AC-MOT) with at least an order of magnitude long lifetime (est. lifetime $>$ 500 ms) in comparison the almost non-existent DC-MOT.

We studied the dependence of the trapped atom number and lifetime of the AC-MOT as a function of magnetic field gradient, AC switching frequency, buffer-gas flow rate, and YAG energy. The results of these studies are shown in Figure 3.5.3. The only strong trend is in the atom number as a function of magnetic field gradient. The capture velocity of the MOT is significantly influenced by the average scattering rate an incoming atom experiences as it travels through the laser beam. Given the small 1.0 cm diameter of the MOT beams, a field gradient of several times the linewidth still makes a significant increase in the total momentum transfer as the atom passes through the beams. A weak, but likely still significant effect on the lifetime results from an increase in the switching frequency of the MOT.

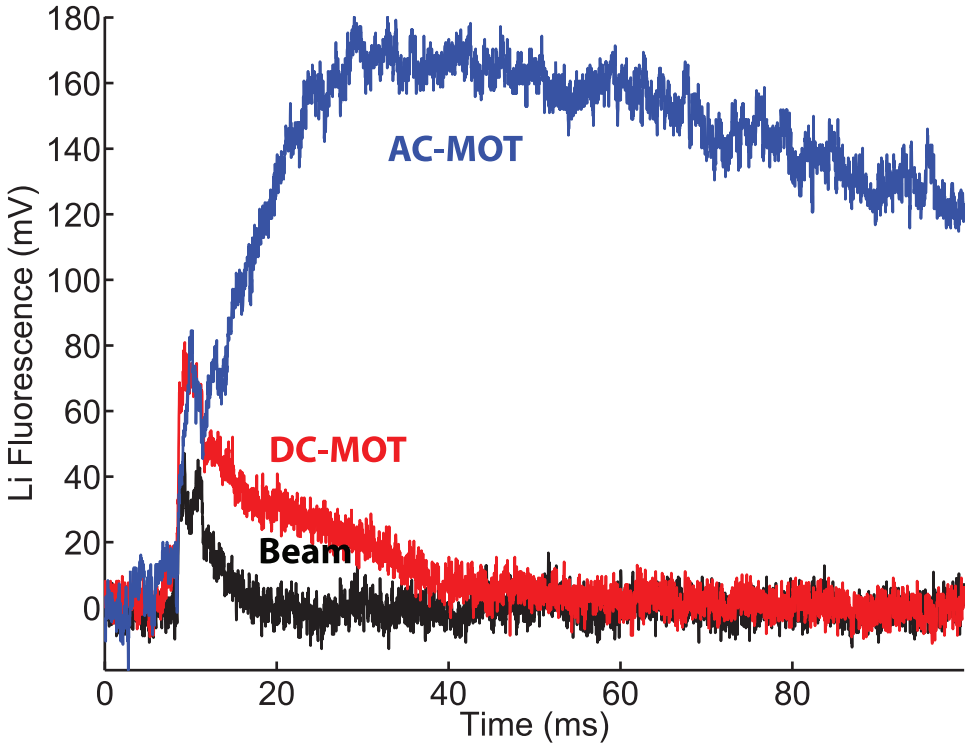

Figure 3.5.2: Comparison of the AC-MOT (blue), DC-MOT(red), and buffer-gas beam fluorescence signals using the D1 line as a function of time. The experimental parameters for these traces are a buffer-gas flow of 3 sccm, a YAG energy of 15mJ, a repetition rate of 1.17 Hz, and a cell temperature of $T = 2$ K.

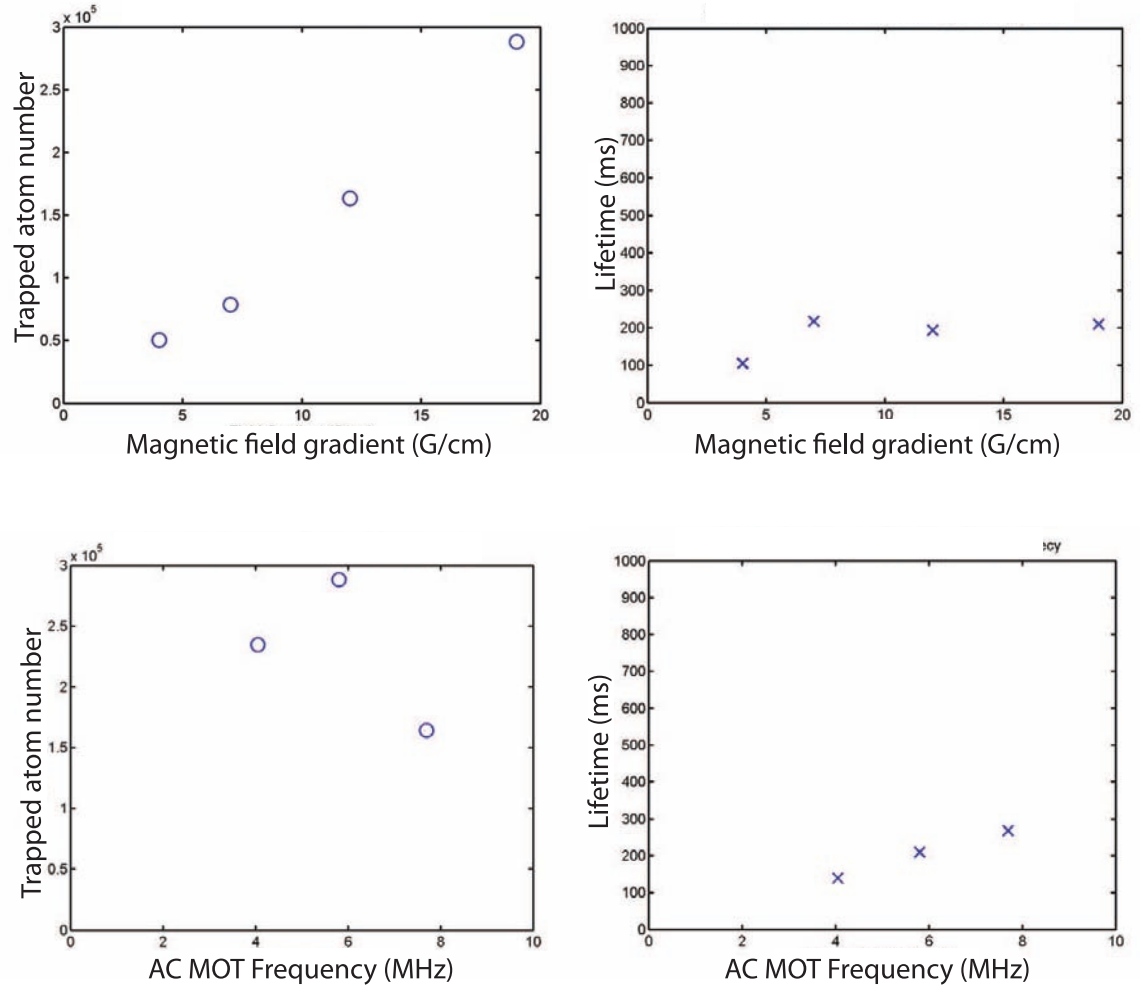

Figure 3.5.3: The trapped atoms number depends strongly on the magnetic field gradient, while no significant difference is observed as a function of the MOT switching frequency. The lifetime of the MOT experiences a slight increase with field gradient, and a significant increase in lifetime as a function of switching frequency.

3.6 Laser Slowing of CaF

Laser slowing of CaF was recently accomplished using the scheme and apparatus discussed above. I was not part of the experiment by the time a consistent laser slowing effect was observed, and a lot of work went into improving the detection scheme, polarization stability of the slowing laser, and carefully optimizing the optical alignment and parameters using the optical pumping and population transfer using the slower lasers. The experiment is still uncovering and overcoming technical challenges associated with the repeatability and control of the laser slowing. I want to briefly show some results which have been achieved with the laser slowing of CaF to highlight how our understanding of laser slowing has evolved. Some of these results I was part of and some I was not directly involved with.

The first set of effects which we were able to demonstrate was a successive increase the number of photons scattered by the beam by first closing the hyperfine structure, then by remixing projection dark states, then by apply the vibrational re-pump lasers. The effects of closing each of these leakage channels is shown in Figure 3.6.1. By observing a fluorescence enhancement with the second vibrational re-pump laser, we knew that some we were scattering over 1000 photons under ideal conditions. We studied the magnitude of the re-pumping effect in various ways, and the most interesting thing we learned was of the power requirements of the vibrational re-pumpers. While a saturated intensity for the main line was measured to only be $I_s \sim 1 - 10$ mW/cm^2, the saturation intensity of the first vibrational re-pumping laser was observed to be much higher, $I_s \approx 200$ mW/cm^2.

Ultimately, with careful optimization, laser slowing of CaF was achieved. The experimental configuration for these measurements is shown in Figure 3.6.2. Figures 3.6.3 and 3.6.4 show the time dependent forward velocity measurements with and

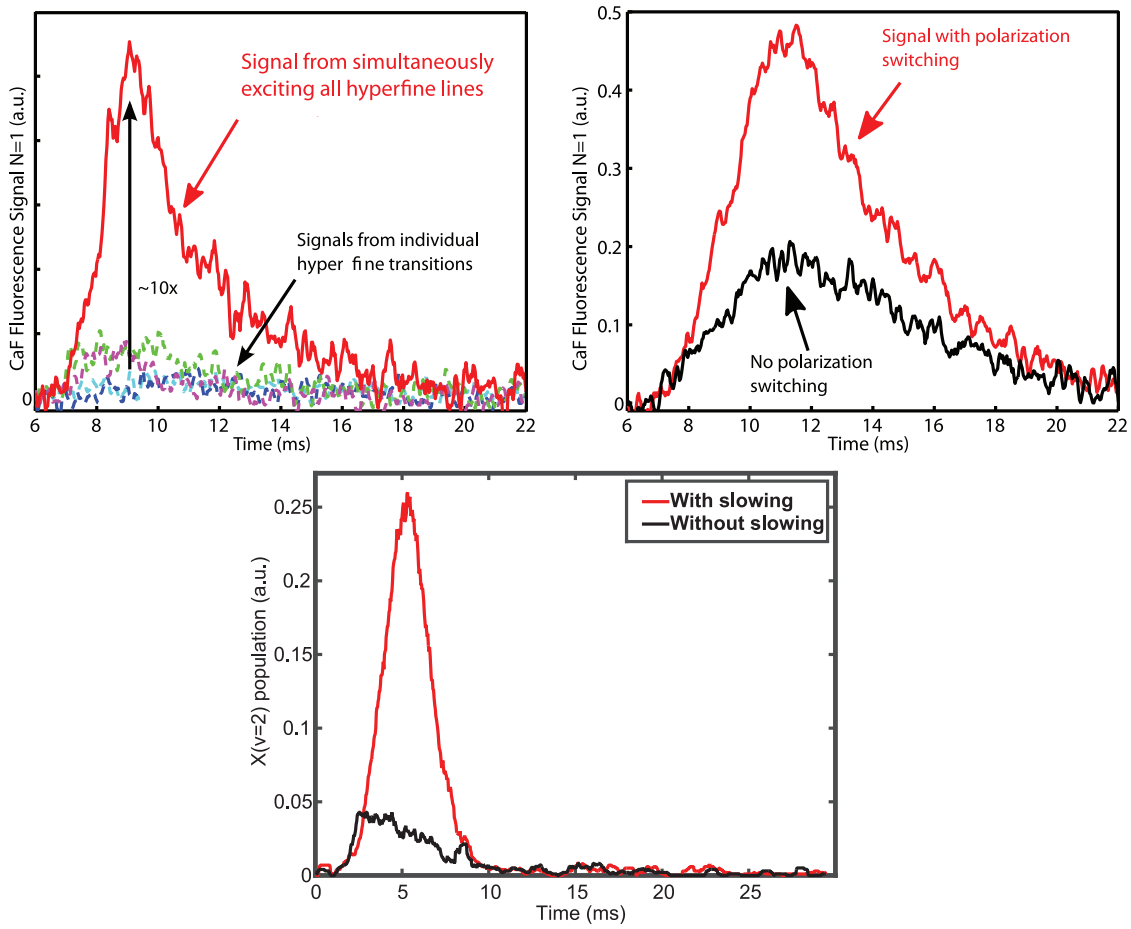

Figure 3.6.1: The effects of closing the various leakage channels in the photon-cycling scheme for laser slowing. First the fluorescence signal can be enhanced by 10x over a single hyperfine state by pumping all four ground state hyperfine states simultaneously. The magnetic dark states can be remixed, in this case we demonstrated a factor of 2 increase the fluorescence signal using the polarization switching method. Finally, the vibrational re-pump lasers can be added to recover leakage to off-diagonal vibrational states.

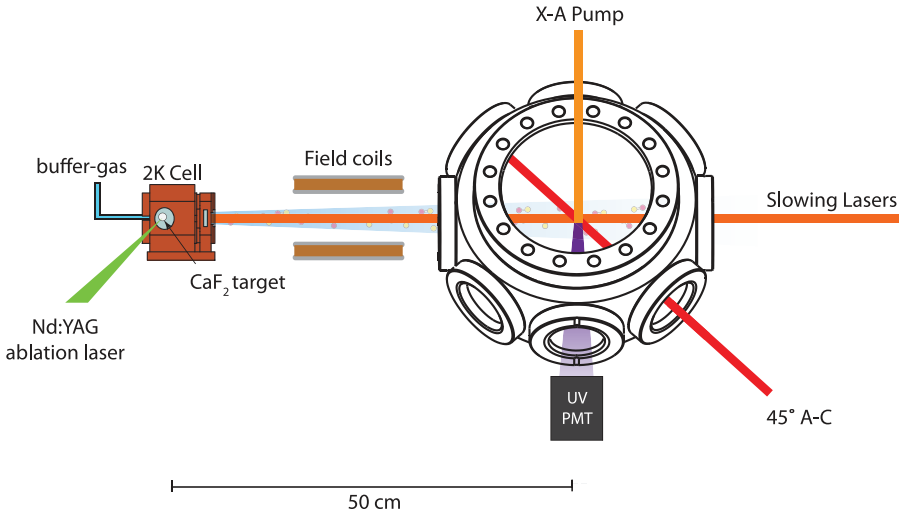

Figure 3.6.2: Experimental configuration for the laser slowing of CaF.

without the presence of the slowing laser, as well as an integrated forward velocity measurement. A depletion of faster molecules is observed, as well as a significant increase in the presence of molecules with a velocity between $v = 0$ m/s and $v = 80$ m/s. A close investigation of the very slow portion of the distribution shows the presence of molecules with forward velocities as slow as $v_f = 5$ m/s, below the predicted capture velocity of the molecular MOT. The number of molecules below the capture velocity $v_f = v_c = 10$ m/s is estimated to be ≈ 500.

A hallmark signature of slowing is the arrival of molecules in the MOT region in a time shorter than it would have taken a free-flying molecule to arrive at the MOT. This can only result from molecules which spent some time flying faster, but then were slowed just before the MOT region. The strong presence of this effect suggests that molecules are being slowed almost entirely just before the MOT center. Current efforts to produce an AC-MOT of CaF in the lab are on-going by my adept former teammates Eunmi, Aakash, Loic, and new-comer Ben.

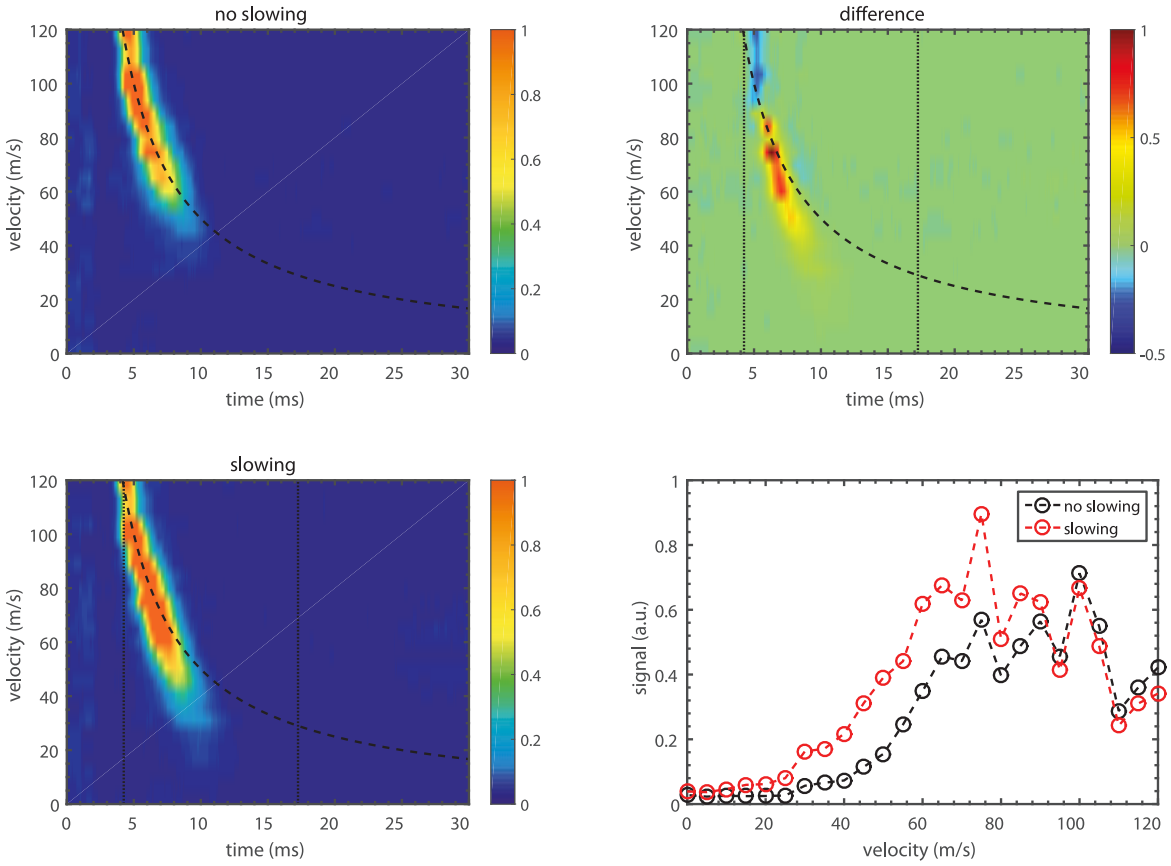

Figure 3.6.3: Velocity spectra of the CaF buffer-gas beam as a function of time without and with application of all slowing lasers. The difference of the two time dependent spectra (red is accumulation, blue is depletion) is shown in the upper right plot and the bottom right plot is a time integrated plot of the without and with slowing measurement with the integration window from $t = 2$ ms to $t = 50$ ms.

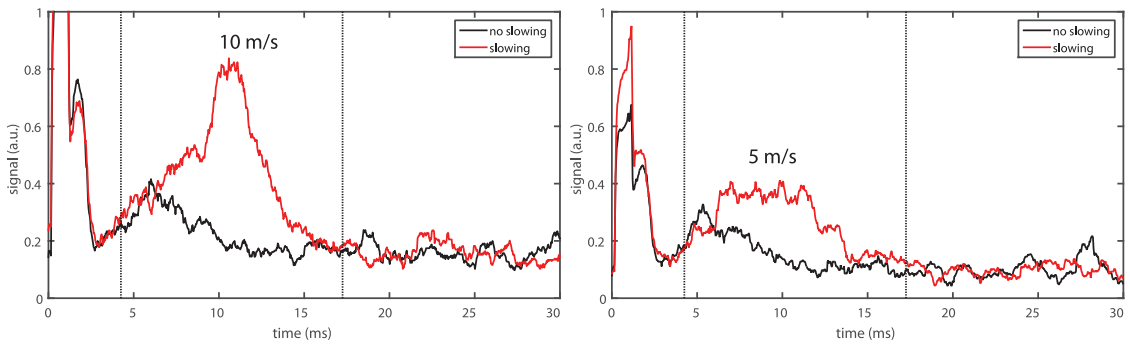

Figure 3.6.4: Time traces the fluorescence signal of the $v_f = 10$ m/s and $v_f = 5$ m/s velocity classes in the MOT center. Significant accumulation of slowed CaF molecules is present below the estimated capture velocity of the molecular MOT. Vertical lines indication the time window during which the slowing laser is applied.

Chapter 4

Cold, Large Molecules

The cooling of cold gas-phase large molecules and applications of such gasses can be used to address fascinating questions relevant to both physics and chemistry. For many decades, spectroscopy and chemistry of cold large molecules has been studied using seeded supersonic beams. Recent developments in cooling and beam production methods for large molecules have led to an exciting renaissance in the studies of spectroscopy, chemistry, and physics using cold large molecules. In this chapter of my thesis, I will give a brief introduction to some of the new developments, ideas, and questions in the field of cold large molecules.

4.1 A powerful quantum system

What constitutes large for a molecule, or any quantum system, is a flexible definition. Here, we define a large molecule as one with greater than 3 atoms and whose rotational properties are *generally* described as an asymmetric top. Many of the types of molecules that have been studied are organic (carbon-containing), and in an alternative defintion would be classified by organic chemists as small molecules. In contract,

linear molecules, such as CaF and SrOH, exhibit a much less rich rotational spectrum than the asymmetric tops discussed in this chapter.

4.1.1 Large Quantum Systems and Cooling

Large quantum systems have garnered significant recent attention in physics and chemical physics. A key open question in this field is over what mass and complexity scale does quantum mechanics behave consistently. For example, it is unknown how quantum mechanics interfaces with gravity in significantly massive objects. Can a quantum superposition state made in a system containing 10^{10} atoms? What about 10^{17} atoms? A Physics Today article[95] discusses how physics research in large quantum systems is divided into two categories.

One category is a top-down approach, and involves the fabrication and precision study of femto-nanogram scale massive objects. The other approach, deemed bottom up, seeks to study quantum mechanical behavior in ever-larger molecular systems. In the 'top-down' approach, laser cooling of the motion of a picogram-scale object through opto-mechanical coupling has recently been achieved[96]. These opto-mechanical systems have applications that range from fundamental tests of quantum mechanics at large masses to the detection of quantum gravity[97]. In the bottom-up approach, quantum mechanical interference of large organic molecules has been observed in molecules containing nearly one thousand atoms[98].

In the work presented in this thesis, we seek to not only study the external quantum mechanical properties of large molecules, but to also manipulate and study the internal quantum mechanical properties of large molecules. The full Hamiltonian of a large molecule is relatively well-known. However, these Hamiltonians can contain hundreds of degrees of freedom, even excluding electron degrees of freedom.

Thus, precise energy levels are difficult to calculate. Simpler models called effective Hamiltonians can be formulated, whose parameter can be measured using precision spectroscopy. While measuring the structure of a large molecule is a challenging task, control over its many degrees of freedom is even more difficult. As in the case of diatomic molecules discussed in the preceeding section, at the cost of such difficult comes the benefit of powerful applications, many of which will be discussed below. Thus, quantum mechanical control over the internal degrees of freedom of a large molecule is an exciting goal for both physics and chemistry purposes[30].

In particular, the cooling of a molecular system becomes more 'efficient' as the molecular system increases in size. This is due to two factors. The first is due to increased density of rotational states. The rotational Hamiltonian for an asymmetric top molecule is

$$\hat{H} = \frac{P_x^2}{2I_x} + \frac{P_y^2}{2I_y} + \frac{P_z^2}{2I_z} \tag{4.1.1}$$

[99]. As the molecule becomes larger, the moment of inertia increases. Assuming a fixed shape and constant density, the moment of inertia grows with mass as $I \sim M^{5/3}$. Consider the case of a molecule which behaves as a symmetric top. The energy of a symmetric top state $|J, K, m_J\rangle$ is

$$E = hBJ(J+1) + h(C-B)K^2, \tag{4.1.2}$$

where $B = \frac{\hbar^2}{2I_B}$ and $C = \frac{\hbar^2}{2I_C}$, J is the total angular momentum quantum number, and K is the projection of the total angular momentum along the symmetry axis. The total number of occupied rotational states for a symmetric top is therefore

$$\sum_{J,K \text{s.t.} \mathrm{E}<\mathrm{k_B T}} J \times (2J+1) \times (2J+1) \tag{4.1.3}$$

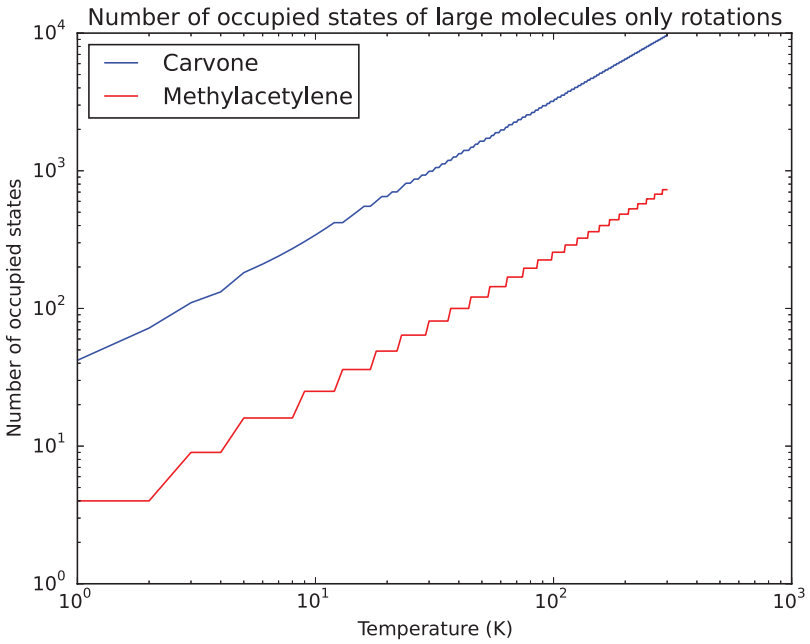

Figure 4.1.1: The number of occupied rotational states of two methylacetylene and carvone as a function of temperature.

For larger molecules, exponentially more rotational states will be populated at a given temperature. Consider the case of carvone, a 25 atom small molecule with a mass of 150 a.m.u. and well-studied biological properties - in particular (-)-carvone is the active taste component of spearmint. Carvone is an asymmetric top molecule with rotational constants $A = 2237$ MHz, $B = 656$ MHz, and $C = 580$ MHz[100]. Here we assume that $C = B = 656$ MHz for the purpose of the following calculation. If only rotational states are considered, the number of states of carvone below the thermal energy is shown below in Figure 4.1.1. Alongside the carvone curve is the curve for methylacetylene, a much smaller ($m_{\text{methylacetylene}}/m_{\text{carvone}} = 0.27$) symmetric top organic molecule used in the work described in this thesis. For only rotational states, $n_{\text{m.a}}/n_{\text{carvone}} \approx 0.065$.

In addition to rotational states, as a molecule grows larger, the number of vibra-

tional modes increase. A molecule with N atoms will have $3N-6$ normal modes of vibration ($3N-5$ for a linear molecule). In addition, as the molecule grows larger, the energy of lowest vibrational mode grows larger. The combination of these factors means that larger molecules occupy many more states for a given temperature compared to a smaller molecule. The comparative number of states below the thermal energy for carvone and methylacetylene, with vibrational states included, is shown in Figure 4.1.2.

Here, $n_{\mathrm{m.a}}/n_{\mathrm{carvone}} \approx 0.01$. For these calculations, I used the measurements of the vibrational spectrum of carvone from Mineyama et al. [101]. These curves imply that cooling of large molecules is highly 'efficient,' as an exponential reduction in the number of occupied states occurs at the temperature drops. In particular, the temperature of a few Kelvin is a critical temperature. In Figure 4.1.2, $T = 4$ K is the first point at which all molecules are in the ground vibrational state, and with the total number of occupied rotational states drops below 10^2. The next critical temperature, given by $T = 2B/k_B \approx 100$ mK, is the point at which all molecules are in the lowest energy rotational state. This temperature regime, which is possible to achieve using standard buffer-gas techniques, represents a largely unexplored set of scientific possibilities.

.

4.1.2 Applications to quantum simulation and computing

Substantial progress has recently been made using molecules for quantum simulation. Recent work on ultracold KRb molecules in an optical lattice has demonstrated simulation of a spin system using dipole-dipole couplings[102]. Recently, work on polyatomic molecules, including CH_3F and related molecules by Zeppenfeld [103],

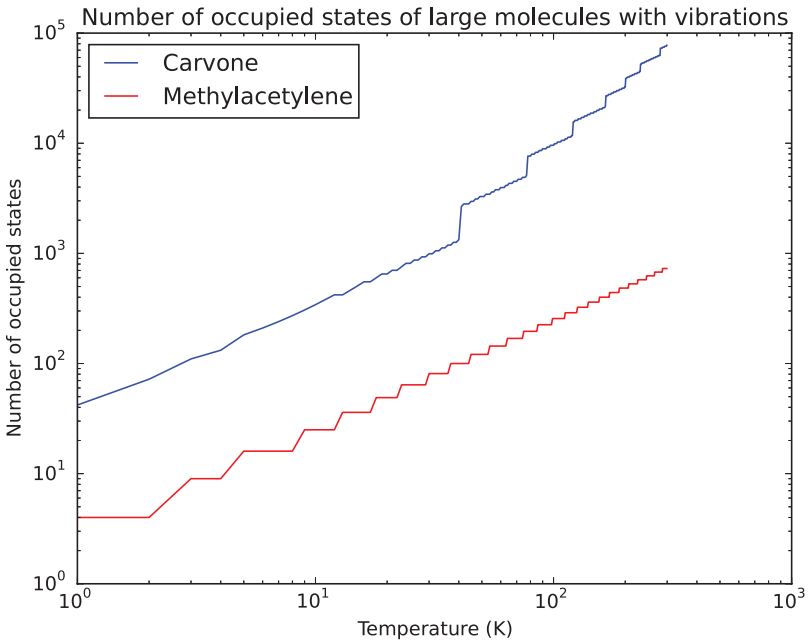

Figure 4.1.2: The number of occupied rovibrational states of methylacetylene and carvone as a function of temperature.

have achieved greater than 10^4 polyatomic molecules at $T \sim 1$mK. Large molecules offer several potential advantages over atoms, atom-like, and even diatomic molecular systems. Large molecule can be very polar. Benzonitrile, a common small organic molecule used in our lab, has a dipole moment of $\mu \approx 4.5$ D, which 150% of that of CaF. As the dipole moment is $e \times r$, a large molecule could in principle be constructed to separate multiple units of charge over more than standard bond length. Additionally, large molecules can be chosen with access to internal spin degrees of freedom. For example, any molecule containing a nitrogen has access to the $S = 1$ nuclear spin of the nitrogen-14 nucleus. Typical nuclear spin-rotation couplings are on the order of $c_N \sim 10$ kHz. For an $S = 1$ nucleus, electric quadrupole splittings, which can be on the order of GHz, will also be present. These couplings could be used to greatly diversify the set of model Hamiltonians accessible in a large molecule

quantum simulation experiment.

Additionally, large molecules could be used as a platform for quantum information and computing. Qubits could be stored in rotational states of the molecule, as discussed in Chapter 1, as well nuclear states of a large molecule. The fundamental challenge in quantum computing is to achieve a large Rabi frequency Ω for driving a qubit, while at the same time maintaining a long coherence time τ. Thus a figure of merit for potential quantum information systems could be the parameter $F = \Omega/\tau$. For example, a nitrogen-vacancy defect in diamond will have $\Omega \sim 10^7$ Hz and $\tau \sim 10^6$ Hz with $F \sim 10$.[104] The rotational state of a large molecule can have an extremely long spontaneous lifetime and couples weakly to external fields. Consider methylacetylene as a conservative case. The spontaneously lifetime of its first rotational excited state is

$$1/\tau = \frac{16\pi^3\nu^3}{3\epsilon_0 hc^3}|\mu|^2 = 4 \times 10^{-8}\ Hz \tag{4.1.4}$$

where we have used $\mu = 0.74$ D. This is extremely long compared to achievable Rabi frequencies, which are on the order of $\Omega \sim 1$ MHz. However, technical limitations such as electric field noise in an electric trap for molecular qubits could limit coherence times to $\tau \sim 1$ second, leading to $F \sim 10^6$, which is still many orders of magnitude largers than commonly used solid state systems.

In large molecules, however, we have access to nuclear spins of the molecule with nuclear-spin rotation coupling as discussed above. These nuclear states would have exceptionally long and robust coherence times for isolated, gas-phase large molecules. The robustness of coherence of nuclear states has allowed work such as NMR quantum computing in a liquid phase ensemble of large organic molecules[105, 106], and the same physics underlies hyperpolarized NMR experiments, as well as and proposals for nuclear atomic clocks[107]. While the effective Rabi frequency may be reduced to

$\Omega \sim c_N \sim 10$ kHz, this could, in principle, allow achieving $F \sim 10^{12}$. Quantum logic gates and algorithms could then be performed similar to NMR quantum computing using the nuclear-nuclear couplings of the various nuclear spins in the molecule, which have similar strengths to the spin-rotation coupling.

4.1.3 Chemistry with large molecules in a single quantum state.

In addition to the physics of manipulating single large molecules, or isolated systems of large molecules, we'd like to study large molecules as they interact strongly enough and at ranges short enough to break chemical bonds. Access to cold, large molecules, opens up the possibility of the quantum state specific chemistry of molecules. Low temperature reactions have been studied with the CRESU technique [108] and crossed beam techniques[109] for many years. However, there is new interest in studying chemical reactions at temperatures low enough that the deBroglie wavelength of the reactants approaches the characteristic interaction length scale for the reaction, where phenomena such as tunneling through reaction barriers begins to dominate the rate of a reaction. Recent progress with merged beams [110], Stark[111, 112], and magnetic deceleration [113] has allowed the study of interactions and reactions of large molecules prepared in well controlled quantum states.

For large molecules, the existence of internal degrees of freedom at modest temperatures suggest that state-specific chemistry with large molecules is feasible even at warm temperatures. Conformers, which are isomers which can be interconverted exclusively by rotations about single bonds, have typical energy spacings of $\Delta E \sim 100 - 500$ Kelvin. At room temperature, many different conformational states are occupied. However, even when conformer populations are evenly distributed, chemistry is often thought to be dictated by a single conformer. Additionally, the folding

of proteins and binding of ligands to biological receptors can be dictated by the properties of a single conformational state of a molecule[114, 115]. The ability to prepare populations in a pure conformational state could dramatically increase reaction rates and probe the understanding of the biological function of molecules.

4.2 Spectroscopy and Analytical Chemistry

Perhaps the most ubiquitous use of cold molecules is in the fields of spectroscopy and analytical chemistry. One of most powerful ways of studying the chemistry of molecules is not just to study their interactions, but study their internal properties, which is accomplished through spectroscopy. The specific quantum properties of the electronic structure, vibrational and rotation degrees of freedom, and couplings within a molecule can all be determined by spectroscopic analysis. This internal structure plays a critical role in the behavior of the bulk properties as well as reactivity.

4.2.1 Mixture analysis

A promising application of microwave spectroscopy of cold, large molecules is in the field of mixture analysis. Determining the chemical composition of a mixture is the fundamental task of analytical chemistry. The two key figures of merit of mixture analysis are sensitivity and specificity. Methods such as cavity enhanced ringdown spectroscopy and frequency comb ringdown spectroscopy[116, 117] can detect trace amounts of gas-phase molecules. Systems based on ionization such as mass spectrometry or resonant ionization (e.g. REMPI) [118]can in principle achieve single molecule sensitivity. However, methods (or ideally a single method) which can achieve the specificity to independently detect species in mixtures that contain ≥ 10 molecules

remain a major outstanding problem in the field of analytical chemistry. The key to a highly specific spectroscopic method is the production of a small number of narrow spectroscopic features for a single chemical species in a mixture.

Numerous methods are available to perform mixture analysis. Spectroscopic methods such as x-ray diffraction (XRD) and x-ray fluorescence (XRF)[119] are commonly used to identify mixtures of chemical species in the solid state. In the liquid phase, the work-horse of specific mixture analysis is Nuclear Magnetic Resonance (NMR) spectroscopy. Non-spectroscopic methods such as gas chromatography combined with mass spectrometry (GC-MS) are also used to detect $\geq$ 10 compounds in a liquid phase[120]. In practice, liquid phase mixture analysis accomplished with a combination of these techniques. A plethora of other liquid phase spectroscopic techniques exist, but many of theses have relatively poor specificity. Thus, many improvements in mixture analysis could come from a single, highly specific spectroscopic method using a gas-phase environment. In following sections, I will describe how our instrument, a CP-FTMW[121] spectrometer in a buffer-gas cell is a promising method to perform mixture analysis. To date, we have used our spectrometer to analyze liquid mixtures of up to approximately 10 chemical species. An example of a spectrum of a complex mixture which we have taken with our instrument is shown in Figure 4.2.1 . In addition to identifying mixtures, our instrument can be used to study the cooling and spectroscopy of molecules in the buffer-gas cell. Half of the identified species in the mixture whose spectrum shown in Figure 4.2.1 arise from different conformers of the same chemical species. In the next chapter of this thesis, I will discuss our study of the cooling of these conformers in the buffer-gas cell.

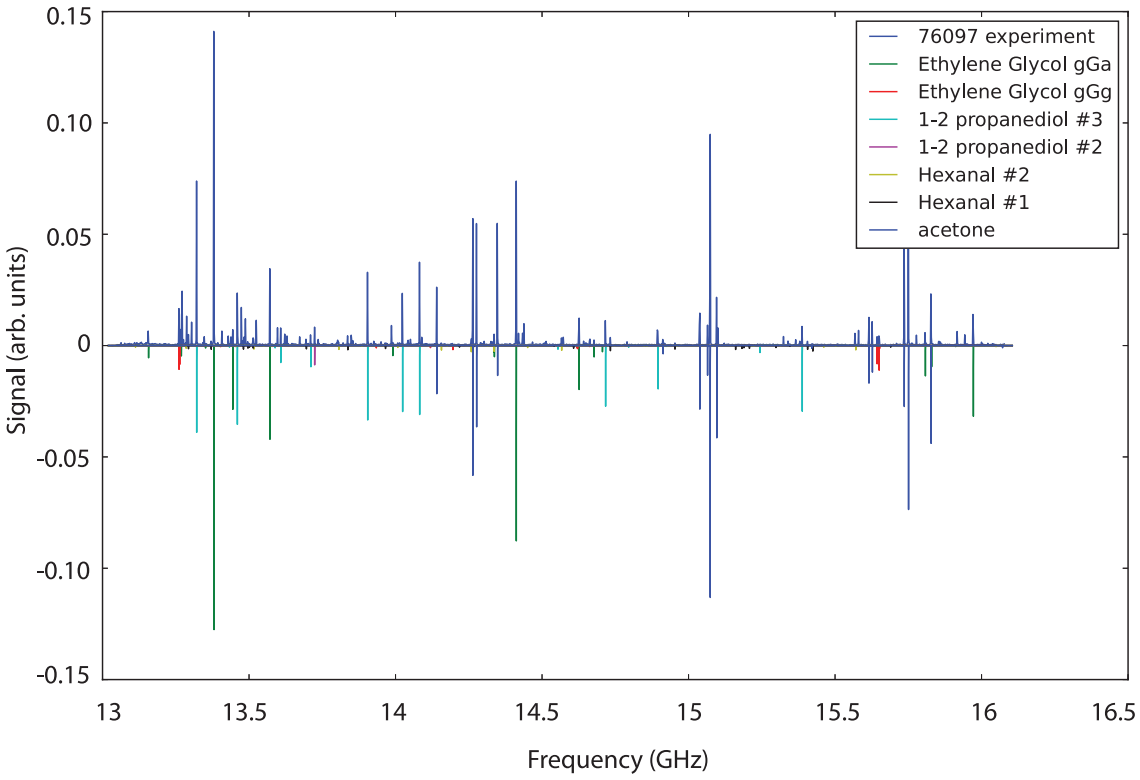

Figure 4.2.1: Spectrum of a liquid mixture of ethylene glycol, 1,2-propanediol, 1-hexanal, and acetone taken using our buffer-gas cell CP-FTMW spectrometer. The experimentally observed spectrum is plotted above the zero of the y-axis, and the theoretically identified lines are plotted below the zero of the y-axis. Different conformers of the same chemical make up half of the species identified in this mixture.

4.2.2 Microwave Spectroscopy

The physical structure of a molecule is critical to chemistry and biology. This structure is accessible using spectroscopy of rotational transitions in molecules. Microwave spectroscopy, typically performed in the gas phase, has seen decades of results and has helped to determine the structure of a very broad class of molecules, including the detection of isotopomers, conformers, enantiomers and clusters of molecules [99, 122, 123]. Microwave spectroscopy functions by finding rotational transitions in a molecule. As discussed above in section 4.1, The rotational Hamiltonian for a polar molecule is represented as a rigid, asymmetric top

$$\hat{H} = \frac{P_x^2}{2I_x} + \frac{P_y^2}{2I_y} + \frac{P_z^2}{2I_z} \tag{4.2.1}$$

This Hamiltonian can be written in terms of the rotational constants $A = \frac{\hbar^2}{2I_A}$, $B = \frac{\hbar^2}{2I_B}$ and $C = \frac{\hbar^2}{2I_C}$ as

$$\frac{\hat{H}}{\hbar^2} = AP_x^2 + BP_y^2 + CP_z^2 \tag{4.2.2}$$

and has solutions $|J, K_a, K_c\rangle$, where J is the total rotational angular momentum quantum number, K_a and K_c are the projections of the total angular momentum vector along z-axis in the case that either the molecule frame a or c is the z-axis in the limit that molecule is deformed to make a symmetric top. For a typical small organic molecule, A, B, and C are in the few GHz range. Although the selection rules are quite complicated for an asymmetric top molecule, in general an increase in either projection quantum number K_a or K_c, or in the total angular momentum J also changes the parity of the rotational wavefunction. This means that transitions between differing asymmetric top states are accessible by electric dipole microwave frequency transitions. Because the lifetime of a rotational state of a large molecule

is so long, microwave spectroscopy experiments rely on fully coherent manipulations. A typical microwave spectroscopy experiment polarizes all molecules in a microwave field emitted by a driving microwave horn with a $\pi/2$ pulse, placing the molecules in a superposition state which then radiates coherently. This radiated signal is called Free Induction Decay (FID) and is then observed via a second receiver horn. The free induction decay signal is Fourier-Transformed to determine the resonant frequency of the radiating transition. An example of a typical FID signal is shown in Figure 4.2.1.

Various microwave spectroscopy techniques exist including high precision cavity spectrometers[32], and the modern chirped-pulse Fourier transform microwave (CP-FTMW) spectrometer[121]. While a cavity based spectrometer can excel at detecting weak signals, in our work with mixture analysis, we use a CP-FTMW apparatus to harness its ability to efficiently take spectra over a broad range of frequencies.

Microwave spectroscopy benefits from the high quality and robustness of microwave hardware. A simple and relatively inexpensive system can easily deliver narrow-band power at any desired frequency by typing a command on a computer. Microwave hardware never fails unless you do something wrong and never drifts in frequency (at a level comparably to the linewidth of a microwave transition in the buffer-gas cell). The ability to produce the data described in the following sections of this thesis in only 1 year is directly attributable to these features of the microwave hardware. I wish to note that the remaining credit for the progress in this and following sections goes to Dr. David Patterson.

4.2.3 Cold molecules for spectroscopy

In order to access information about the internal structures of a molecule, single quantum states need to be interrogated. Practically, this means that the population of a

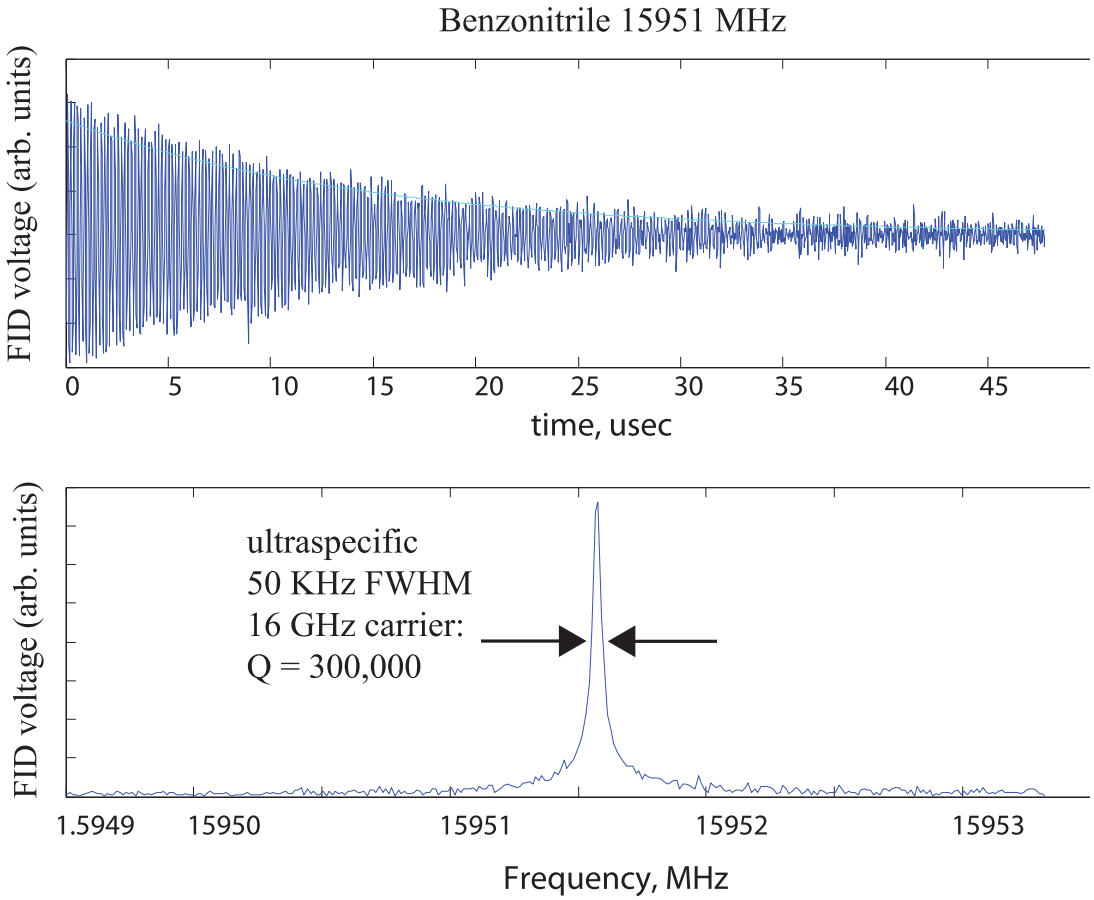

Figure 4.2.2: Typical free induction decay (FID) signal in a microwave spectroscopy experiment. The observed transition is the $|5,0,5\rangle \rightarrow |6,0,6\rangle$ transition in Benzonitrile. In this case, the experiment was performed in a $T = 6$ Kelvin buffer-gas cell, where the line width is 50 kHz, determined by the collision rate with the buffer-gas. In jet-cooled beam microwave spectroscopy experiments, this linewidth is often set by Doppler broadening and depends on the particular detection geometry used.

spectroscopic sample must be limited to an experimentally and theoretically tractable number of quantum states. Should the population exist in an intractable number of states, definitive identification becomes impossible. Thus, while some applications can be successful without this, a precise and accurate measurement of molecular properties requires definitive identification. In order achieve this requirement, cold temperatures of ($T \lesssim \Delta E/k_B$), where ΔE is the energy spacing between levels, are necessary. Room temperature can be a feasible energy scale to work at for a very small set of very small molecules, but for the vast majority of typical 'small molecules,' cryogenic temperatures are required. For the vibrational degree of freedom, this requires $T \lesssim 100$ Kelvin, for the rotational degree of freedom, this typically requires $T \lesssim 1$ Kelvin. Isolation of weaker degrees of freedom can require ultracold temperatures, but these couplings are typically spin related and the corresponding number of states are limited by magnitudes of the spin involved. An example of microwave rotational spectroscopy of acetone at both room temperature and $T \sim 1$ K is shown in Figure 4.2.2 and illustrates this requirement.

The most common technique for the production of cold molecules for spectroscopy is the pulsed supersonic jet[31]. This method involves cooling during a rapid isentropic and adiabatic expansion from a high pressure reservoir into a very low pressure region. For an ideal gas and the absence of shock waves, viscous forces, heat sources such as chemical reactions,

$$\frac{T}{T_0} = \left(\frac{P}{P_0}\right)^{(\gamma-1)/\gamma} = \frac{1}{1+\frac{1}{2}(\gamma-1)M^2}, \tag{4.2.3}$$

where T and P are the final temperature and pressure, T_0 and P_0 are the initial temperature and pressure, $\gamma = c_p/c_v$ is the ratio of the constant pressure heat capacity to the constant volume heat capacity, and M is the mach number of the flow. Thus, for

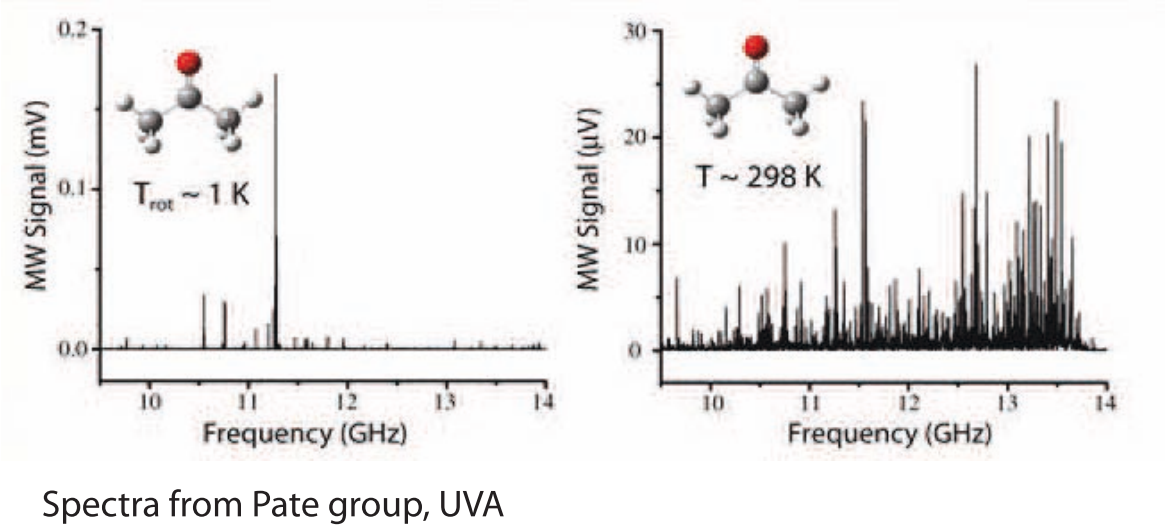

Figure 4.2.3: Microwave spectrum of acetone taken at a rotational temperature of $T \sim 1$ Kelvin, and at the room temperature, $T = 298$ Kelvin, showing the large improvement in spectroscopic analysis when using cold molecules for spectroscopy. This data is courtesy of Brooks Pate, University of Virginia.

great enough difference in pressure between the reservoir and the low pressure region, and correspondingly the higher the mach number, the colder the sample becomes until collisions finally cease and the temperature is frozen. Mach numbers as high as $M = 250$ ($T = 0.015$) Kelvin can be produced given adequate maintenance of the low pressure region. The largest factor increasing the mach number is the reduction in the speed of sound via reduction of the density of the flow. However, the flow speed does increase due to boosting - more collisions from the high pressure rear of the flow than from the lower pressure front of the flow. This results in molecular velocities as high at $v = 1000$ m/s. At this speed, molecules in a supersonic expansion typically only experience collisions for a distance of 1 cm, which occurs in a time of $t = 10^{-5}$ seconds. During this time, only a handful (10-100) of collisions occur. This short duration and rapidly changing density of the supersonic expansion environment make detailed study of this cooling challenging. While final translational temperatures

as low the above quoted $T = 15$ mK have been achieved, typical set-ups achieve rotational temperatures of $T_{\mathrm{R}} < 1$ K . This is because it is technically challenging to maintain a very high vacuum in the low pressure region while inputting a large gas load. The common solution to this is to use a pulsed source of molecules as opposed to a continuous source. Additionally, thermalization of other internal degrees of freedom proceeds more slowly, for example vibrational temperatures are routinely $T_{\mathrm{V}} \sim 1-10$ K and conformational temperatures tend to be $T_C \sim 100$ Kelvin [124].

As will be shown in the next chapter of this thesis, the collisional environment of a buffer-gas cell allows for technically easier and more precise studies of cooling in large molecules. Additionally, buffer-gas beams offer an ideal source for precision spectroscopic measurement. The molecular flux of a buffer-gas beam can be more than an order of magnitude higher than a pulsed supersonic jet. The slower forward velocity of the beam can add additional coherence time to the measurement as well, which linearly increases the sensitivity of the measurement. The electron electric dipole moment (EDM) measurement is a good example of a precision spectroscopic measurement made with a buffer-gas beam source which attains higher sensitivity than comparable supersonic beam-based measurements[19].

A number of additional methods for producing cold molecules for spectroscopy in the solid state have been developed. One of the most successful of these methods is matrix isolation spectroscopy. In this method, a dilute gaseous mixture of a species mixed with a noble gas carrier is deposited onto an optical window held at cryogenic temperatures. In the frozen solution, the embedded molecules are relatively weakly coupled to the frozen matrix environment. This coupling is strong enough to cool the internal degrees of freedom on the embedded molecules to the thermodynamic temperature of the ice, but weak enough that spectroscopic lines of individual quantum

states can often be fully resolved. This method has produced a rich set of studies of chemical reactions[125] and the cooling of internal degrees of freedom[126]. Additional methods include interesting techniques such as spectroscopy inside droplets of superfluid helium[127].

Chapter 5

Conformational Relaxation in a Buffer-Gas Cell

5.1 Conformers in chemistry and biology

The structure of organic molecules is critical to molecular function in biology and chemistry. In particular, understanding the properties of conformers, which are rotational isomers, allows us to understand diverse phenomena such as the folding of proteins[128, 115, 129, 114], behavior of DNA[115, 130], metabolism of sugar[131, 132] , and reactions of organic molecules with trapped ions[133]. Key open chemical questions regarding conformers include the identification and energy of conformers, structure, interconversion barrier heights and shapes, and chemical relevance[115, 30]. Conformers may be observed using a diverse set of spectroscopic methods and environments. For example, molecular beam microwave spectroscopy can measure structure[32], cryogenic matrix isolation spectroscopy can measure dynamics in a solid state environment [134], and ultrafast spectroscopy can measure both structure

and reaction dynamics [135]. Each method provides a window into certain conformational properties and could be compared to quantum-chemistry theory calculations. For example, the study of the conformers of glycine has seen a rich interplay between quantum-chemistry theory and spectroscopy [136, 134, 137, 138, 139].

Much of our understanding of gas-phase conformers comes from jet cooled molecular beam spectroscopy and cryogenic matrix isolation spectroscopy experiments. The low internal and beam-frame temperature of molecules in the jet allows for precision spectroscopy, which can help determine structure of conformers[31]. Despite the low internal temperatures achieved, a thermally distributed gas-phase conformational population is rarely observed in these methods. The cooling of the conformational degree of freedom is governed by conformational relaxation, which is the conversion of a high energy conformer into a lower energy conformer. It can be induced by gas-phase collisions or couplings in a solid state environment and is an important phenomenom used in the study of conformational interconversion barriers. In jet cooled molecular beam spectroscopy, conclusions about the interconversion barriers separating conformers can be obtained by observing the relative population of conformers after relaxation, or by spectroscopy of embedded gas phase samples in a cryogenic ice matrix[140]. However, direct, continous observation of collision-induced gas-phase conformational relaxation has not previously been achieved. The primary limitation preventing continuous collisional measurements in jet cooled molecular beams is the short duration and rapidly changing density and energy of the supersonic expansion. Other indirect methods to study conformational relaxation and potential energy surfaces include [141, 142, 143].

5.2 Microwave spectroscopy of conformers in a buffer-gas cell

We report the direct observation of conformational relaxation using microwave spectroscopy paired with buffer-gas cooling. Owing to the controlled and well understood collisional environment in the buffer-gas, the conformation-changing scattering cross-section can be measured, which provides a sensitive and quantitative probe of the conformational potential surface of the molecule. Collision frequency can be controlled via the buffer-gas density in the cell, which is typically low enough to allow for high precision, state-specific spectroscopy with resolution comparable to that achieved in jet cooled beams.

Fourier Transform Microwave (FTMW) rotational spectroscopy is an efficient tool to study the dynamics of conformational relaxation in a cryogenic environment, and reveals the structural information of a molecule because transition frequencies are determined by the moments of inertia of the molecule[99]. FTMW spectroscopy has been used to detect conformers, isotopomers, and clusters of molecules in the gas-phase. Due its continuous nature microwave spectroscopy in a buffer-gas environment can be up to two orders of magnitude more sensitive than in pulsed supersonic jet experiments[90] and has been used to perform mixture analysis, as well as measurement of the enantiomeric composition of samples[123]. Additionally, buffer-gas cooling has been shown to cool a diverse set of organic molecules to the few Kelvin temperature range[33, 144, 90]. The density of buffer-gas in a buffer-gas cell is constant, low, and can be accurately measured. This allows for precise measurements of atom-molecule inelastic cross-sections[145, 35].

We chose the chiral molecule 1,2-propanediol as the subject for our study. 1,2-

propanediol is spectroscopically well understood and has been previously used in both pulsed-jet and buffer-gas cooling microwave spectroscopy experiments[124, 90]. Conformers of 1,2-propanediol and similar molecules have been spectroscopically identified in pulsed jet experiments and *ab-initio* calculations on the conformational potential surface have guided the spectroscopic analysis of these molecules[146, 100, 147]. In our current study, we observe seven conformers of 1,2-propanediol, conformers #1-#7, which are described in detail in [124].

5.3 Apparatus and experiment

The experimental apparatus used for these measurements is a Chirped-Pulsed Fourier Transform Microwave (CP-FTMW) spectrometer that uses a cryogenic buffer-gas cooling cell (see Figure 1). Previous generations of the apparatus, similar to the current, are described in detail elsewhere[90, 123]. Briefly, an 18 cm sided cubic buffer-gas cell is held at 6 Kelvin by a pulse tube cryocooler. On one side of the buffer-gas cell is a 1.5 cm diameter inlet hole through which molecules are introduced. A pulsed valve at $T = 320$ Kelvin is backed by gaseous 1,2-propanediol is located 1.5 cm from the inlet of the cell. Warm molecules from this pulsed valve enter the cell and then experience 10-100 collions to cool translationally and rotationally, and are then lost via diffusion to the cell wall after undergoing approximately one thousand collisions in 10 ms. The input flow of molecules can be operated in either a pulsed mode or a continuous mode where the valve is held open.

Helium buffer-gas is introduced into the cell through a fill line placed near the molecule entrance aperture. The typical helium density in the cell is on the order of $n_{\mathrm{He}} \sim 10^{14}$ cm^{-3} and the typical 1,2-propanediol density in the cell is $n_{\mathrm{prop}} \sim 10^{9}$ cm^{-3} . The rotational temperature of the buffer-gas is measured to be $T = 6$ K in

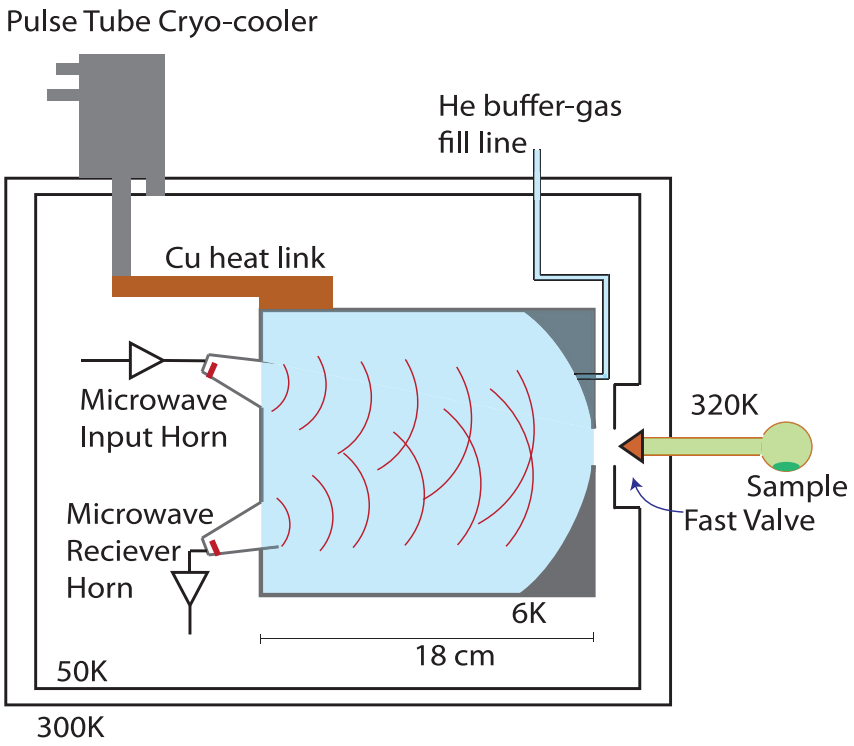

Figure 5.3.1: Experimental apparatus (not to scale). Molecules are loaded into the cold cell via injection from a warm ($T = 320$ Kelvin) pulsed valve and through a hole in a microwave mirror, where they thermalize and eventually diffuse to the cold cell walls and freeze. The resulting translationally and rotationally cold gas is polarized by a brief, strong microwave pulse emitted from the microwave input horn. The resulting free induction decay is collected by a microwave receiver horn coupled to the same microwave mode. The signal from the reciever horn is amplified, mixed down to RF frequencies, and digitized.

all cases and the translational temperature is assumed the same. The mean elastic collision time between a 1,2-propanediol molecule and a helium atom is approximately 10 μs and the diffusion time of molecules to the walls of the cell is $\tau \sim 10$ ms. On the side of the cell opposite the aperture are two microwave horns coupled to the molecules and each other via a spherical microwave mirror located on the aperture side. The microwave field mode defined by this geometry occupies the majority of the cell and has good overlap with the zeroth order diffusion mode for molecules in the cell. The input horn is driven by a microwave chirp with a bandwidth of 100 MHz and a central frequency that can be varied from 12-18 GHz. This drive field provides a $\pi/2$ pulse to initiate the free induction decay (FID) signal, which is picked up by the receiver horn. The signal from the receiver horn is fed to a switch-protected low noise amplifier. The reciever signal is mixed back down using the local oscillator, digitized, and averaged by a low dead-time data acquisition card.

The experimental timing sequence is shown in Figure 2. Microwave spectra of 1,2-propanediol are recorded during varying time windows after the opening of the pulsed valve, delayed by an interval ΔT ranging from $\Delta T = 10$ ms to $\Delta T = 34$ ms. After the packet of 1,2-propanediol enters the cell, 200 microwave drive chirps of 100 MHz in width polarize the molecules in the microwave mode, and after chirp, a 20 μs long FID trace is collected via the receiver horn. The FID signal is Fourier transformed to produce the spectrum. Measurements were performed at two different buffer-gas flow rates into the cell $f = 7.5 \times 10^{17}$ and $f = 1.25 \times 10^{18}$ molecules/sec (3 and 5 sccm) respectively. Relative changes in the density of the helium buffer-gas can be measured using the collisionally limited ringdown time of the FID signal[90]. The absolute helium density can be determined by knowledge of the molecular conductance of cell aperture and by the absolute flow into the cell using the equation $n_{\mathrm{He}} = \frac{4f}{A\bar{v}_{He}}$,

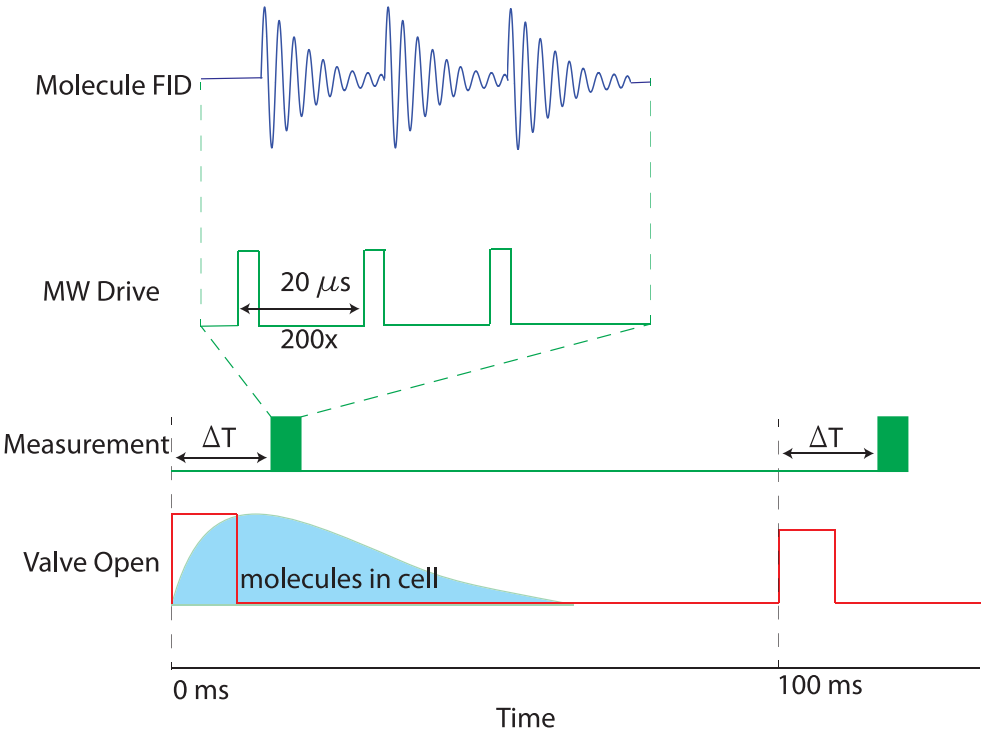

Figure 5.3.2: The experimental timing protocol. The pulsed valve is opened for 10 ms, which introdues the packet of molecules into the cell. Molecules diffusion through the cell for approximately 10-20 ms, as shown by the blue shaded region. A time ΔT after the valve is triggered, the measurement sequence begins. The measurement is composed of 200 polarizing chirped microwave pulses with repetition rate is 50 kHz, as set by the mean collision time of 10 μs. The FID signal is recorded in the time following the polarizing pulse. All FID signals for a given ΔT are averaged together. Varying ΔT allows construction of a "movie" of the conformer populations.

where f is the buffer-gas flow rate into the cell, A is the open area of the cell aperture, and $\bar{v}_{\mathrm{He}} = 158$ m/s is the mean thermal velocity of the helium at the temperature of the cell, $T = 6$ Kelvin. For our cell, the density per sccm of buffer-gas flow inside is calculated to be $n_{\mathrm{He}} \approx 3.6(1.8) \times 10^{13}$ sccm^{-1}cm^{-3}. The absolute flow rate of our flow controller was calibrated using a volume standard. Using the ringdown time of the FID signal then yields a measured state and conformer specific rotation changing collision cross-section σ_R, which vary by approximately 25%. Across conformers, these cross-section are measured have an average value $\bar{\sigma}_R = 5.8(2.9) \times 10^{-14}$ cm^2, where the quoted error in the mean is derived from uncertainty in the absolute buffer-gas density in the cell. Additional data was taken with the valve held open. In this mode, we can take higher sensitivity spectra but without time dynamics to be recorded due to a much higher measurement duty cycle.

In the pulsed mode of operation, as the measurement time delay ΔT increases, we observe conformer signals decaying at various rates faster and slower than the diffusion time. This decay is the result of a combination of two effects, conformational relaxation and diffusion to the cell wall. For some conformers, the primary source of this decay is diffusion. However for other conformers such as #5 and #6, the observed loss is much quicker. We interpret this as due to conformational relaxation. One set of typical spectra is shown in Figure 3. To understand the effect of diffusion alone, we study the time behavior of the methylacetylene (C_3H_4), a species with no internal conformers. Data was taken at 11 evenly spaced time intervals ΔT, shown in Figure 4. We find that for methylacetylene, the in-cell dynamics are well modeled using a simple diffusion model. The molecules first diffuse into the cell center as they enter through the aperture, and then continue to diffuse to the cell wall where they freeze.

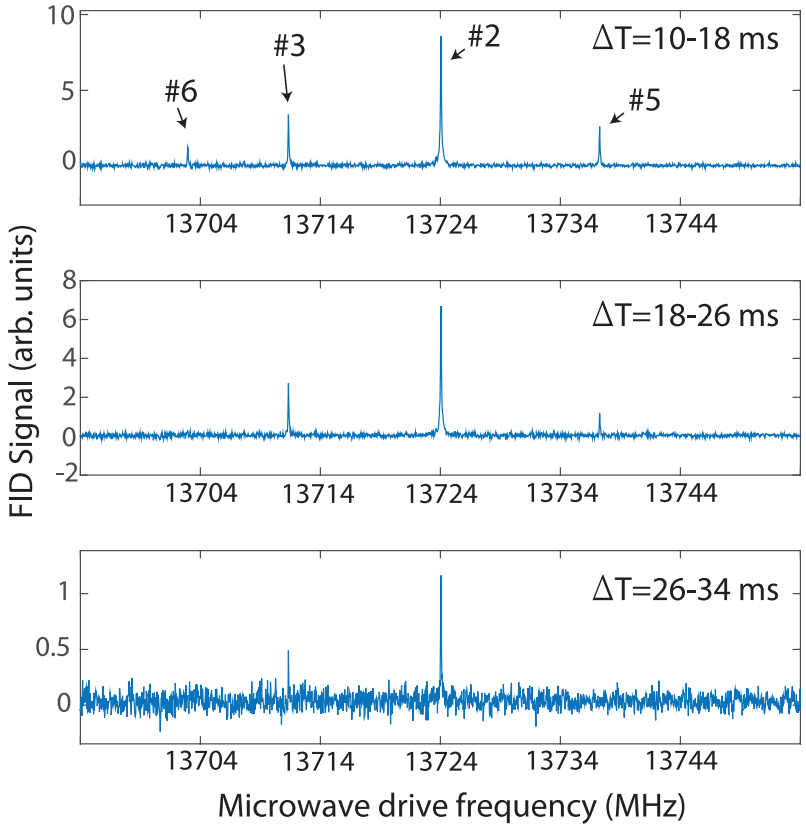

Figure 5.3.3: Spectra of 1,2-propanediol in the region from 13694 MHz to 13754 MHz taken at different time intervals ΔT after the pulsed valve opens. The molecular signal decays over time due to diffusion to the cell walls, but is plotted on axes scaled to magnitude of the signal. Conformational relaxation is visible as the changing ratio of peak heights over time. Here, conformer #6 is the fastest to relax, followed by conformer #5. Here, conformer #2 appears to decay very slowly, if at all, to the ground state (conformer 3).

5.4 Modeling the dynamics of molecules in a pulse loaded buffer-gas cell

Our diffusion model assumes the input of a Gaussian-shaped pulse of N_{T} total molecules with a temporal width w. This pulse travels from the valve to the cell in time t_0, where it then lost at a rate α via 'one-body' process. In the case of no internal dynamics (diffusion only), $\alpha = 1/\tau$ where τ is the diffusion time of the zeroth order diffusion mode in the cell. After the molecules have entered the cell, the number of molecules $N(t)$ in the microwave mode at any time is described by the differential equation

$$\frac{dN(t)}{dt} = N_{\mathrm{T}} R(t) - \alpha N(t), \tag{5.4.1}$$

where $R(t)$ is the loading rate of molecules into the cell and reflects the valve dyanmics, where, again, we model the loading pulse as

$$R(t) = \frac{1}{\sqrt{2\pi}w} e^{-\frac{(t-t_0)^2}{2w^2}}, \tag{5.4.2}$$

with $\int_{-\infty}^{\infty} R(t)dt = 1$. The solution to equation 1 is the function

$$N(t) = \frac{1}{2} N_{\mathrm{T}} \cdot e^{\frac{1}{2}\alpha(-2(t-t_0)+\alpha w^2)} \cdot \left(\mathrm{erf}\left(\frac{t_0 + \alpha w^2}{\sqrt{2}w} \right) - \mathrm{erf}\left(\frac{-t + t_0 + \alpha w^2}{\sqrt{2}w} \right) \right). \tag{5.4.3}$$

This equation fits the methylacetylene data very well, as shown in Figure 4, with typical values $\alpha \sim 10$ ms^{-1}, $w \approx 6$ ms, and $t_0 \approx 10$ ms, depending on conditions. The parameters w and t_0 are characteristics of the pulsed valve and hence are assumed to be the same for all chemical species, including 1,2-propanediol.

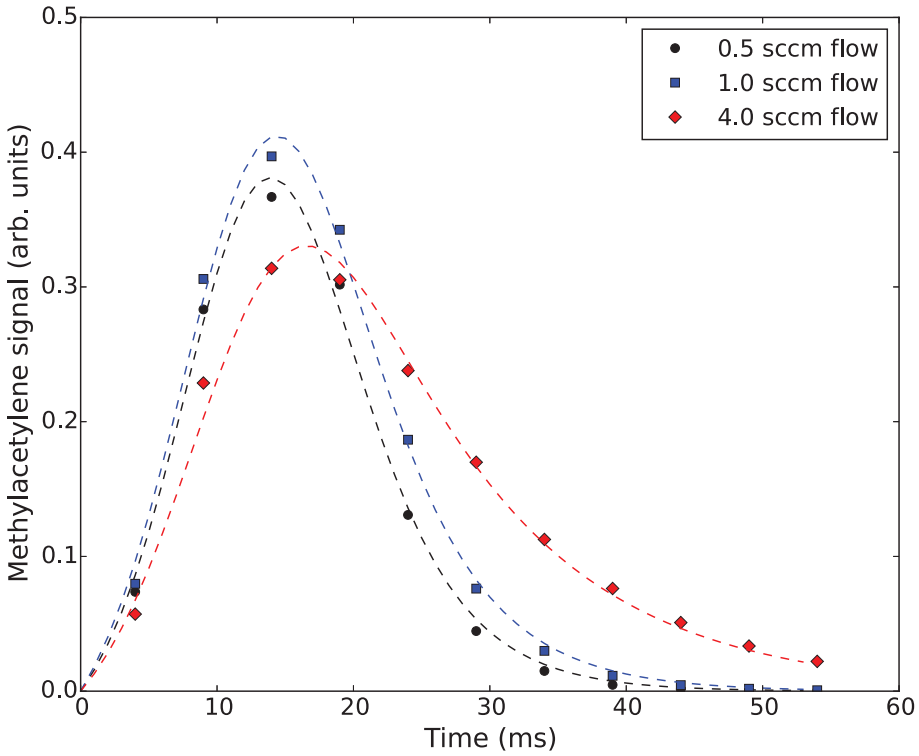

Figure 5.4.1: Time dynamics of a pulse of methylacetylene in the cell at three different buffer-gas flow rates. The dynamics are well fit by a simple diffusion model, where the microwave mode in the cell is loaded with a Gaussian shaped pulse of molecules and undergoes diffusion in the zeroth order mode in cell. The fit to the model (eq. 3) in each case is denoted with a dashed line. The values w and t_0 measured for methylacetylene are used to fit the 1,2-propanediol dynamics.

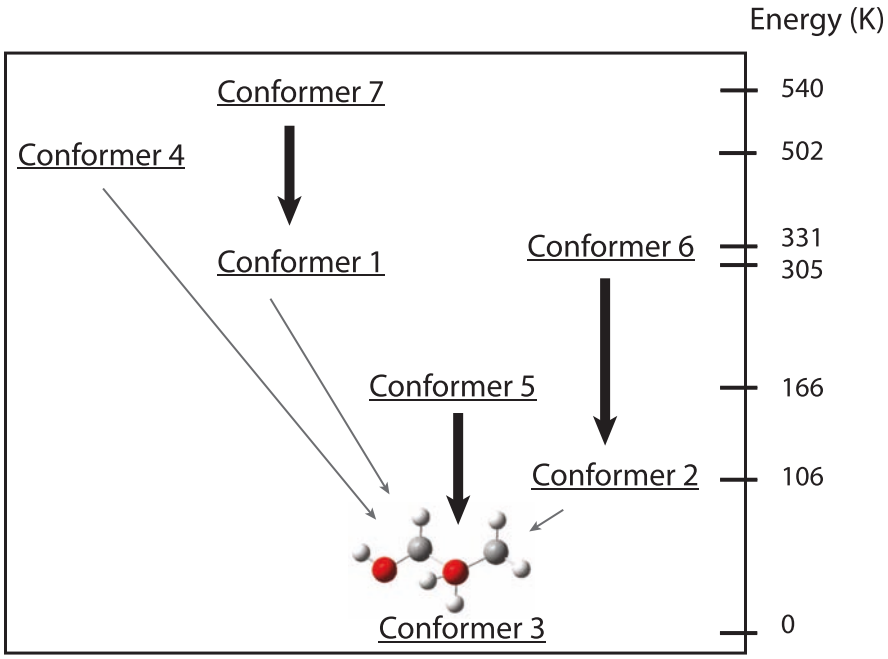

Figure 5.4.2: The observed 1,2-propanediol system with hypothesized conformational cooling pathways for 1,2-propanediol. Pathways denoted with thick black arrows involve a 110-120 degree rotation of a free OH group and are expected to have relatively large relaxation rates. Pathways denoted with thin gray arrows are weaker channels and represent relaxations involving a greater degree of structural change to the molecule, as discussed in [124].

5.5 Observation and dynamics of conformational relaxation in the buffer-gas cell

In the case of 1,2-propanediol, we model the conformers as coupled states undergoing population transfer through both conformational relaxation and diffusion to the cell walls. We model the couplings between conformers first assuming the suggested conformational pathways in Lovas et al. A schematic of this model is shown in Figure 5. In particular, the populations of the conformers obey the equation

$$\frac{d\vec{N}}{dt} = \vec{N}_{\mathrm{T}} R(t) + \mathbf{A}\vec{N}(t), \tag{5.5.1}$$

where $\vec{N}$ is a vector containg the populations $N_i(t)(i = 1, \ldots, 7)$ of the seven observed conformers, $\vec{N_{\mathrm{T}}}$ is a vector containing the total intial populations of each conformer, $R(t)$ is the same loading rate defined by equation 2, and $\mathbf{A}$ is the matrix whose elements contain to diffusion and inter-conformational population transfer rates.

$$\mathbf{A} = \begin{pmatrix} -\alpha & 0 & 0 & 0 & 0 & 0 & \alpha_{7\to1} \\ 0 & -(\alpha+\alpha_{2\to3}) & 0 & 0 & 0 & \alpha_{6\to2} & 0 \\ 0 & \alpha_{2\to3} & -\alpha & \alpha_{4\to3} & \alpha_{5\to3} & 0 & 0 \\ 0 & 0 & 0 & -(\alpha+\alpha_{4\to3}) & 0 & 0 & 0 \\ 0 & 0 & 0 & 0 & -(\alpha+\alpha_{5\to3}) & 0 & 0 \\ 0 & 0 & 0 & 0 & 0 & -\alpha & 0 \\ 0 & 0 & 0 & 0 & 0 & 0 & -\alpha \end{pmatrix}. \tag{5.5.2}$$

To measure the coupling rates $\alpha_{\mathrm{a}\to\mathrm{b}}$ between any two conformers a and b and the diffusion time α, we fit the observed conformer populations $N_{\mathrm{i}}(t)$ to a numerical

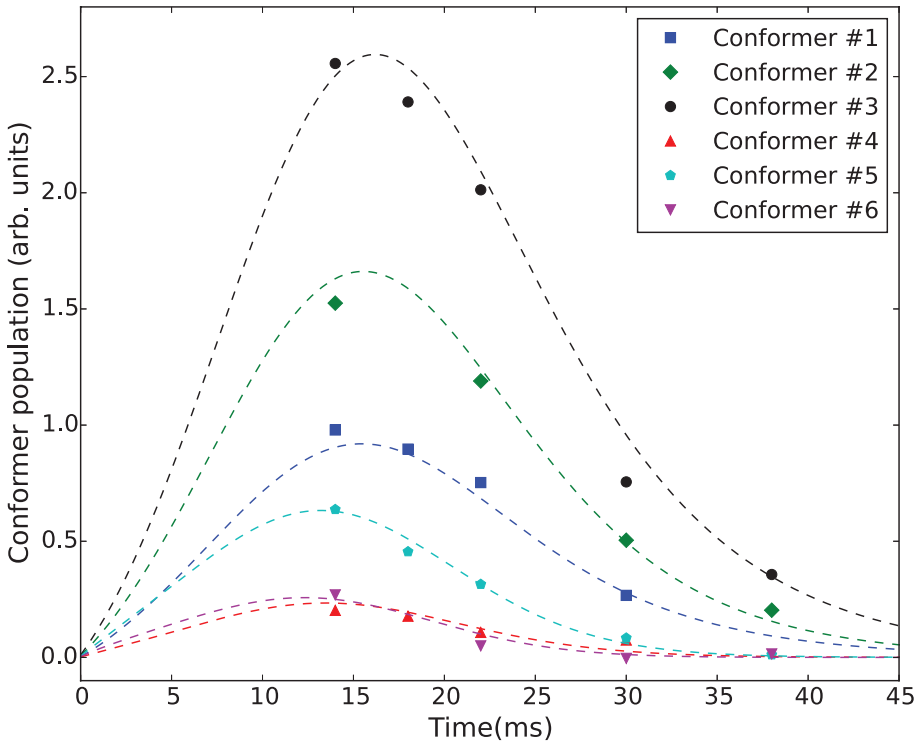

Figure 5.5.1: Dynamics of the populations of conformers #1−#6 of 1,2-propanediol in the buffer-gas cell at a helium density $n_{He} = 1.4(7) \times 10^{14}\,\mathrm{cm}^{-3}$. Each population is calculated from the observed line strength by dividing by the predicted line strength, as calculated from the PGOPHER program. The time evolution of the conformer populations is fit to a simple diffusion model with one free parameter, $\alpha_{\mathrm{a}\to\mathrm{b}}$, for each conformer. The time for a each point is set to the center of the integration window.

solution to equation 4. In this fit, the initial population of each conformer i, $N_{\mathrm{T},i}$, is assumed to be a thermal population at $T = 320$ Kelvin, which is the temperature of the pulsed valve. The conformer populations are derived from the intensity of each spectral line by dividing by the line strength as calculated using the microwave spectroscopy package PGOPHER[148] and by normalizing to an overall factor.

This data set shows clear evidence for conformational relaxation along the pathways suggested in Lovas et al., but we also observe strong relaxation from conformer

#4 to the ground state, a pathway which was hypothesized to be weak by Lovas et al.. The measured relaxation rates differ significantly from conformer to conformer, suggesting that this measurement is sensitive to the different interconversion barrier shapes. Conformers #4, #5, and #6 are measured to have large inelastic relaxation rates into the ground state of $\alpha_{4\to3} = 0.12(5) \times 10^3$ s^{-1}, $\alpha_{5\to3} = 0.15(6) \times 10^{-3}$ s^{-1}, and $\alpha_{6\to3} = 0.3(1) \times 10^3$ s^{-1} respectively, compared to the diffusion rate of $\alpha = 0.14(6) \times 10^3$ s^{-1} . Additionally, small signals from conformer #7 are seen in steady flow data. Based on the observed dynamics of conformer #1, we estimate a high rate relaxation from conformer #7 into conformer #1 of $\alpha_{7\to1} > 0.5 \times 10^3$ s^{-1}. Table 1 summarizes the inelastic relaxation rates of the conformers and their ratios with the elastic cross-sections at a buffer-gas density of $n_{\mathrm{He}} = 1.4(7) \times 10^{14}$ cm^{-3}.

Dynamics of the conformer populations can also be measured at different helium densities. The experiment was repeated at a helium density higher by a ratio of $r = 1.33(6)$. At this higher density, the relaxation rates are observed to scale linearly with the buffer-gas density. This is additional evidence that the conformational relaxation we see here is the result of collisions with the helium buffer-gas. We assign a conformational relaxation collision cross-section to each pathway using

$$\sigma_{\mathrm{a}\to\mathrm{b}} = \alpha_{\mathrm{a}\to\mathrm{b}}/n_{\mathrm{He}}\bar{v}, \tag{5.5.3}$$

where $\bar{v}$ is dominated by $\bar{v}_{He}$ to the 95% level. These values are summarized in Table 1. Also shown is the ratio of rotational relaxation to conformational relaxation collision cross-sections, $\gamma_R = \bar{\sigma_R}/\sigma_{\mathrm{a}\to\mathrm{b}}$. The value of $\bar{\sigma_R}$ is measured to be $\bar{\sigma}_R = 5.8(2.9)\times10^{-14}$ cm^2 using the FID ringdown time and measured density, and is measured to be the same for each conformer to the 25% level. The quoted error in Table 1 is combined statistical (from fitting) and systematic and is dominated by uncertainties in the

Pathway	ΔEnergy (K)	α ($\times 10^3\,\mathrm{s}^{-1}$)	σ ($\times 10^{-14}\,\mathrm{cm}^2$)	γ_R
#2−#3	106	0.01(1)	$4.7(3.0) \times 10^{-4}$	$> 10^4$
#5−#3	166	0.15(6)	$7.0(4.5) \times 10^{-3}$	$8.2(3.3) \times 10^2$
#6−#2	225	0.3(1)	$1.4(0.9) \times 10^{-2}$	$4.1(1.6) \times 10^2$
#7−#1	235	> 0.5	$> 5 \times 10^{-2}$	$< 10^2$
#4−#3	502	0.12(5)	$5.6(3.6) \times 10^{-3}$	$1.0(0.4) \times 10^3$
Diffusion	-	0.14(6)	$6.6(3.3) \times 10^{-3}$	-

Table 5.1: Rates α, collision cross-sections σ, and values of the ratio γ_R for the five measured conformational relaxation rates and the 1,2-propanediol diffusion rate as measured at the buffer-gas density of $n_{\mathrm{He}} = 1.35 \times 10^{14}\,\mathrm{cm}^{-3}$.

absolute frequency dependent gain of the detection system and the absolute buffer-gas density in the cell. Measurement of the ratio γ_R, ratios of relaxation rates for different pathways $\sigma_{\mathrm{a}\to\mathrm{b}}/\sigma_{\mathrm{c}\to\mathrm{d}}$, and diffusion rates at different helium densities are known to higher accuracy than the absolute values listed in Table 1 because they do not rely on knowledge of the absolute buffer-gas density in the cell.

In conclusion, we have directly observed conformational relaxation pathways and measured the collision induced relaxation cross-section of 5 of the excited conformers of 1,2-propanediol. Our measurements have shown partial agreement with the hypothesized relaxation pathways, and an additional strong conformational relaxation pathway in 1,2-propanediol which were not previously hypothesized. The measured cross-sections are comparable to the cross-sections measured associated with other relaxation processes of a similar energy scale[35]. The mechanism behind the conformational relaxation remains an open question. Further measurement using different isotopologues, rotational states, or at different collision energies (via buffer-gas temperature) would elucidate the mechanism behind the relaxation. This method could be applied to any thermally stable and buffer-gas cool-able molecule, which is thought encompass most small molecules. Information about cooling pathways and conformational structure (in form of the cross-section) can be learned about a wide range

of molecules.

Chapter 6

Future Directions with Large Molecules

In this chapter of my thesis, I will describe several results and future research directions on spectroscopy, cooling, and quantum mechanical control of large molecules. I will describe preliminary results on three different experiments. In the first experiment, we demonstrate key steps in the separation of chiral molecules using Moire deflectometry. In particular, we observe Moire fringes using a beam of cold benzonitrile, demonstrating a working set of Moire gratings which are sensitive to milliKelvin transverse potentials. We also describe a full scheme for the separation and potential applications. In the next experiment, we demonstrate preliminary results on an experiment to measure parity violation in chiral molecules. We achieve buffer-gas cooling of methyl-trioxorhenium, a candidate molecule for a parity violation search using microwave or IR spectroscopy. We also outline several possible measurement schemes. Finally, I will discuss spectroscopy of highly unstable molecules, and present results on successful isolation and spectroscopy of highly reactive chemical intermediates in a buffer-gas cell for tens of milliseconds. These results underscore the diversity of

spectroscopy and quantum mechanical control experiments possible using buffer-gas cooled large molecules.

6.1 Chiral Separation using Moire deflectometry

One of the most exciting future directions with large molecules is the enantiomer-specific microwave spectroscopy developed in the Patterson lab[123, 149]. This novel method for measuring the enantiomeric character of a sample, or mixture of samples, is based on capturing the geometric structure of a molecules dipole moment in the phase of a spectroscopic signal. Two enantiomers of a polar, chiral molecule will have identical values of the magnitude of their dipole moment $||\vec{\mu}||$. For any choice of coordinate system, the sign of the projection of the dipole moment vector along two axis a and b , μ_a and μ_b, will be identical between enantiomers. Along, the third axis, however, the sign of the projects μ_c will differ. Hence, the product $\mu_a\mu_b\mu_c$ changes sign between different enantiomers, which is independent of the particular choice of axes used. A schematic of this distinction between enantiomers is shown in Figure 6.1.1. Using the correct set of coherent manipulations in a molecule, this product can be mapped onto the phase of emitted radiation.

A particularly appealing classical analogy to this problem is that of identifying left hand threaded or a right hand threaded machine screw. Given a machine screw in a tapped hole, how can one tell the handedness of the thread? One simply turns the screw clockwise (x-y axes) and observes the whether the screws backs out of the tapped hole, or enters deeper (z axis). The spectroscopic analogy of this process is to make a $'$clockwise$'$ turn of the molecule by driving rotational transitions along two axes of the molecule and observe the phase of radiation emitted along the third. This method is typically accomplished by resonantly driving a c-type and a-type transition

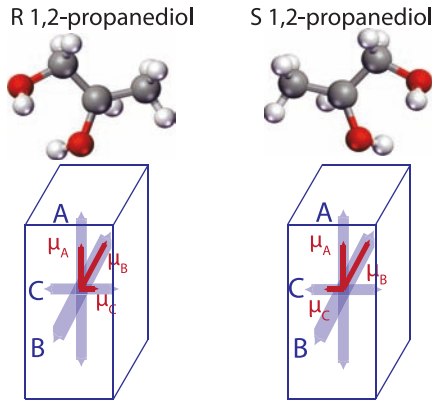

Figure 6.1.1: Two enantiomers of the molecule 1,2-propanediol. These enantiomers can be distinguished based on the relative orientation of the molecular dipole. Regardless of the choice of axes a, b, c, the product of the dipole moment projections $\mu_a\mu_b\mu_c$ changes sign between different enantiomers.

simultaneously, and recording the radiation emitted at the frequency of the b-type transition in a closed triad of states. The rotations are mapped to physical axes of the molecule through the lab frame polarization of the microwave field. Therefore each transition is driven with a mutually orthogonal linear polarization. This method, called three-wave mixing, was successfully demonstrated to measure enantiomeric excesses in samples as small as 2%. This sensitivity combines with high specificity to make this method an unprecedentedly powerful tool for chiral mixture analysis. A schematic of this method and a plot of the resulting radiation with enantiomer-specific phase is shown in Figure 6.1.2. An additional method which rotates the states by mixing using a switched DC field was used in the initial work and has applications in experiments to detect the absolute configuration of a chiral species, which will be discussed below.

Given a method which can measure the enantiomeric character of a mixture, a key process to demonstrate next would be a separation, or purification, of a such a mixture. The first separation of chiral samples was accomplish by Pasteur in 1848,

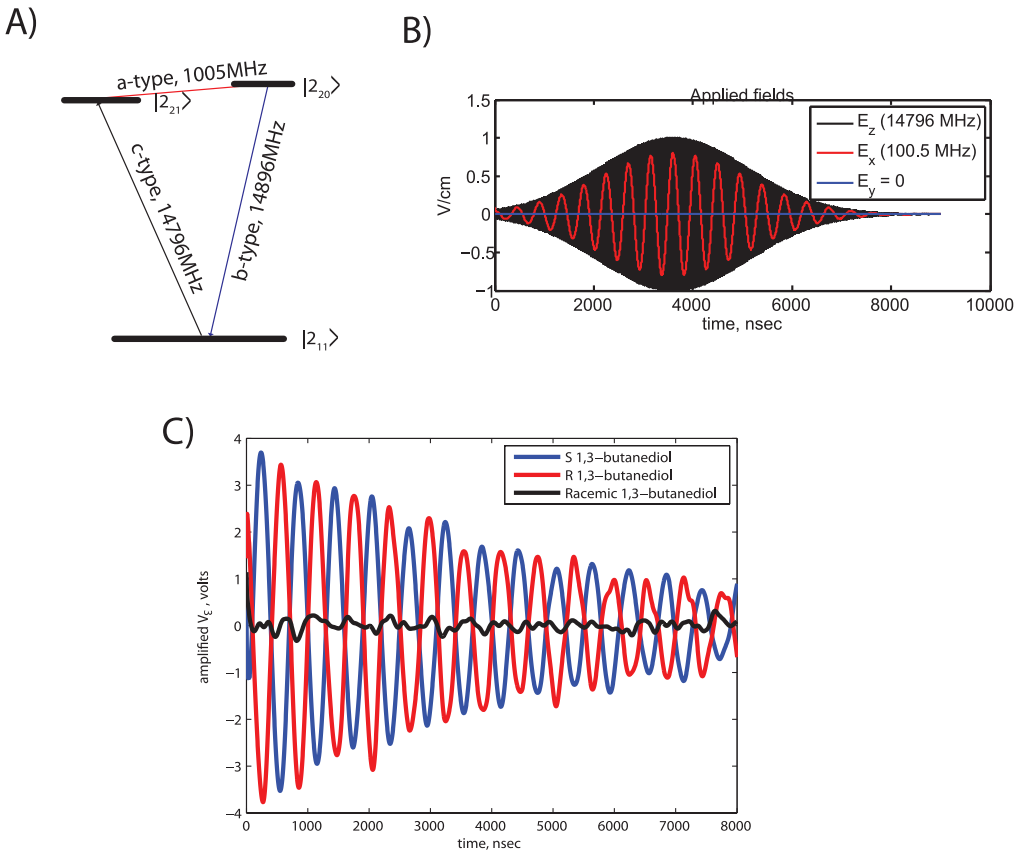

Figure 6.1.2: The enantiomer-sensitive spectroscopy method. A) A triad of states in 1,2-propanediol which results in an enantiomer specific phase in the emitted b-type radiation. B) The time profile of the applied fields which produces the enantiomer-specific signal. C) The measured signal for 1,3-butanediol. This signal is emitted at 14884 GHz, but is digitized at an intermediate frequency of 36.2 MHz and is shown mixed down to 4 MHz for clarity.

who separated crystals of tartaric acid by hand based on their differing shapes. Currently, most purification of chiral samples is performed using biological and chemical methods. Samples may be synthesized using precursor reagents with exclusively the desired chirality. In these syntheses, each reaction must also maintain the correct chirality. This is typically accomplished using asymmetric catalytic reactions [150]. Gas chromatography can be used to separate mixtures of enantiomers[151]. In these separations, a tube is coated with an empirically determined compound, the so-called stationary phase, which itself is chiral. Typically, molecules based on sugars are used as the stationary phase[152]. As the gaseous mixture to be separated is flowed over the stationary phase, a differential affinity to the chiral stationary phase results in chromatographic separation.

Finally, the most common source of enantiopure samples is derived from living organisms, whose biology has evolved to function using only a single preferred chirality. The origin of this phenomena, called the homochirality problem, is potentially addressable by an experiment on which we performed preliminary work and is described in the following section of this chapter[153].

Our proposed method for chiral separation has four individual steps:

1. Generate a rotationally cold beam of molecules using a supersonic expansion jet.

2. Populate a single rotational state with a single enantiomeric form using phase controlled microwave pulses.

3. Propagate the molecular beam through closed Moire gratings.

4. Deflect the desired state through the gratings using near resonant microwave fields.

A key feature of the proposed chiral separation process is that it is a fully coherent, quantum state specific process. This property of the process is unique among all other chiral separation techniques. Quantum state-specific separation experiments have a rich history in their own right, starting from the famous Stern-Gerlach experiment, which separated the spins states of silver atoms.

A variety of interesting physics and chemistry experiments are possible with enantiomer and state pure beams. Two enantiomers of a given molecule are in general separated by a potential energy barrier. A reconfiguration of the bonds in the molecule would allow conversion from enantiomer to another. In general, the molecular Hamiltonian commutes with parity

$$[\hat{P}, \hat{H}_{\mathrm{mol-EM}}] = 0 \tag{6.1.1}$$

, where $\hat{H}_{\mathrm{mol-EM}}$ is the molecular Hamiltonian containing only electromagnetic interactions. Therefore, molecular states are simultaneously eigenstates of parity and energy, and therefore must be linear combinations of different chiralities

$$|\Psi^{\pm}\rangle = \frac{1}{\sqrt{2}}\left(|\Psi^{R}\rangle \pm |\Psi^{L}\rangle\right) \tag{6.1.2}$$

. As a result, a molecule prepared in a single enantiomer must be a non-stationary state and exhibit interconversion dynamics. These dynamics have never before been observed. However using our method to coherent prepare an enantiopure state, we should be able to observe these interconversion. If a parity-violating molecular Hamiltonian is instead considered, the two chiral eigenstates will not be simultaneous eigenstates of energy and a relative energy shift could be observed. We discuss preliminary work towards such an experiment in the following section. By performing such an experiment with an enantiopure sample created by this coherent separation method,

fully-spectroscopic switching of the handedness of the sample is possible. This would allow a dramatic reduction in the potential systematic errors in such a measurement. Additionally, this separation method could allow the study of collision induced enantioconversion and even enantiomer specific collisions and chemical reactions.

6.1.1 Coherent state population transfer scheme

Just as the phase of the emitted radiation in the three wave mixing scheme depends on the enantiomeric content of the population in the initial state of the triad, a scheme to selectively populate a rotational state with a single enantiomer is possibly by phase control of applied microwave fields. Our scheme for selectively populating a single rotational state with a specific enantiomer involves irradiating the molecules with three fields which with a fixed phase relationship between. The fields are polarized along mutually orthogonal lab frame axes and drive a connected triad of states, just as in the three-wave mixing scheme. The results of a numerical simulation of this process is shown in Figure 6.1.3. An interference of the probability amplitudes for the population in the selected state leads to this population transfer, which is fully coherent. Either chiralty can be produced, and can be switched quickly by simply changing the phase relationship between the fields. This process should yield state purities which are better than the limit imposed by other steps in this purification process.

6.1.2 Moire deflectometry

Moire deflectometry is a fascinating and powerful method of detecting small transverses forces using a beam of particles. The classical Moire effect involves the appearance of interferometric patterns when two periodic structures are superimposed at

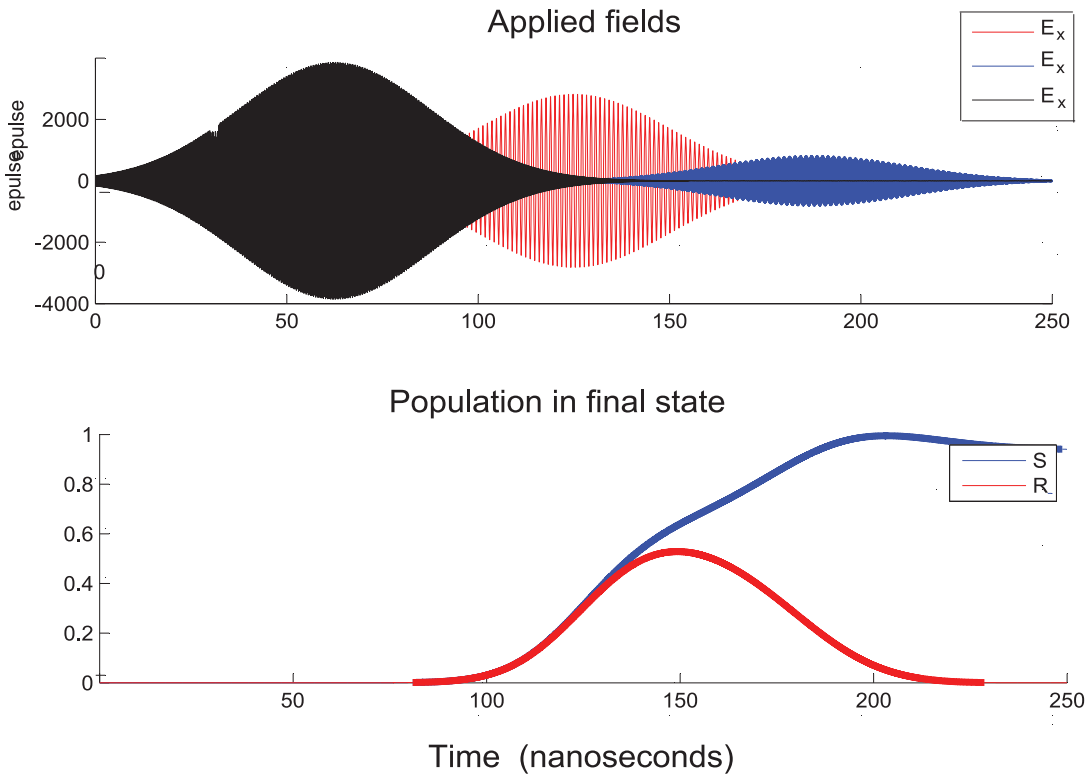

Figure 6.1.3: A numerical simulation of the proposed coherent population transfer scheme. Simulations courtesy of Dave Patterson

slight angles or offsets. A Moire deflectometer, which encounters similar patterns, is an apparatus which creates many spatially narrow and narrow in transverse momentum particle beams using a pair of plates with aligned, small apertures, which we call gratings. A third plate is then aligned with the initial two, such that any perturbation of the filtered beam results in the change of transmission through the final plate. The spread in the transverse velocity of each of the narrow beams is controlled by the distance between gratings and the size of the aperture in the gratings. For a diffuse beam, such as our pulsed supersonic jet beam source, beams are not just coincident with the central direction of the original beam, but also traverse the gratings at a velocities geometrically defined by the transverse distance between grating apertures. A schematic of operation of a Moire deflectometer is shown in Figure 6.1.4. A cartoon showing the transverse velocity distribution after the two defining gratings in a Moire deflectometer is shown in Figure 6.1.5. Moire deflectometers have been used in atomic systems, for example to measure inertial forces in metastable argon [154], in exotic systems such as anti-protons, where weak forces were detected in hopes of performing a gravitational equivalence test [155] , and have been proposed for molecular systems as well, for example to sort non-polar molecules [156].

The sensitivity of the Moire deflectometer is determined by the both the forward velocity of the beam and dimensions of the deflectometer, i.e the size of the apertures and the length of the deflectometer. To detect a transverse force of magnitude F, the required slit width w is

$$w \leq \frac{L^2 F}{v_f^2 m}, \tag{6.1.3}$$

where L is the length of the deflectometer and v_f is the forward velocity of the beam. The squared dependence of the slit width comes from both the geometric scaling of the width against the length, and also the interaction time of the force

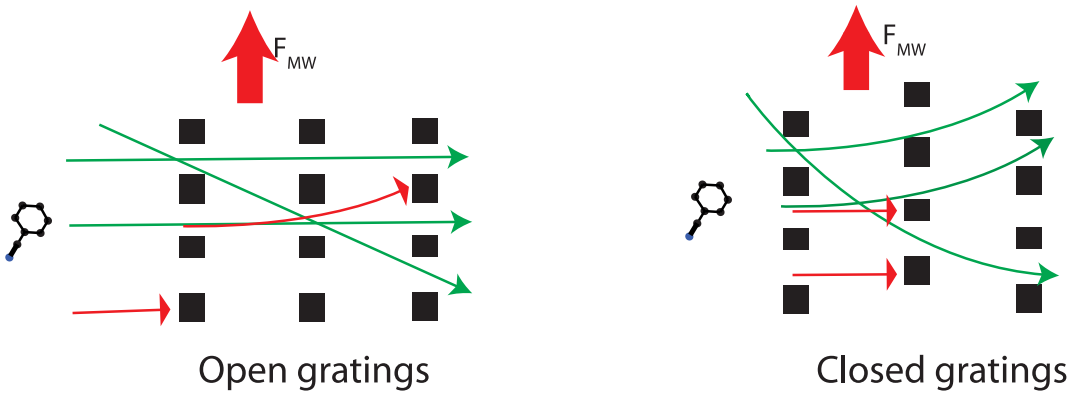

Figure 6.1.4: A schematic describing the operation of a Moire deflectometer. In the open configuration, only trajectories which do not experience an transverse acceleration are allowed through the grating. In the closed configuration, which is typically used to detect the presence of transverse forces only allows through paths which are selected by the first grating and experience the correct amount of deflection to pass around a barrier one slit width wide.

scaling with the length and forward velocity. The state-specific transverse force we will apply is a near-resonant microwave field. The AC-stark shift induced by the near resonant field is given by

$$\Delta E = \frac{\hbar}{2}\left(\delta + \sqrt{\Omega(r)^2 + \delta^2}\right), \tag{6.1.4}$$

where $\Omega = \mu \cdot E(r)$ is the Rabi frequency and δ is the detuning of the microwave field. The resulting force comes from the gradient in the electric field intensity

$$F(r) = -\nabla U = -\hbar\left(\frac{\Omega(r)\frac{\partial\Omega}{\partial r}(r)}{\sqrt{\Omega(r)^2 + \delta^2}}\right), \tag{6.1.5}$$

which for a parallel wire geometry would depend on the linear gradient in the direction out of the plane of the parallel wires. The AC field will also deflect other states at second order. Thus in order to keep the purity of the beam, we need to minimize the off-resonant stark shift which would deflect undesired states. Using second order

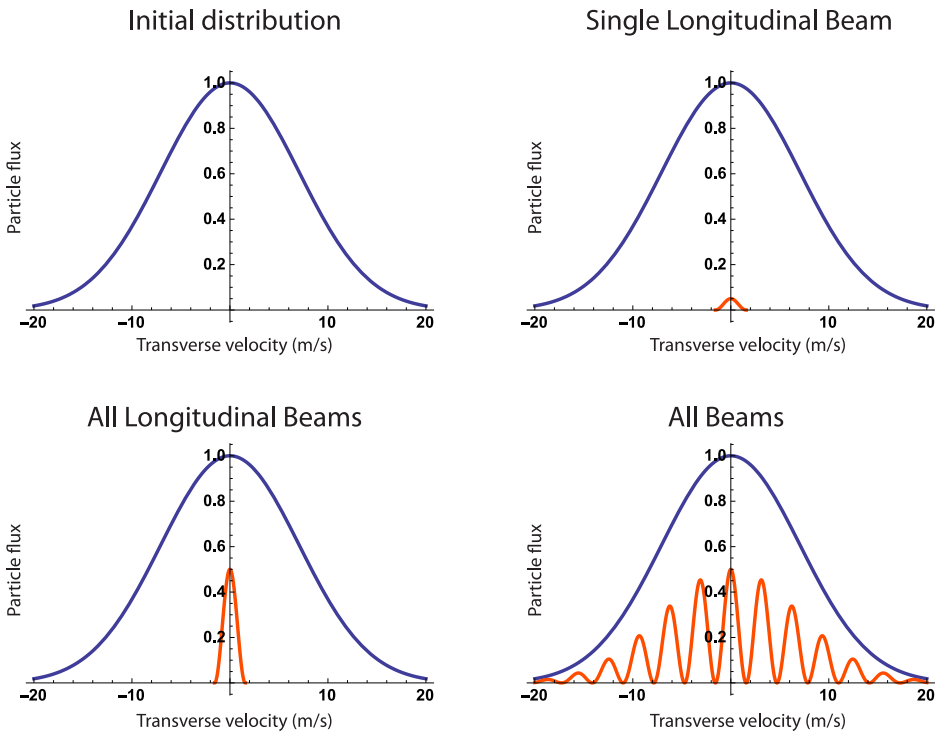

Figure 6.1.5: A cartoon representation of the transverse velocity distribution in a Moire deflectometer after filtering by the first two gratings. Distributions are not to scale for our apparatus. Clockwise from top left: The initial velocity distribution. A single longitudinal beam selected by a pair of apertures. All longitudinal beams selected by all apertures. All beams from a diffuse source, which include beams at angles defined by the tranisverse spacing of the apertures.

perturbation theory, the energy shift En for a polar molecules due to a weak field is

$$\Delta En \approx \frac{d^2 E^2}{hB}, \tag{6.1.6}$$

where B is the rotation constant of the molecule in frequency units. A dimensionless parameter

$$\alpha = \frac{dE}{B} \tag{6.1.7}$$

describes how polarized the other states are for an applied field E. A conservative estimate of the desired value of $\alpha = 0.01$ should be on-par with other purity limiting effects. Therefore the magnitude of the electric field, and hence force one can apply is limited by the desired specificity of the deflection force. For typical molecular parameters of $d \approx 3$ Debye and $B \approx h \times 3$ GHz, this requires $E \lesssim 10$ V/cm.

Using this requirement, we can calculate the force from a near-resonant microwave field, and hence the required grating geometry. The achievable Rabi frequency is therefore $\Omega \approx 10^7$ Hz. For a gradient of $\partial\Omega/\partial r \sim 10^9$ Hz/m, and a detuning of $\delta = 20$ MHz, the resulting acceleration a on a 100 amu molecule is $a = 10^{-25}/10^{-25} = 1$ m/s^2. A careful simulation suggests that in practice, accelerations of $a \sim 10^1$ m/s^2 are achievable. Then, using a forward velocity of $v_f = 500$ m/s and a deflectometer length of 10 cm, the required slit size is therefore $w = 0.1^2 * 10/500^2 = 4$ μm. This is comparable to the requirement of the inertial sensing in [154] . These gratings are easily fabricated by lithographic techniques and a set was made for us by Bo Dwyer.

A number of other weak forces could be detected on molecules which could be interesting. One possibility is to make a rotationally-state pure or nearly pure beam. As a prelimary step towards chiral separation, we achieved the alignment of a Moire deflectometer capable of producing such a beam. In a polar asymmetric top molecule,

the likelihood of having two very closely spaced rotational levels of opposite parity is quite high. If a pair of rotational levels were closely enough space compared to the other populated levels in the sample, these states would experience a linear Stark effect while all other states would experience a suppressed 2nd-order stark effect. Then, only the closely spaced states would be deflected by a static electric field. In benzonitrile, two such states are $|4404\rangle$ and $|3303\rangle$, which are spaced by as low as a few MHz at zero field. At this spacing, a field gradient of $dE/dr = 10^3$ V/cm^2 could be applied, leading to a required slit width of only $w = 100$ μm. A set gratings with a slit width of $w = 75$ μm were lithographically fabricated in 2 mil thick SS for us by Tech Etch. These gratings and their profile is shown below in Figure 6.1.6.

Another interesting possibility is to observe the absorption of a single photon by a molecule. Typically, the observation of the absorption of a single photon by a system is inferred from the later emission of that photon. However, an IR photon exciting a vibrational mode in a large molecule would remain 'in' the molecule during the duration of it's time in the deflectometer, which would allow for the direct observation of the photon absorption recoil momentum. Such an effect would require a grating slit width of $w =\lesssim 1$ μm.

6.1.3 Apparatus

The apparatus used for the chiral separation is based on a pulsed supersonic jet apparatus. This apparatus is the first and only supersonic jet in our lab and was an instructive experience which has given an appreciation for how the vast majority of cold, large molecule experiments are done in the world. It was largely constructed by Dave Patterson and Sandra Eibenberger. The center of the physical apparatus is the outer vacuum chamber, which is the standard Precision Cryo 20"x20"x24"x1/2"

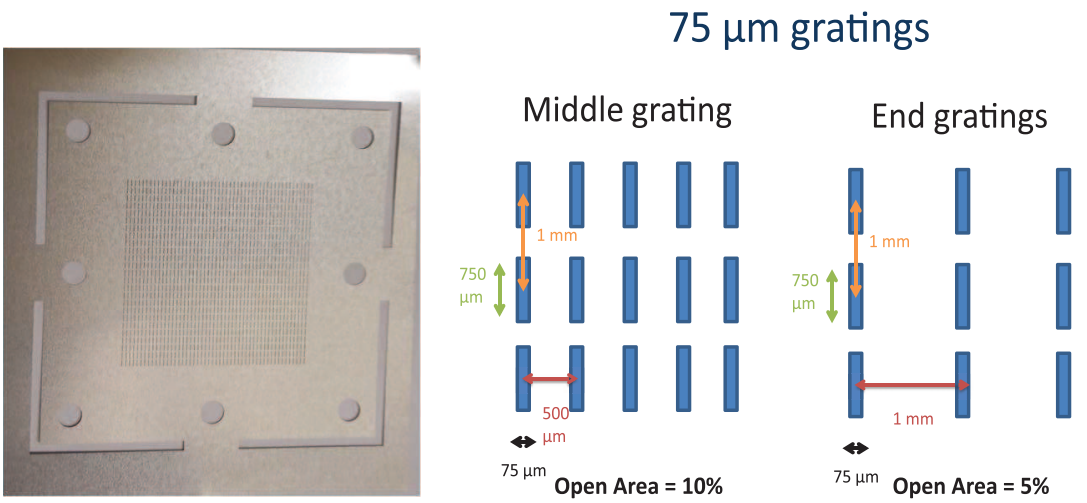

Figure 6.1.6: 75 μm Moire gratings used in the experiment. Left is a photograph of the actual grating and on the right is a schematic layout of the end and middle gratings. These gratings have a slit width small enough to see off-resonant electrostatic deflection of a single or few rotational states using modest electric fields. The middle grating can have twice as many slits as the end grating as a straight path which connects laterally adjacent gratings on either end of the deflectometer intersects the plane of the middle grating at half the lateral distance.

square aluminum dewar used in the lab. The vacuum chamber is supported from below by an extruded Al 80-20 frame. The pulsed jet assembly is located on one of the lateral sides of the chamber. The electronic and cryogen feed-throughs as well as the vacuum pumps are located on the top plate of the vacuum chamber. The control electronics and microwave sources are located in a rack next to the vacuum chamber and all microwaves are introduced in the chamber via flexible microwave coaxial cables.

The interior of the vacuum chamber is divided into roughly three sections. The first section is called the microwave region, and is where the supersonic expansion and microwave manipulations take place. Microwave dection to ensure proper cooling also takes place in this region. The supersonic expansion is formed by a Parker Hannifin Series 9 pulsed valve which is built in to a feed-through assembly which places the opening aperture of the valve inside the inner volume of the chamber and clear of the walls. Special care is take not to place any object too close to the aperture to ensure unobstructed expansion of the gas pulse. This region has several microwave horns, the microwave switch, and and low noise microwave amplifier. Typically the horns are placed in a standard FID set-up to enure that a rotationally cold supersonic expansion has formed. There is a dedicated Agilent V-550 turbo-pump for this section which allows rotational supersonic beam formation at repetition rates of a few Hz using a backing pressure of approximately $P \approx 2$ atm of typically neon gas. This region is isolated from the other regions using viton seals, with the only conductance into the following regions through a central conical aperture.

The next region, called the Moire region, is approximately 30 cm in length and is where the actual deflection occurs. The moire gratings are held by optics mounts which are secured to an elevated optics breadboard. The middle optics mount is

located on a smaller secondary optics breadboard which is mounted to the larger breadboard by a home made flexure stage made from formed SS shim stock. This secondary breadboard can be moved laterally by a high accuracy stepper motor which is secured to the larger elevated breadboard. The tip and tilt degrees of freedom of each optics mount can, in principle, be controlled by stepper motors as well. The near resonant microwave field would be applied between the gratings of the deflectometer assembly.

Signal arising from molecules which entered the final detection region but did not pass through the entire deflectometer assmebly are the principle source of background for the experiment. Most molecules are either blocked by the gratings or miss them entirely. These molecules can still enter the detection region after first sticking to the apparatus, and then beign re-emitted along a trajectory significantly differing from the original molecular beam. This allows them to pass through a fraction of the gratings, or none at all. High pumping is critical to reducing this background, which otherwise slowly and stickily diffuses around the chamber.

Primary pumping is provided by a separate Varian V-550 turbo-pump pump. However, additional and substantial pumping of the seeded species is achieved with Cryo-pumping. I fabricated a liquid cryogen pot, which was placed into the main volume of the Moire region. This pot is normally run at liquid nitrogen temperatures and its hold time is typically 4 hours, but it's stability is not critical to the experiment. Large cryo-pumping fins extend off this pot to increase the effective cryo-pumping speed. The transition into the final region is made using several overlapping cold tubes which are thermally anchored to the pot. This ensures that only molecules with, to first order, a trajectory which would have taken them through the Moire deflectometer make it into the detection region. Additionally, a movable paddle is

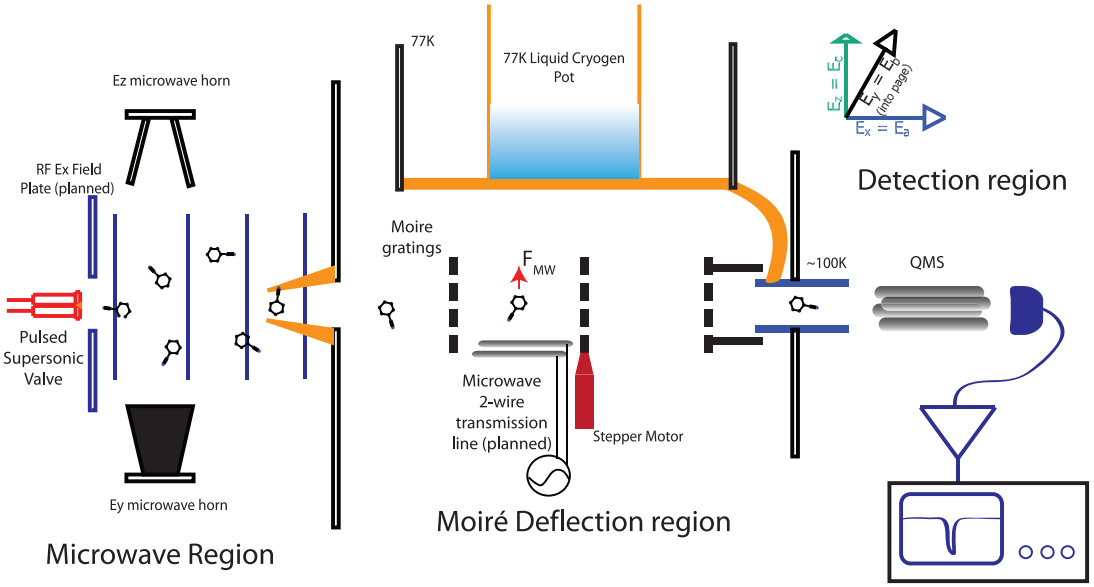

Figure 6.1.7: A schematic of the Moire deflectometer. Depicted here is the the coherent population transfer set-up in the microwave region. After preparation of the desired rotational state, molecules pass through the deflection gratings in the 'closed state,' where only the state of interest is deflected through the gratings by the near resonant microwave or DC electric field generated from the transmission line. Successfully deflected molecules enter the detection region where they are ionized, mass filtered, and detected with an electron multiplier.

mounted through a motion feed-through to allow blocking of the Moire trajectories for diagnostic purposes.

The final section is the detection region, which houses an SRS RGA with direct analog access to the electron multiplier unit. This RGA, which ionizes passing molecules and filters the ions by mass before collecting them in an amplifying electron multiplier unit, allows species specific ultra-high sensitivity detection capabilities. The output of the electron multiplier is sent through an SRS low noise pre-amplifier and read out on an oscilloscope which is trigger by the same TTL pulse which triggers the valve to open. The microwave electronics are identical to those described in preceding chapter of this thesis. A schematic of this set-up is shown in Figure 6.1.7.

6.1.4 Moire fringes using micron-scale gratings

A useful diagnostic signal is the Moire fringe. As the middle grating is translated in position by the stepper motor, the gratings should move from open to closed. This variation of the signal, usually periodic is called a Moire fringe. The contrast of the fringes is key to the performance of the deflectometer. In particular, the purity of the resulting deflected beam scales linearly with the contrast. In our deflectometer, we are aiming for $> 99\%$ contract. Many rotational states exist in the molecule beam and a 1% contribution from each undeflected state will quickly add to a substantial fraction of the total detected signal.

Alignment of the gratings is a challenging and critical procedure. A misalignment of the gratings will cause a reduction in contrast, and strict tolerances are required to even observe Moire fringes in the first place. The in-plane rotation of the gratings is the most sensitive alignment, requiring $\Delta\Theta < 0.2$ degrees for the 75 μm gratings. The out of plane rotation must be within $\Delta < 0.8$ degrees for the same gratings. Additionally the longitudinal spacing of the gratings is important - each of the gratings must be equidistant, with $|x_1 - x_2| < 375$ μm, where x_1 and x_2 are the distances between the first and second, and second and third gratings respectively to observe fringes. Course alignment was achieved with a pair of precision machined spacer blocks. Fine alignment was achieved empirically using the diffraction patterns of red laser pointer through the gratings.

A typical molecular beam signal as recorded by the continuous electron multiplier (CEM) under optimal conditions is shown in Figure 6.1.8. Using a programmable Newport stepper motor, we can scan the lateral position of the middle grating to trace out a Moire fringe. When properly aligned and with all of the cryo-pumping described in the preceding section, Moire fringes were observed in both a set of ma-

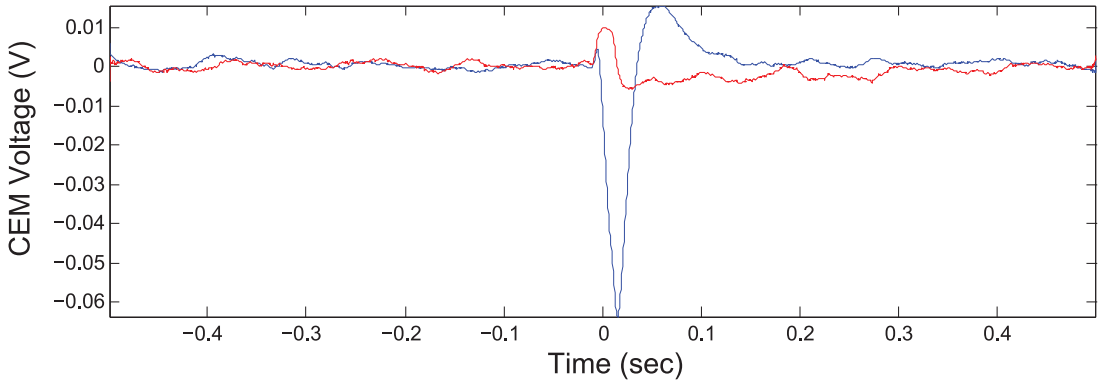

Figure 6.1.8: A typical continuous electron multiplier signal (CEM) signal after amplification with no deflection forces present. The red trace corresponds to the gratings in the closed position, and the blue trace corresponds to the gratings in the open position. Negative voltage corresponds to the presence of benzonitrile molecules. Any positive voltage signal is an artifact of the amplifier, which is AC coupled and must maintain a 0 average signal. The molecular beam traverses the entire chamber in approximately 10 ms, which is visible as the time offset of the blue peak. With the closed gratings, a small molecular signal is still observed. In this run, the contrast was estimated to be $\gtrsim 95\%$.

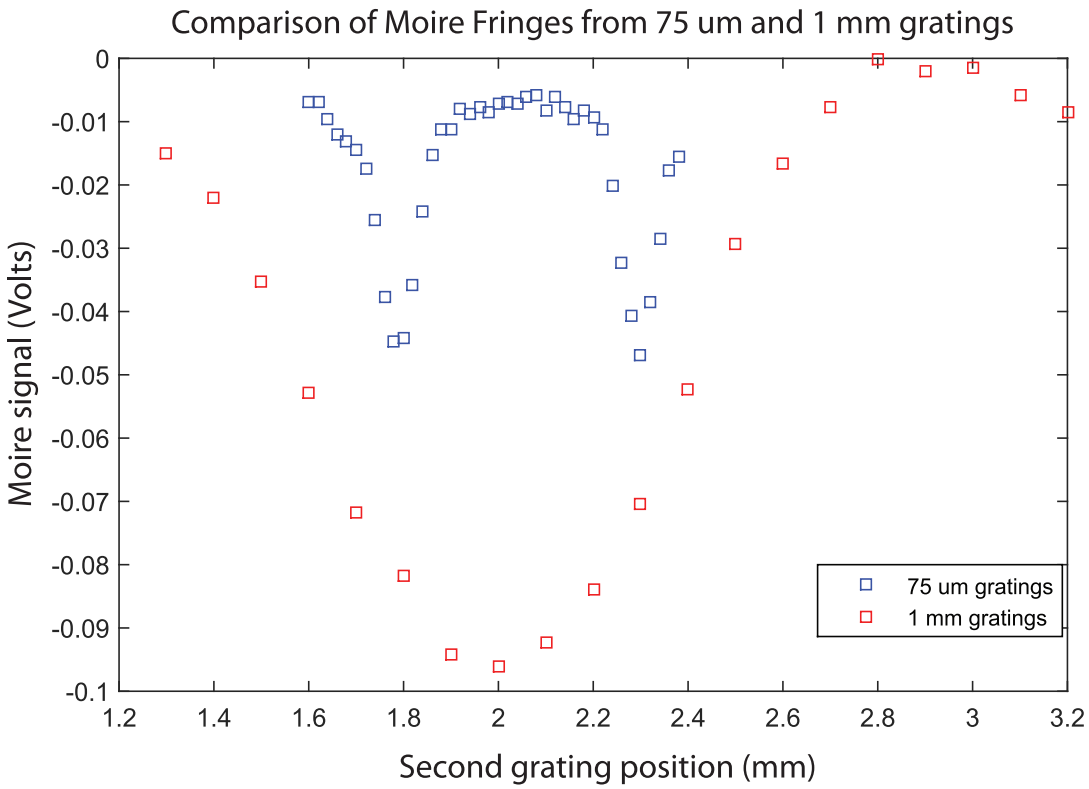

Figure 6.1.9: Moire fringes observed with both $w = 1$ mm and $w = 75$ μm gratings using a programmable Newport high precision stepper motor. The contrast of the fringes with the $w = 75$ μm gratings was between 90% and 95% and is suspected to be limited by the in-plane alignment of the gratings. The vertical scale of the two curves is not the same, but the horizontal scale is the same.

chined gratings with $w = 1$ mm and with the lithographically fabricated $w = 75$ μm gratings. Critical to the observation of the fringes with the $w = 75$ μm gratings was the proper alignment of the gratings and the cold overlapping tubes described above. The fringes from these gratings are shown in Figure 6.1.9. The contrast of the fringes with the $w = 75$ μm gratings was between 90% and 95% and is suspected to be limited by the in-plane alignment of the gratings.

The next steps forward with this experiment would be the observation of deflection through closed Moire gratings. For this, we will use the DC stark shift to deflect

the most polarizable rotational states. Additionally, the coherent state transfer step will need to be demonstrated. Current work in the lab may be showing the first signs of this working. Work is also underway in the Schnell group in Hamburg as well to demonstrate this step. Next, Moire fringes must be demonstrated with the nanofabricated 5 μm gratings. The alignment procedure and system of the gratings will likely require substantial improvement, for example using stepper motors on tip-tilt degrees of freedom of the grating mounts, perhaps a longitudinal translation stage with stepper motor, and likely improved patience of the experimenter. Near-resonant deflection of the beam will then need to be demonstrated. Finally, the entire protocol described will have to be put together. This experiment was unexpectedly difficult, and though I'm confident of it's eventual success, a skilled experimenter and significant time will be necessary. Luckily just such an experimenter, Dr. Sandra Eibenberger is now working in the lab.

6.2 Parity violation in chiral molecules

As discussed in the preceding section, the electromagnetic molecular Hamiltonian commutes with the parity operator. However, parity violating interactions are known to exits within atoms. In particular, the weak nuclear force exhibits parity violation. The observation of parity non-conservation (PNC) in atoms have served as the most stringent tests of electroweak interactions and are highly sensitive to new interactions[8]. Additionally, the PNC effects can magnified in molecules using closely spaced opposed parity levels [20]. In addition to constraining parameters in high energy physics, PNC in molecules could play in a field about as different as one can imagine - biology. PNC in chiral molecules is hypothesized to play a role in the homochirality of life[157] . In this section of my thesis, we discuss preliminary work

towards a precision measurement experiment of PNC in chiral molecules using a buffer-gas cell or buffer-gas beam source.

6.2.1 Parity Violation in Molecules

The search for parity violation in chiral molecules has been on-going for over 25 years and a major collaboration is working towards new precision measurements. In chiral molecules, parity violating energy shifts are expected to manifest in the vibrational and rotation degrees of freedom. A seminal work in 1999 placed an upper bound on the magnitude of these energy shifts in the vibrational modes of CHFClBr of $\Delta\nu/\nu < 4.10^{-13}$ using a saturated absorption measurement in a gas filled long Fabry-Perot cavity[158]. In this experiment, a measurement of the line center is was limited by statistical uncertainties at the 10 Hz, but the PNC energy shift measured was dominated by a systematic error from collisional shifts of unknown contaminant gasses. The predicted PNC shift in CHFClBr is predicted to be on the order of $\Delta\nu/\nu \sim 10^{-16}$. Shortly thereafter a competing group released a non-zero measurement of a PNC signal in a Mossbauer spectroscopy experiment using a chiral iron complex, $Fe(phen)_3Sb_2(C_4H_2O_6)_2{\cdot}8H_2O$, which was also dominated by systematic errors [159].

Current progress is directed both towards finding a molecule which might exhibit larger parity violating energy shifts and also developing more accurate spectroscopic measurement techniques and high precision light sources. An excellent review on the theory is given by Quack and Stohner in [160] and an excellent review of experiment progress is found in the review by [161], which is the collaboration currently pushing these experiments most forward. Our preliminary work on this question focuses on two fronts, using a highly sensitive candidate molecule and using high precision

spectroscopy based on buffer-gas cooling.

PNC arises in molecules arises predominately from the exchange of a Z^0 boson between the quarks in the nucleus and the electrons in the orbitals of the molecule[162, 1, 163]. Because the Z^0 has a large rest mass of $m_Z = 92.6$ GeV, it has very short range and can only interact with electrons which penetrate the nucleus. While the electromagnetic current is only in vector form

$$j^\mu \left[\psi(x)\right] = \psi^\dagger(x)\gamma^0\gamma^\mu\psi(x) \tag{6.2.1}$$

, where $\psi(x)$ is the wavefunction operator for the electron is bispinor form, the weak neutral currents have both vector components and axial (pseudo) vector components, the latter of which is

$$j^\mu \left[\psi(x)\right] = \psi^\dagger(x)\gamma^0\gamma^\mu\gamma^5\psi(x) \tag{6.2.2}$$

While the electromagnetic current's vector nature renders its interactions parity conserving, the interaction of the electromagnetic current and the weak neutral current violates parity. The dominant contribution to the parity violating effect arises from a pseudo-vector coupling of Z^0 to the electron and a vector coupling to the nucleus. In particular, this interaction is dominated by the time-like ($\mu = 0$) component of the weak neutral current, i.e. the weak neutral charge

$$Q_W = -N + Z\left(1 - 4\sin^2\left(\theta_W\right)\right), \tag{6.2.3}$$

where $\theta_W \approx 0.24$ is the Weinberg mixing angle which describes the spontaneous symmetry breaking of B^0 and W^0 bosons into photons and Z^0 bosons. The resulting

Hamiltonian for this interaction is

$$H_{PV} = \frac{G_F}{\sqrt{8}} \sum_A Q_{W,A} \gamma^5 \rho^A(r), \tag{6.2.4}$$

where $G_F \approx 3 \times 10^{-12} mc^2 \left(\frac{\hbar}{mc}\right)^3$ is the Fermi constant and $\rho^A(r)$ is the weak nuclear charge distribution for nucleon A. In the non-relativistic limit, this Hamiltonian reduces to

$$H_{PV} = \sum_A \frac{G_F}{\sqrt{2}} \frac{1}{2mc\hbar} Q_{W,A} \vec{S} \cdot \left[\vec{p}\delta^3(\vec{r}) + \delta^3(\vec{r})\vec{p}\right], \tag{6.2.5}$$

where $\vec{p}$ is the linear momentum operator on the electron and $\vec{s}$ is the electron spin. This Hamiltonian mixes electron orbitals of different orbital angular momentum L due to the action of the linear momentum operator. Evaluation of this Hamiltonian on hydrogen electron orbitals shows that this mixing

$$\langle n'p | H_{PV} | ns \rangle \propto Z^3. \tag{6.2.6}$$

One factor of Z comes from the increase in the the weak neutral charge on the nucleus, another from the increased electron density in the S orbital from the nuclear electrostatic charge, and one from increased momentum of electron nuclear a more charged nucleus. In molecules this effect requires further spin-orbit mixing in order see a non-zero matrix element. Thus for a chiral molecule,

$$\Delta E_{PV} \propto Z^3 \times \Delta E_{SO} \propto Z^5. \tag{6.2.7}$$

To observe parity violation in a chiral molecule, one must choose a molecule with as heavy a nuclei as possible.

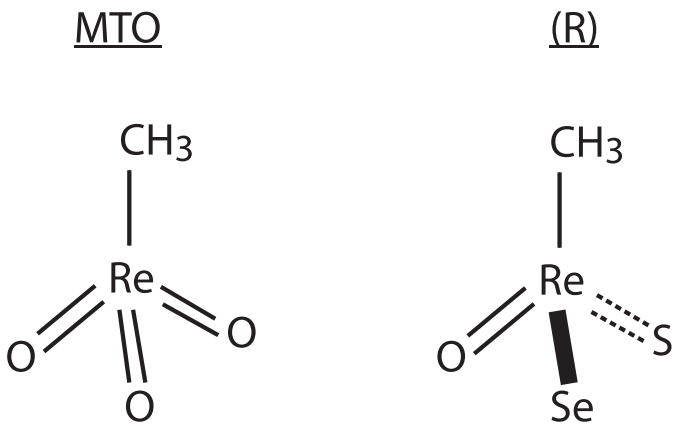

Figure 6.2.1: The Lewis diagram for methyl trioxorhenium (MTO) and a right handed chiral derivative. These molcules are expected to show large parity non-conserving energy shifts and have ideal properties for a molecular beam spectroscopy experiment.

6.2.2 Methyltrioxorhenium as a candidate molecule

Recent research has focused on a set of molecules based on a rhenium metal complex [164]. Rhenium is a third-row transition metal with atomic mass of 186 a.m.u. This makes it one of the heaviest species for which a diverse set of transition metal chemistry is known. In particular, chiral oxorhenium complexes have been identified as ideal candidates for a PNC search in chiral molecules. Due to the heavy Re nucleus, MTO is predicted to manifest PNC energy shifts on the order of $\Delta\nu/\nu \sim 10^{-14}$ or higher. Chiral oxorhenium complexes are readily synthesized from commercially available methyltrioxorhenium (MTO). Additionally, these complexes can sublimate at moderate temperatures without decomposition, no internal rotations are present, and the hyperfine structure is relatively simple. Microwave spectroscopy of MTO has already been performed and has identified the rotational constants, centrifugal distortion, and hyperfine constants[165]. The Lewis diagram of MTO and a chiral derivative are shown in Figure 6.2.1

6.2.3 Buffer-gas cooling of Methyltrioxorhenium

As a preliminary step towards a precision measurement experiment of PNC in chiral molecules, we performed microwave spectroscopy of buffer-gas cooled MTO in a 6K helium buffer-gas cell. MTO is the first organo-metallic molecule to be buffer-gas cooled and one of the heaviest molecule to be buffer-gas cooled. Nonetheless, this spectroscopy experiment was very easy, working on our very first try with all data taken in a single experimental run of a few hours. The apparatus used for this experiment is identical to that described in Chapter 5 of this thesis and was run in steady state mode with a buffer-has flow of 2 sccm. MTO is a symmetric top molecule and has one rotational line, split by hyperfine structure, in the bandwidth of our instrument. Rhenium has two abundant isotopes, ^{185}Re and ^{187}Re which exhibit isotopes shifts. We recorded a broadband spectrum of MTO from 13.8 GHz to 14 GHz. This spectrum, along with the line assignments, is shown in Figure 6.2.2.

6.2.4 Towards a parity violation search in a buffer-gas beam or cell

The current generation of PNC measurement in molecules is proposing to use a Ramsey style measurement in a supersonic beam. This will allow line-widths on the order of 100 Hz, as opposed to the 60 kHz of the original 1999 experiment. Additionally, the free beam environment should eliminate the collisional shifts which caused the dominant systematic error in that experiment. A buffer-gas beam source for this experiment would represent a strictly beneficial increase in the sensitivity of this experiment. The sensitivity in a Ramsey experiment is

$$S \propto \tau\sqrt{N}, \tag{6.2.8}$$

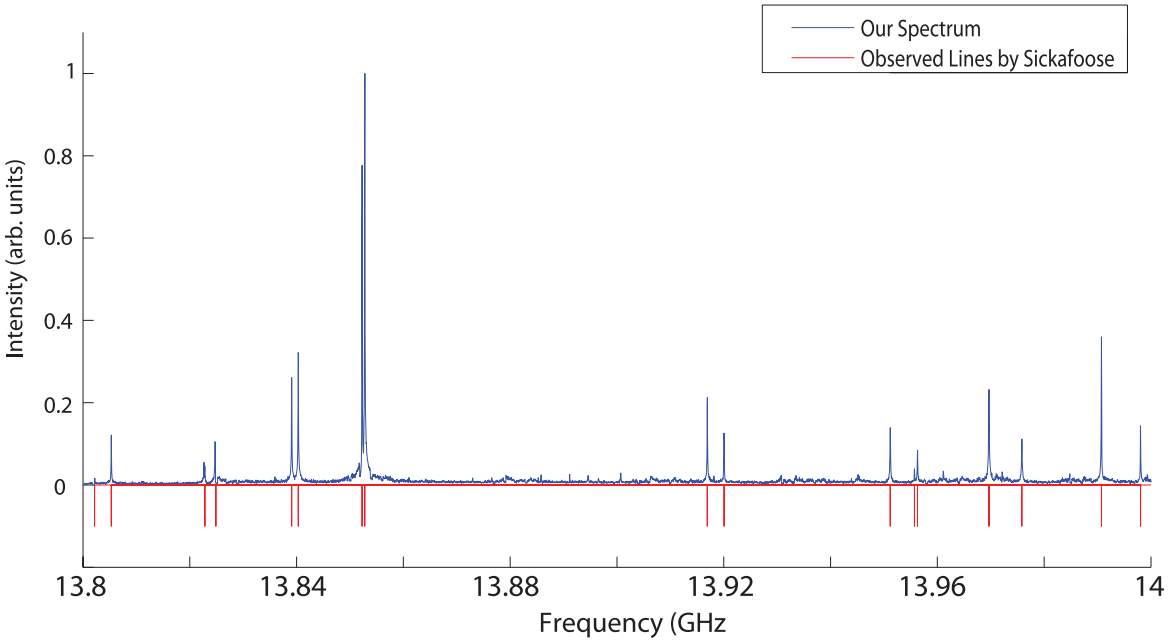

Figure 6.2.2: FTMW spectrum of buffer-gas cooled MTO showing hyperfine splittings and isotopomers. The spectral lines observed in reference [165] are plotted below the spectrum in red. Some of the lines in the spectrum have not been previously identified.

where τ is the coherence time of the measurement and N is the number of molecules being measured. A neon buffer-gas beam operated in the hydrodynamic regime could achieve a forward velocity of $v_f \approx 150$ m/s, one sixth that of a pulsed supersonic beam, and additionally could produced over an order of magnitude more molecular flux. This would give a sensitivity $S \gtrsim 20$ times greater than an equivalent pulsed supersonic jet experiment.

A measurement in a buffer-gas or supersonic beam would have a major systematic - the second order Doppler shift. This shift, due to the time dilation experienced in a moving beam is $\propto v_f^2$. In a supersonic beam, control of v_f is difficult. However, in a buffer-gas beam, would have this systematic reduced by a factor of $\left(\frac{1}{6}\right)^2$and is the magnitude of v_f is easier to control. In a buffer-gas cell, this systematic would be eliminated. Despite the much wider line shape in a cell, which we be on the order of

MHz for optical frequencies, a much higher molecule number and lack of 2nd order Doppler shift could make this a promising alternative to a beam based measurement. Recently, ultra-high precision spectroscopy of organic molecules was achieved in the buffer-gas cell with an IR frequency comb. This method could access vibrational transitions particularly sensitive to PNC energy shifts.

A particularly intriguing idea for an in-cell measurement of PNC energy shifts is the construction of a molecular MASER with chiral MASEing medium such as one of the chiral derivatives of MTO. A molecular MASER, is qualitatively different from an optical laser. In a MASER, the linewidth is set by the incredibly small natural linewidth of the rotational states of the molecule, which is on the order of 10^{-8} Hz, and not the linewidth of the cavity around it. The Schawlow-Townes limit for the linewidth of a molecular MASER in the buffer-gas cell has estimated to be well below 10^{-6} Hz, i.e. $\Delta\nu/\nu \sim 10^{-16}$ and would be fantastically sensitive. This amazing linewidth comes not just from the low natural lifetime, but also from very high number of molecules in cell. In reality, such a linewidth would be limited by technical noise sources, such as cavity noise which couples to the photons by not being deeply enough in the bad-cavity limit.

The requirements for such a MASER appear feasible. There must be an 'optical depth' of 1, i.e. unit probability of absorption of a microwave photon before loss from the cavity. A recent measurement of microwave absorption in our buffer-gas cell is on the order of 10^{-3}, and a microwave cavity with a Finesse of $F \sim 10^3$ is relatively easy to achieve. One simply needs a suitable scheme for pumping into a non-thermal distribution of rotational states, and thermal black-body photons would initiate MASEing. The output frequency of two separate MASERs using both left and right handed chiral molecules as the gain medium, or the output of the same

MASER but by using MASEing media of different handedness, could be compared to detect PNC energy shifts.

6.3 Spectroscopy of highly unstable molecules

Buffer-gas cooling of large molecules is not just a technique applicable to higher resolution spectroscopy of stable molecules and mixtures, but can also be used to perform high resolution spectroscopy on unstable molecules as well. The world is filled with unstable molecules as we speak (except we are not speaking, you are reading). Chemical reactions typically experience numerous transient reaction intermediates. Some intermediates have incredibly short lifetimes and react due to internal dynamics within the molecule. However, a large class of reaction intermediates are meta-stable, and require a collision event to proceed. A low energy helium collision may be soft enough to preserve these states. If reaction intermediates could be generated and introduced into the buffer-gas, reactions could be stopped, allowing for precision spectroscopy of critical reaction intermediates.

One important class of unstable molecule is that of carbonyl oxides, known as Criegee intermediates (CI). CIs play a critical role in the oxidation of organic molecules in the Earth's upper atmosphere[166]. For example, ozonolysis, which proceeds via CIs, is a major tropospheric removal mechanism for unsaturated hydrocarbons. The nature and properties, such as the structure, of CIs are poorly understood and experimental spectroscopy is limited due to their unstable nature. Isolation of these molecules in a buffer-gas environment is one goal.

Unstable radicals are some of the most common molecules in the universe, making up a substantial component interstellar medium (ISM). The chemistry of these radicals plays an important role in the transport of matter and formation of stars

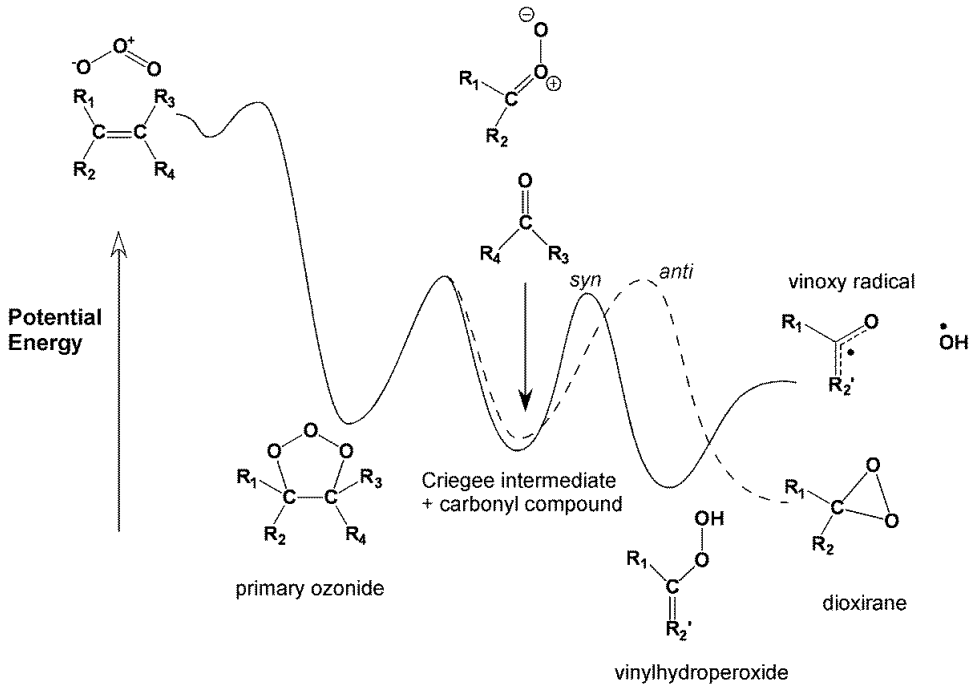

Figure 6.3.1: Reaction pathway and various intermediates in the ozonolysis of alkenes process. Figure adapted from [166]

and planets in the interstellar medium. The presence of large molecules in the ISM is quite surprising given its low density. The discovery of the molecule $c-C_3H_2$ in 1985 heralded a phase of intense study of large, reactive molecules in space[167]. These molecules belong to another class of unstable molecules which we would like to study in the buffer-gas environment.

To this end, we outfitted our pulsed valve for molecule introduction with an electrical discharge assembly provided by the McCarthy Lab. This discharge is located outside of the pulse valve, but still a few centimeters before the entrance aperture to the cell. The discharge electrodes are charged to $1-4$ kV and discharge when the pulsed valve is fired. Using an identical experiment protocol as what was described in Chapter 5 of this thesis, we observed the unstable radical $c-C_3H_2$ and the rarer molecule $c-C_3H$ using microwave spectroscopy in a 6K helium buffer-gas

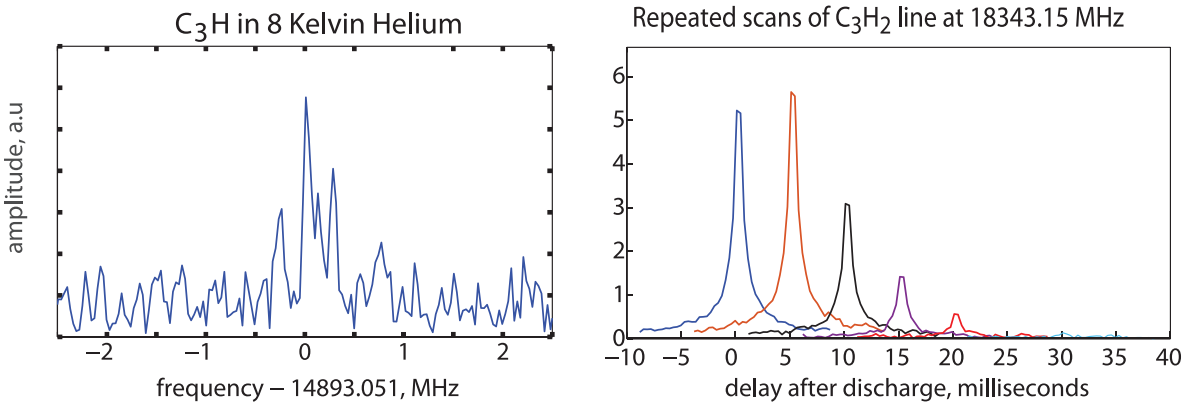

Figure 6.3.2: Unstable organic radicals c – C_3H and c – C_3H_2 observed in the buffer-gas cell after production in a pulsed discharge valve. The high unstable molecule C_3H is observed to have a splitting due to XXX.$C_3H_2$is observed in the cell the cell for over 20 ms, which itself is limited by the buffer-gas density in the cell.

cell. c – C_3H_2 was observed to persist in the buffer-gas cell for more than 20 ms with the lifetime being limited by diffusion. This suggests that c – $C_3H_2$is stable during collisions with the 6K helium buffer gas. The triplet splitting due to the free hydrogen is also observed c – C_3H[168]. This method represents a promising avenue towards observing other unstable radicals or reaction intermediates.

Appendix A

Technical Drawings

The technical drawings provided in this chapter are machine drawings for the Cold ECDL laser system presented in Section 3.2.3 of Chapter 3. They can be presented as is to a professional machine shop for fabrication. Additional technical drawings for this, and other apparati - e.g. the vacuum chamber described in Chapter 2 and second generation vacuum chamber described in Chapter 3, are found on the Laser Cooling SVN subversion repository under the Constructions and Drawings folder.

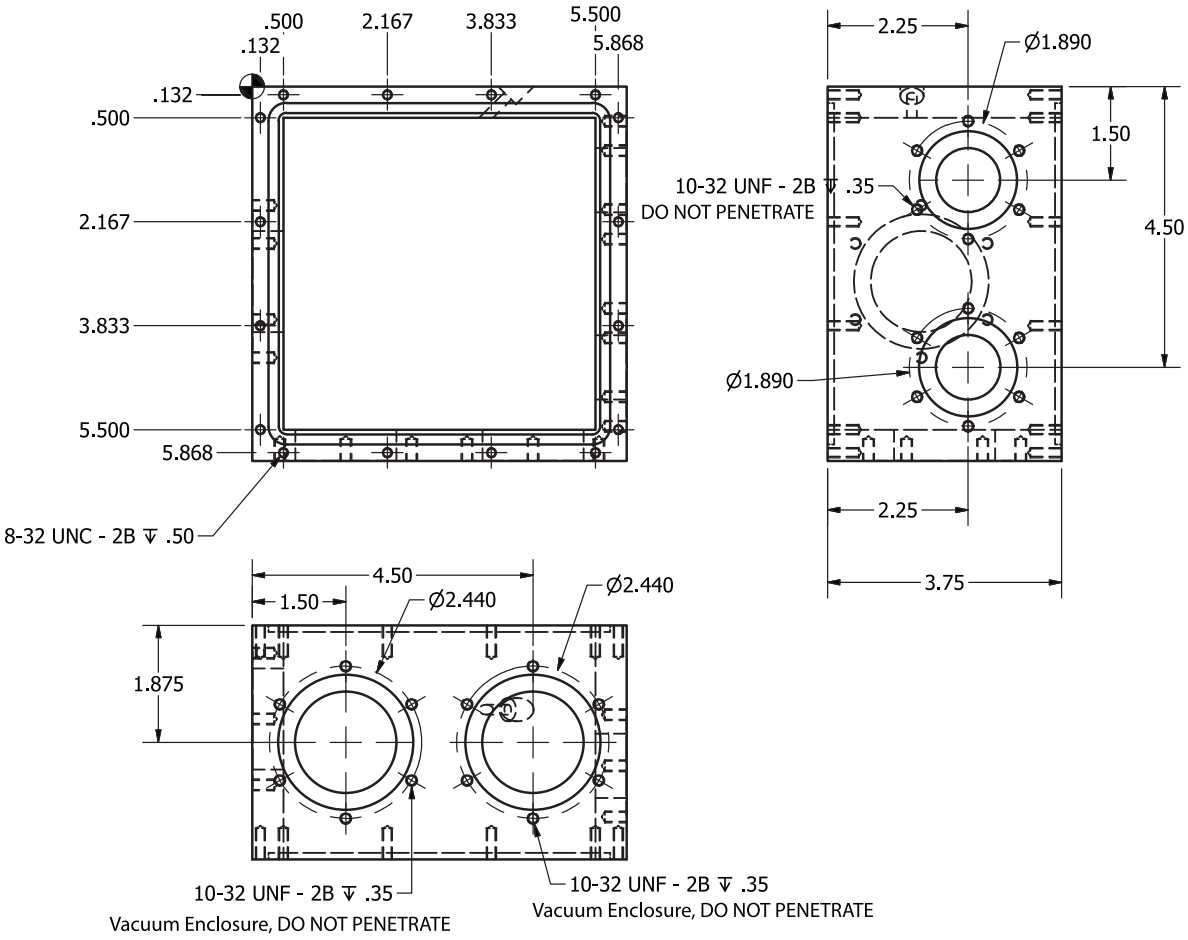

Figure A.0.1: The Cold ECDL enclosure body, page 1.

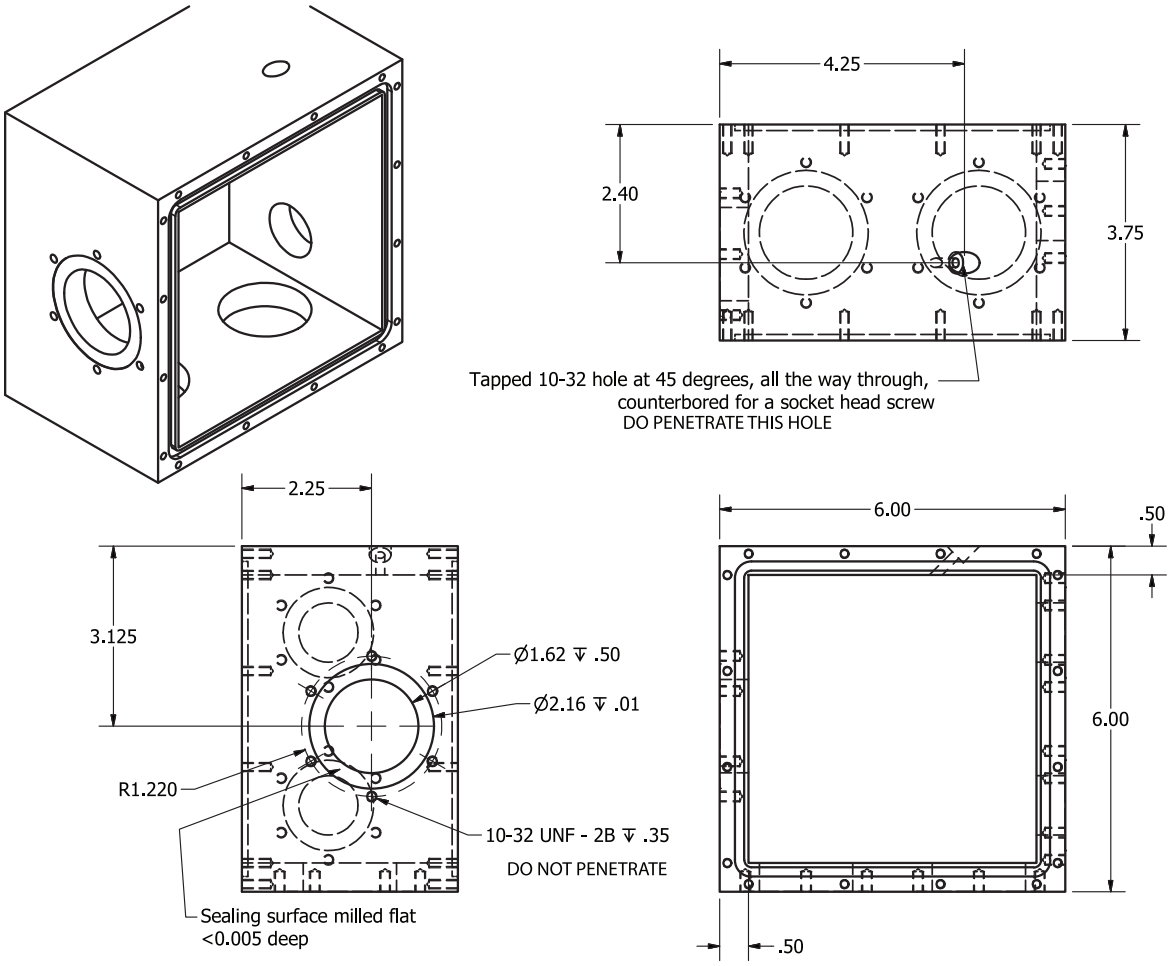

Figure A.0.2: The Cold ECDL enclosure body, page 2.

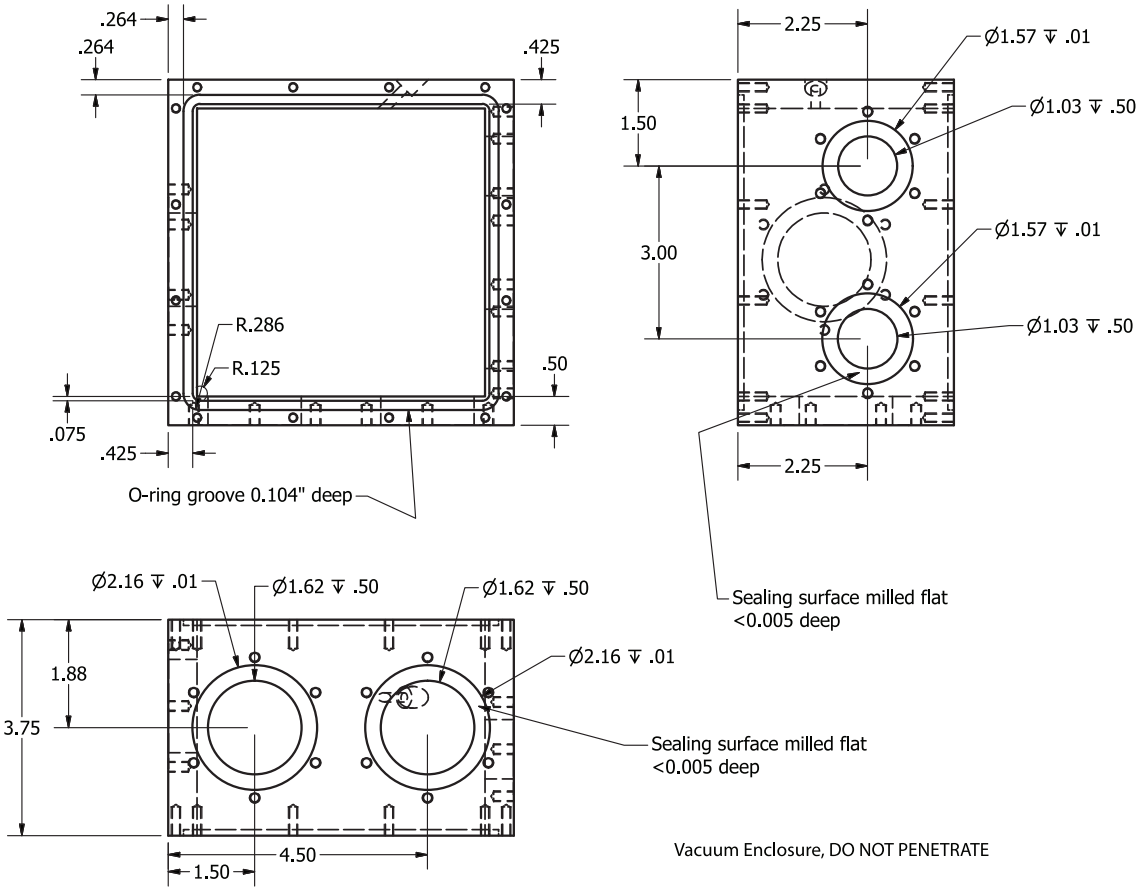

Figure A.0.3: The Cold ECDL enclosure body, page 3-o-ring grooves.

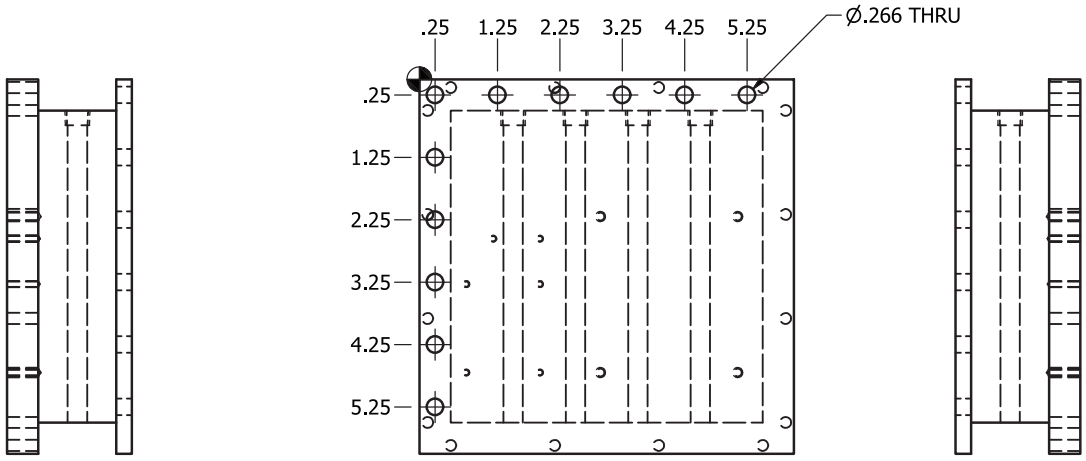

Figure A.0.4: The Cold ECDL base, page 1.

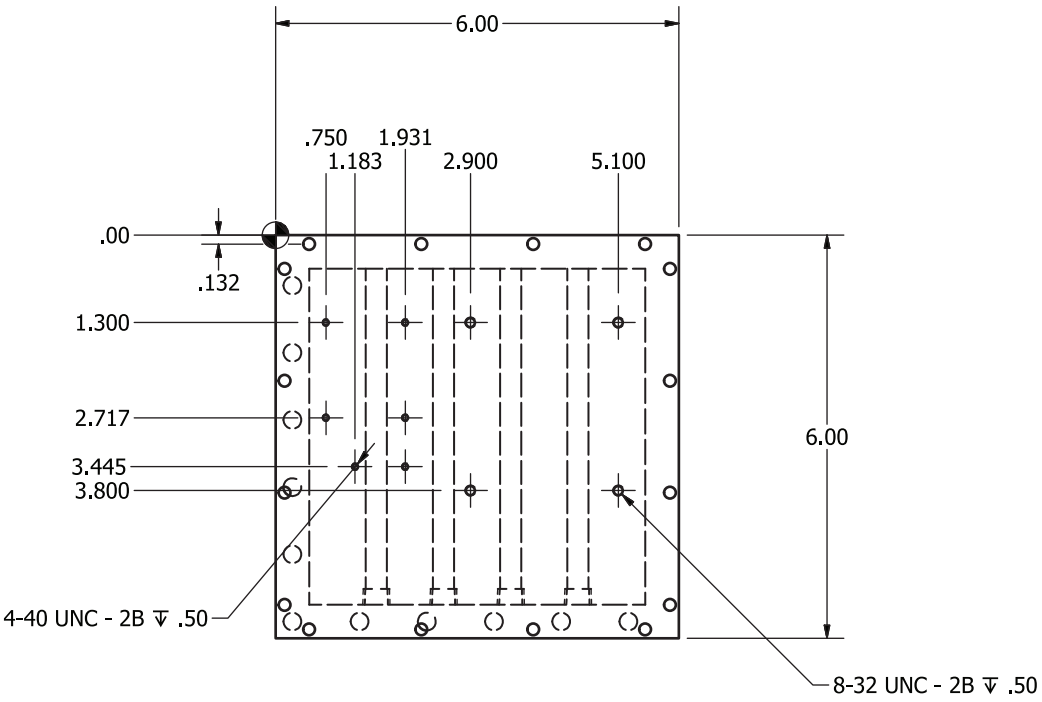

Figure A.0.5: The Cold ECDL base, page 2.

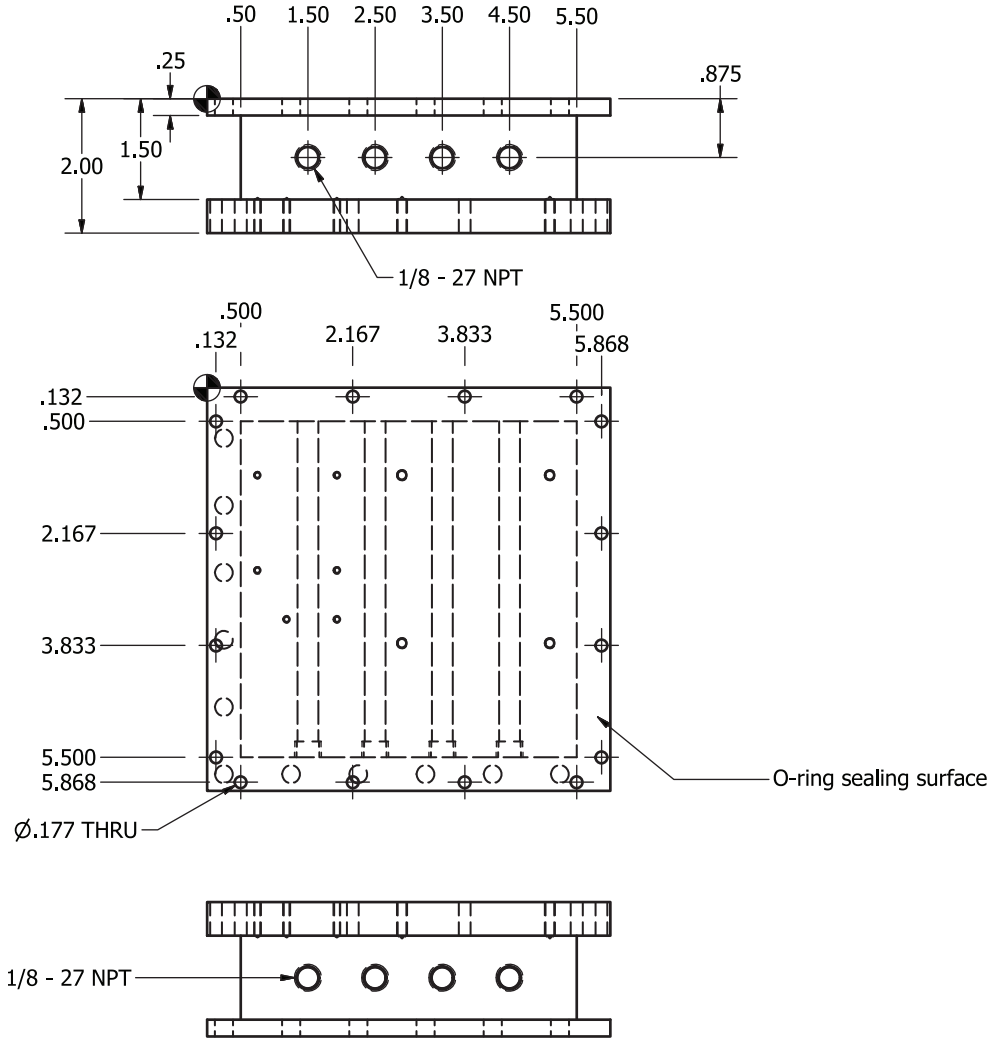

Figure A.0.6: The Cold ECDL base, page 3.

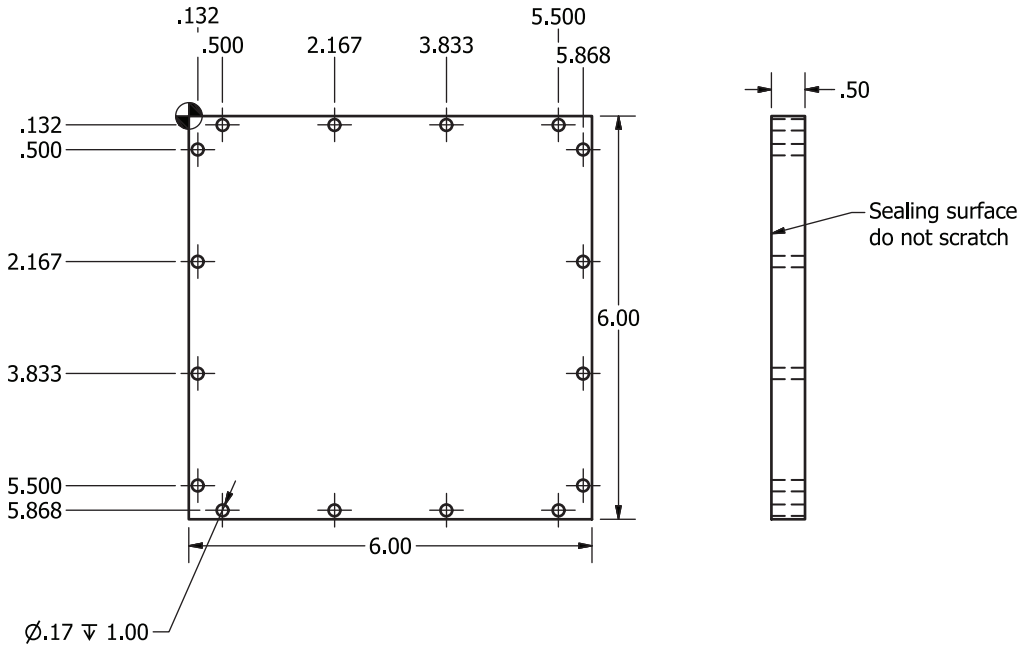

Figure A.0.7: The Cold ECDL top plate.

Bibliography

[1] D. Budker, D. F. Kimball, and D. P. DeMille, *Atomic physics: an exploration through problems and solutions*, Oxford University Press, 2004.

[2] E. Raab, M. Prentiss, A. Cable, S. Chu, and D. E. Pritchard, "Trapping of neutral sodium atoms with radiation pressure," *Physical Review Letters* **59**(23), p. 2631, 1987.

[3] M. H. Anderson, J. R. Ensher, M. R. Matthews, C. E. Wieman, and E. A. Cornell, "Observation of bose-einstein condensation in a dilute atomic vapor," *science* **269**(5221), pp. 198–201, 1995.

[4] K. B. Davis, M.-O. Mewes, M. R. Andrews, N. Van Druten, D. Durfee, D. Kurn, and W. Ketterle, "Bose-einstein condensation in a gas of sodium atoms," *Physical review letters* **75**(22), p. 3969, 1995.

[5] B. DeMarco and D. S. Jin, "Onset of fermi degeneracy in a trapped atomic gas," *Science* **285**(5434), pp. 1703–1706, 1999.

[6] B. Regan, E. D. Commins, C. J. Schmidt, and D. DeMille, "New limit on the electron electric dipole moment," *Physical review letters* **88**(7), p. 071805, 2002.

[7] T. W. Hänsch, J. Alnis, P. Fendel, M. Fischer, C. Gohle, M. Herrmann, R. Holzwarth, N. Kolachevsky, T. Udem, and M. Zimmermann, "Precision spectroscopy of hydrogen and femtosecond laser frequency combs," *Philosophical Transactions of the Royal Society of London A: Mathematical, Physical and Engineering Sciences* **363**(1834), pp. 2155–2163, 2005.

[8] C. Wood, S. Bennett, D. Cho, B. Masterson, J. Roberts, C. Tanner, and C. Wieman, "Measurement of parity nonconservation and an anapole moment in cesium," *Science* **275**(5307), pp. 1759–1763, 1997.

[9] J. Simon, W. S. Bakr, R. Ma, M. E. Tai, P. M. Preiss, and M. Greiner, "Quantum simulation of antiferromagnetic spin chains in an optical lattice," *Nature* **472**(7343), pp. 307–312, 2011.

[10] I. Bloch, J. Dalibard, and S. Nascimbène, "Quantum simulations with ultracold quantum gases," *Nature Physics* **8**(4), pp. 267–276, 2012.

[11] M. Greiner, C. A. Regal, and D. S. Jin, "Emergence of a molecular bose–einstein condensate from a fermi gas," *Nature* **426**(6966), pp. 537–540, 2003.

[12] S. Taie, R. Yamazaki, S. Sugawa, and Y. Takahashi, "An su (6) mott insulator of an atomic fermi gas realized by large-spin pomeranchuk cooling," *Nature Physics* **8**(11), pp. 825–830, 2012.

[13] T. Kraemer, M. Mark, P. Waldburger, J. Danzl, C. Chin, B. Engeser, A. Lange, K. Pilch, A. Jaakkola, H.-C. Nägerl, *et al.*, "Evidence for efimov quantum states in an ultracold gas of caesium atoms," *Nature* **440**(7082), pp. 315–318, 2006.

[14] J. McKeever, A. Boca, A. Boozer, R. Miller, J. Buck, A. Kuzmich, and H. Kimble, "Deterministic generation of single photons from one atom trapped in a cavity," *Science* **303**(5666), pp. 1992–1994, 2004.

[15] T. Nicholson, S. Campbell, R. Hutson, G. Marti, B. Bloom, R. McNally, W. Zhang, M. Barrett, M. Safronova, G. Strouse, *et al.*, "Systematic evaluation of an atomic clock at 2 [times] 10-18 total uncertainty," *Nature communications* **6**, 2015.

[16] A. D. Ludlow, M. M. Boyd, J. Ye, E. Peik, and P. O. Schmidt, "Optical atomic clocks," *Rev. Mod. Phys.* **87**, pp. 637–701, Jun 2015.

[17] T. Gustavson, P. Bouyer, and M. Kasevich, "Precision rotation measurements with an atom interferometer gyroscope," *Physical Review Letters* **78**(11), p. 2046, 1997.

[18] L. D. Carr, D. DeMille, R. V. Krems, and J. Ye, "Cold and ultracold molecules: science, technology and applications," *New Journal of Physics* **11**(5), p. 055049, 2009.

[19] J. Baron, W. C. Campbell, D. DeMille, J. M. Doyle, G. Gabrielse, Y. V. Gurevich, P. W. Hess, N. R. Hutzler, E. Kirilov, I. Kozyryev, *et al.*, "Order of magnitude smaller limit on the electric dipole moment of the electron," *Science* **343**(6168), pp. 269–272, 2014.

[20] D. DeMille, S. Cahn, D. Murphree, D. Rahmlow, and M. Kozlov, "Using molecules to measure nuclear spin-dependent parity violation," *Physical review letters* **100**(2), p. 023003, 2008.

[21] A. Micheli, G. Brennen, and P. Zoller, "A toolbox for lattice-spin models with polar molecules," *Nature Physics* **2**(5), pp. 341–347, 2006.

[22] D. DeMille, "Quantum computation with trapped polar molecules," *Physical Review Letters* **88**(6), p. 067901, 2002.

[23] A. André, D. DeMille, J. M. Doyle, M. D. Lukin, S. E. Maxwell, P. Rabl, R. J. Schoelkopf, and P. Zoller, "A coherent all-electrical interface between polar molecules and mesoscopic superconducting resonators," *Nature Physics* **2**(9), pp. 636–642, 2006.

[24] K.-K. Ni, S. Ospelkaus, M. De Miranda, A. Pe'er, B. Neyenhuis, J. Zirbel, S. Kotochigova, P. Julienne, D. Jin, and J. Ye, "A high phase-space-density gas of polar molecules," *science* **322**(5899), pp. 231–235, 2008.

[25] J. W. Park, S. A. Will, and M. W. Zwierlein, "Ultracold dipolar gas of fermionic na 23 k 40 molecules in their absolute ground state," *Physical Review Letters* **114**(20), p. 205302, 2015.

[26] E. Shuman, J. Barry, and D. DeMille, "Laser cooling of a diatomic molecule," *Nature* **467**(7317), pp. 820–823, 2010.

[27] J. Barry, D. McCarron, E. Norrgard, M. Steinecker, and D. DeMille, "Magneto-optical trapping of a diatomic molecule," *Nature* **512**(7514), pp. 286–289, 2014.

[28] B. K. Stuhl, M. T. Hummon, M. Yeo, G. Quéméner, J. L. Bohn, and J. Ye, "Evaporative cooling of the dipolar hydroxyl radical," *Nature* **492**(7429), pp. 396–400, 2012.

[29] C. Bruzewicz, M. Gustavsson, T. Shimasaki, and D. DeMille, "Continuous formation of vibronic ground state rbcs molecules via photoassociation," *New Journal of Physics* **16**(2), p. 023018, 2014.

[30] Y.-P. Chang, D. A. Horke, S. Trippel, and J. Kupper, "Spatially-controlled complex molecules and their applications," *arXiv:1505.05632v2 [physics.chem-ph]* , 2015.

[31] D. Levy, "Laser Spectroscopy of Cold gas-phase Molecules," *Annual Review of Physical Chemistry* **31**, pp. 197–225, 1980.

[32] T. J. Balle and W. H. Flygare, "Fabry-Perot cavity pulsed Fourier transform microwave spectrometer with a pulsed nozzle particle source," *Review of Scientific Instruments* **52**(1), p. 33, 1981.

[33] D. Patterson, E. Tsikata, and J. M. Doyle, "Cooling and collisions of large gas phase molecules," *Physical Chemistry Chemical Physics* **12**(33), p. 9736, 2010.

[34] M. Zeppenfeld, B. G. Englert, R. Glöckner, A. Prehn, M. Mielenz, C. Sommer, L. D. van Buuren, M. Motsch, and G. Rempe, "Sisyphus cooling of electrically trapped polyatomic molecules," *Nature* **491**(7425), pp. 570–573, 2012.

[35] I. Kozyryev, L. Baum, K. Matsuda, P. Olson, B. Hemmerling, and J. M. Doyle, "Collisional relaxation of vibrational states of SrOH with He at 2 K," *New Journal of Physics* **17**(4), p. 045003, 2015.

[36] W. C. Campbell and J. M. Doyle, "Cooling, trap loading, and beam production using a cryogenic helium buffer gas.," in *Cold Molecules: Theory, Experiment, Applications*, R. V. Krems, W. C. Stwalley, and B. Friedrich, eds., ch. 13, pp. 474–504, CRC Press, Boca Raton, 2009.

[37] S. C. Doret, C. B. Connolly, W. Ketterle, and J. M. Doyle, "Buffer-gas cooled bose-einstein condensate," *Physical review letters* **103**(10), p. 103005, 2009.

[38] N. R. Hutzler, H.-I. Lu, and J. M. Doyle, "The buffer gas beam: An intense, cold, and slow source for atoms and molecules," *Chemical reviews* **112**(9), pp. 4803–4827, 2012.

[39] D. Patterson and J. M. Doyle, "A slow, continuous beam of cold benzonitrile," *Physical Chemistry Chemical Physics* **17**(7), pp. 5372–5375, 2015.

[40] H.-I. Lu, I. Kozyryev, B. Hemmerling, J. Piskorski, and J. M. Doyle, "Magnetic trapping of molecules via optical loading and magnetic slowing," *Physical review letters* **112**(11), p. 113006, 2014.

[41] P. v. d. S. Harold J. Metcalf, *Laser Cooling and Trapping*, Springer, 1999.

[42] D. Wineland and H. Dehmelt, "Proposed 1014 delta upsilon less than upsilon laser fluorescence spectroscopy on t1+ mono-ion oscillator iii," in *Bulletin of the American Physical Society*, **20**(4), pp. 637–637, AMER INST PHYSICS CIRCULATION FULFILLMENT DIV, 500 SUNNYSIDE BLVD, WOODBURY, NY 11797-2999, 1975.

[43] T. W. Hänsch and A. L. Schawlow, "Cooling of gases by laser radiation," *Optics Communications* **13**(1), pp. 68–69, 1975.

[44] J. V. Prodan, W. D. Phillips, and H. Metcalf, "Laser production of a very slow monoenergetic atomic beam," *Physical Review Letters* **49**(16), p. 1149, 1982.

[45] J. Prodan, A. Migdall, W. D. Phillips, I. So, H. Metcalf, and J. Dalibard, "Stopping atoms with laser light," *Physical review letters* **54**(10), p. 992, 1985.

[46] S. Chu, L. Hollberg, J. E. Bjorkholm, A. Cable, and A. Ashkin, "Three-dimensional viscous confinement and cooling of atoms by resonance radiation pressure," *Physical Review Letters* **55**(1), p. 48, 1985.

[47] A. L. Migdall, J. V. Prodan, W. D. Phillips, T. H. Bergeman, and H. J. Metcalf, "First observation of magnetically trapped neutral atoms," *Physical Review Letters* **54**(24), p. 2596, 1985.

[48] K. Honda, Y. Takahashi, T. Kuwamoto, M. Fujimoto, K. Toyoda, K. Ishikawa, and T. Yabuzaki, "Magneto-optical trapping of yb atoms and a limit on the branching ratio of the 1 p 1 state," *Physical Review A* **59**(2), p. R934, 1999.

[49] C. Bradley, J. McClelland, W. Anderson, and R. Celotta, "Magneto-optical trapping of chromium atoms," *Physical Review A* **61**(5), p. 053407, 2000.

[50] A. Griesmaier, J. Werner, S. Hensler, J. Stuhler, and T. Pfau, "Bose-einstein condensation of chromium," *Physical Review Letters* **94**(16), p. 160401, 2005.

[51] D. Sukachev, A. Sokolov, K. Chebakov, A. Akimov, S. Kanorsky, N. Kolachevsky, and V. Sorokin, "Magneto-optical trap for thulium atoms," *Physical Review A* **82**(1), p. 011405, 2010.

[52] J. McClelland and J. Hanssen, "Laser cooling without repumping: a magneto-optical trap for erbium atoms," *Physical review letters* **96**(14), p. 143005, 2006.

[53] A. Frisch, K. Aikawa, M. Mark, A. Rietzler, J. Schindler, E. Zupanič, R. Grimm, and F. Ferlaino, "Narrow-line magneto-optical trap for erbium," *Physical Review A* **85**(5), p. 051401, 2012.

[54] M. Lu, S. H. Youn, and B. L. Lev, "Trapping ultracold dysprosium: a highly magnetic gas for dipolar physics," *Physical review letters* **104**(6), p. 063001, 2010.

[55] J. Stuhler, A. Griesmaier, T. Koch, M. Fattori, T. Pfau, S. Giovanazzi, P. Pedri, and L. Santos, "Observation of dipole-dipole interaction in a degenerate quantum gas," *Physical Review Letters* **95**(15), p. 150406, 2005.

[56] S. Sugawa, K. Inaba, S. Taie, R. Yamazaki, M. Yamashita, and Y. Takahashi, "Interaction and filling-induced quantum phases of dual mott insulators of bosons and fermions," *Nature Physics* **7**(8), pp. 642–648, 2011.

[57] S. Sugawa, S. Taie, Y. Takasu, R. Yamazaki, S. Uetake, and Y. Takahashi, "Quantum simulation using ultracold two-electron atoms in an optical lattice," *JOURNAL OF THE KOREAN PHYSICAL SOCIETY* **59**(4), pp. 2936–2940, 2011.

[58] M. Cazalilla, A. Ho, and M. Ueda, "Ultracold gases of ytterbium: Ferromagnetism and mott states in an su (6) fermi system," *New Journal of Physics* **11**(10), p. 103033, 2009.

[59] R. J. Ralchenko Y, Kramida A and N. A. Team, "2013 nist atomic spectra database (version 4.0)," 2013. accessed 30 Apr 2014 14:05:57 EDT.

[60] G. Nave, "Atomic transition rates for neutral holmium (hoi)," *JOSA B* **20**(10), pp. 2193–2202, 2003.

[61] W. Childs, D. R. Cok, and L. Goodman, "New line classifications in ho i based on high-precision hyperfine-structure measurement of low levels," *JOSA* **73**(2), pp. 151–155, 1983.

[62] D. Patterson and J. M. Doyle, "Bright, guided molecular beam with hydrodynamic enhancement," *The Journal of chemical physics* **126**(15), p. 154307, 2007.

[63] J. Barry, E. Shuman, E. Norrgard, and D. DeMille, "Laser radiation pressure slowing of a molecular beam," *Physical review letters* **108**(10), p. 103002, 2012.

[64] M. T. Hummon, M. Yeo, B. K. Stuhl, A. L. Collopy, Y. Xia, and J. Ye, "2d magneto-optical trapping of diatomic molecules," *Phys. Rev. Lett.* **110**, p. 143001, Apr 2013.

[65] V. Zhelyazkova, A. Cournol, T. Wall, A. Matsushima, J. Hudson, E. Hinds, M. Tarbutt, and B. Sauer, "Laser cooling and slowing of caf molecules," *Physical Review A* **89**(5), p. 053416, 2014.

[66] H.-I. Lu, J. Rasmussen, M. J. Wright, D. Patterson, and J. M. Doyle, "A cold and slow molecular beam," *Physical Chemistry Chemical Physics* **13**(42), pp. 18986–18990, 2011.

[67] C. Chen, Y. Li, K. Bailey, T. O'Connor, L. Young, and Z.-T. Lu, "Ultrasensitive isotope trace analyses with a magneto-optical trap," *Science* **286**(5442), pp. 1139–1141, 1999.

[68]

[69] C. Cheng, W. Jiang, G. Yang, Y. Sun, H. Pan, Y. Gao, A. Liu, and S. Hu, "An efficient magneto-optical trap of metastable krypton atoms," *Review of Scientific Instruments* **81**(12), p. 123106, 2010.

[70] J. Schoser, A. Batär, R. Löw, V. Schweikhard, A. Grabowski, Y. B. Ovchinnikov, and T. Pfau, "Intense source of cold rb atoms from a pure two-dimensional magneto-optical trap," *Phys. Rev. A* **66**, p. 023410, Aug 2002.

[71] J. Miao, J. Hostetter, G. Stratis, and M. Saffman, "Magneto-optical trapping of holmium atoms," *Physical Review A* **89**(4), p. 041401, 2014.

[72] J. M. Brown and A. Carrington, *Rotational Spectroscopy of Diatomic Molecules*, Cambridge Molecular Science, Cambridge University Press, 2003.

[73] M. Di Rosa, "Laser-cooling molecules," *The European Physical Journal D-Atomic, Molecular, Optical and Plasma Physics* **31**(2), pp. 395–402, 2004.

[74] T. Tscherbul, J. Kłos, and A. Buchachenko, "Ultracold spin-polarized mixtures of 2 σ molecules with s-state atoms: Collisional stability and implications for sympathetic cooling," *Physical Review A* **84**(4), p. 040701, 2011.

[75] V. Singh, K. S. Hardman, N. Tariq, M.-J. Lu, A. Ellis, M. J. Morrison, and J. D. Weinstein, "Chemical reactions of atomic lithium and molecular calcium monohydride at 1 k," *Physical review letters* **108**(20), p. 203201, 2012.

[76] W. Childs, L. Goodman, U. Nielsen, and V. Pfeufer, "Electric-dipole moment of caf (x $2\sigma+$) by molecular beam, laser-rf, double-resonance study of stark splittings," *The Journal of chemical physics* **80**(6), pp. 2283–2287, 1984.

[77] G. Herzberg, *The spectra and structures of simple free radicals*, Dover, 1971.

[78] T. Wall, J. Kanem, J. Hudson, B. Sauer, D. Cho, M. Boshier, E. Hinds, and M. Tarbutt, "Lifetime of the a (v= 0) state and franck-condon factor of the a- x (0- 0) transition of caf measured by the saturation of laser-induced fluorescence," *Physical Review A* **78**(6), p. 062509, 2008.

[79] M. Dulick, P. F. Bernath, and R. W. Field, "Rotational and vibrational analysis of the caf b$2\sigma+$-x $2\sigma+$ system," *Canadian Journal of Physics* **58**(5), pp. 703–712, 1980.

[80] M. Pelegrini, C. S. Vivacqua, O. Roberto-Neto, F. R. Ornellas, and F. B. Machado, "Radiative transition probabilities and lifetimes for the band systems a^2pi-x^2sigma+ of the isovalent molecules bef, mgf and caf," *Brazilian journal of physics* **35**(4A), pp. 950–956, 2005.

[81] F. Charron, B. Guo, K. Zhang, Z. Morbi, and P. Bernath, "High-resolution infrared emission spectrum of caf," *Journal of Molecular Spectroscopy* **171**(1), pp. 160–168, 1995.

[82] L. A. Kaledin, J. C. Bloch, M. C. McCarthy, and R. W. Field, "Analysis and deperturbation of the a 2 π and b 2 $\sigma+$ states of caf," *Journal of molecular spectroscopy* **197**(2), pp. 289–296, 1999.

[83] W. Childs, G. Goodman, and L. Goodman, "Precise determination of the v and n dependence of the spin-rotation and hyperfine interactions in the caf x2σ12 ground state," *Journal of Molecular Spectroscopy* **86**(2), pp. 365–392, 1981.

[84] D. Berkeland and M. Boshier, "Destabilization of dark states and optical spectroscopy in zeeman-degenerate atomic systems," *Physical Review A* **65**(3), p. 033413, 2002.

[85] C. Gittins, N. Harris, R. Field, J. Verges, C. Effantin, A. Bernard, J. Dincan, W. Ernst, P. Bundgen, and B. Engels, "Analysis and deperturbation of the c 2 π and d 2 σ+ states of caf," *Journal of molecular spectroscopy* **161**(1), pp. 303–311, 1993.

[86] M. Prentiss, E. Raab, D. Pritchard, A. Cable, J. Bjorkholm, and S. Chu, "Atomic-density-dependent losses in an optical trap," *Optics letters* **13**(6), pp. 452–454, 1988.

[87] D. Boiron, A. Michaud, P. Lemonde, Y. Castin, C. Salomon, S. Weyers, K. Szymaniec, L. Cognet, and A. Clairon, "Laser cooling of cesium atoms in gray optical molasses down to 1.1 μk," *Physical Review A* **53**(6), p. R3734, 1996.

[88] J. Flemming, A. Tuboy, D. Milori, L. Marcassa, S. Zilio, and V. Bagnato, "Magneto-optical trap for sodium atoms operating on the d 1 line," *Optics communications* **135**(4), pp. 269–272, 1997.

[89] M. Harvey and A. J. Murray, "Cold atom trap with zero residual magnetic field: The ac magneto-optical trap," *Physical review letters* **101**(17), p. 173201, 2008.

[90] D. Patterson and J. M. Doyle, "Cooling molecules in a cell for FTMW spectroscopy," *Molecular Physics* **110**(15-16), pp. 1757–1766, 2012.

[91] H. Ball, M. Lee, S. Gensemer, and M. Biercuk, "A high-power 626 nm diode laser system for beryllium ion trapping," *Review of Scientific Instruments* **84**(6), p. 063107, 2013.

[92] L. Ricci, M. Weidemüller, T. Esslinger, A. Hemmerich, C. Zimmermann, V. Vuletic, W. König, and T. W. Hänsch, "A compact grating-stabilized diode laser system for atomic physics," *Optics Communications* **117**(5), pp. 541–549, 1995.

[93] W. Ketterle, A. Martin, M. A. Joffe, and D. E. Pritchard, "Slowing and cooling atoms in isotropic laser light," *Physical review letters* **69**(17), p. 2483, 1992.

[94] R. W. Boyd, *Nonlinear Optics*, Academic Press, 2nd edition ed., 2003.

[95] M. Aspelmeyer, P. Meystre, and K. Schwab, "Quantum optomechanics," *Physics Today* **65**(7), pp. 29–35, 2012.

[96] J. Chan, T. M. Alegre, A. H. Safavi-Naeini, J. T. Hill, A. Krause, S. Gröblacher, M. Aspelmeyer, and O. Painter, "Laser cooling of a nanomechanical oscillator into its quantum ground state," *Nature* **478**(7367), pp. 89–92, 2011.

[97] I. Pikovski, M. R. Vanner, M. Aspelmeyer, M. Kim, and Č. Brukner, "Probing planck-scale physics with quantum optics," *Nature Physics* **8**(5), pp. 393–397, 2012.

[98] S. Gerlich, S. Eibenberger, M. Tomandl, S. Nimmrichter, K. Hornberger, P. J. Fagan, J. Tüxen, M. Mayor, and M. Arndt, "Quantum interference of large organic molecules," *Nature communications* **2**, p. 263, 2011.

[99] C. H. Townes and A. L. Schawlow, *Microwave spectroscopy*, Courier Corporation, 2013.

[100] J. R. A. Moreno, T. R. Huet, and J. J. L. González, "Conformational relaxation of S-(+)-carvone and R-(+)-limonene studied by microwave Fourier transform spectroscopy and quantum chemical calculations," *Structural Chemistry* **24**, pp. 1163–1170, oct 2012.

[101] M. Mineyama and T. Egawa, "Conformational property of carvone as studied by laser-jet spectroscopy and theoretical calculations," *Journal of molecular structure* **734**(1), pp. 61–65, 2005.

[102] B. Yan, S. A. Moses, B. Gadway, J. P. Covey, K. R. Hazzard, A. M. Rey, D. S. Jin, and J. Ye, "Observation of dipolar spin-exchange interactions with lattice-confined polar molecules," *Nature* **501**(7468), pp. 521–525, 2013.

[103] A. Prehn, M. Ibrügger, R. Glöckner, G. Rempe, and M. Zeppenfeld, "Direct cooling of polar molecules to sub-millikelvin temperatures," *arXiv preprint arXiv:1511.09427* , 2015.

[104] J. Maze, J. Taylor, and M. Lukin, "Electron spin decoherence of single nitrogen-vacancy defects in diamond," *Physical Review B* **78**(9), p. 094303, 2008.

[105] N. A. Gershenfeld and I. L. Chuang, "Bulk spin-resonance quantum computation," *science* **275**(5298), pp. 350–356, 1997.

[106] I. L. Chuang, L. M. Vandersypen, X. Zhou, D. W. Leung, and S. Lloyd, "Experimental realization of a quantum algorithm," *Nature* **393**(6681), pp. 143–146, 1998.

[107] E. Peik and C. Tamm, "Nuclear laser spectroscopy of the 3.5 ev transition in th-229," *EPL (Europhysics Letters)* **61**(2), p. 181, 2003.

[108] I. W. Smith, I. R. Sims, B. R. Rowe, and B. Rowe, "Gas-phase reactions at low temperatures: Towards absolute zero," *Chemistry-a European Journal* **3**(12), pp. 1925–1928, 1997.

[109] D. R. Herschbach, "Reactive collisions in crossed molecular beams," *Discussions of the Faraday Society* **33**, pp. 149–161, 1962.

[110] A. Henson, S. Gersten, Y. Shagam, J. Narevicius, and E. Narevicius, "Observation of resonances in penning ionization reactions at sub-kelvin temperatures in merged beams," *Science* **338**(6104), pp. 234–238, 2012.

[111] J. Kupper, F. Filsinger, and G. Meijer, "Manipulating the motion of large neutral molecules," *Faraday Discussions* **142**, pp. 155–173, 2009.

[112] B. C. Sawyer, B. K. Stuhl, M. Yeo, T. V. Tscherbul, M. T. Hummon, Y. Xia, J. Kłos, D. Patterson, J. M. Doyle, and J. Ye, "Cold heteromolecular dipolar collisions," *Physical chemistry chemical physics* **13**(42), pp. 19059–19066, 2011.

[113] E. Narevicius and M. G. Raizen, "Toward cold chemistry with magnetically decelerated supersonic beams," *Chemical reviews* **112**(9), pp. 4879–4889, 2012.

[114] C. a. Royer, "Probing protein folding and conformational transitions with fluorescence," *Chemical Reviews* **106**(5), pp. 1769–1784, 2006.

[115] M. S. de Vries and P. Hobza, "Gas-Phase Spectroscopy of Biomolecular Building Blocks," *Annual Review of Physical Chemistry* **58**(1), pp. 585–612, 2007.

[116] R. T. Jongma, M. G. Boogaarts, I. Holleman, and G. Meijer, "Trace gas detection with cavity ring down spectroscopy," *Review of scientific instruments* **66**(4), pp. 2821–2828, 1995.

[117] M. J. Thorpe, K. D. Moll, R. J. Jones, B. Safdi, and J. Ye, "Broadband cavity ringdown spectroscopy for sensitive and rapid molecular detection," *Science* **311**(5767), pp. 1595–1599, 2006.

[118] K. Ledingham and R. Singhal, "High intensity laser mass spectrometry-a review," *International journal of mass spectrometry and ion processes* **163**(3), pp. 149–168, 1997.

[119] K. Norrish and B. W. Chappell, "X-ray fluorescence spectrometry," in *Physical methods in determinative mineralogy*, pp. 201–272, Academic Press London, 1977.

[120] R. A. Hites, "Gas chromatography mass spectrometry," *Handbook of instrumental techniques for analytical chemistry* , pp. 609–626, 1997.

[121] G. G. Brown, B. C. Dian, K. O. Douglass, S. M. Geyer, S. T. Shipman, and B. H. Pate, "A broadband fourier transform microwave spectrometer based on chirped pulse excitation," *Review of Scientific Instruments* **79**(5), p. 053103, 2008.

[122] C. Pérez, M. T. Muckle, D. P. Zaleski, N. A. Seifert, B. Temelso, G. C. Shields, Z. Kisiel, and B. H. Pate, "Structures of cage, prism, and book isomers of water hexamer from broadband rotational spectroscopy," *Science* **336**(6083), pp. 897–901, 2012.

[123] D. Patterson, M. Schnell, and J. M. Doyle, "Enantiomer-specific detection of chiral molecules via microwave spectroscopy," *Nature* **497**(7450), pp. 475–477, 2013.

[124] F. b. Lovas, D. Plusquellic, B. Pate, J. Neill, M. Muckle, and A. c. Remijan, "Microwave spectrum of 1,2-propanediol," *Journal of Molecular Spectroscopy* **257**(1), pp. 82–93, 2009.

[125] P. R. Schreiner, H. P. Reisenauer, D. Ley, D. Gerbig, C.-H. Wu, and W. D. Allen, "Methylhydroxycarbene: Tunneling control of a chemical reaction," *Science* **332**(6035), pp. 1300–1303, 2011.

[126] P. Felder and H. Gunthard, "Freezing of Internal Rotation Temperature In A Supersonic Jet Detected By Matrix IR Spectroscopy," *Chem. Phys. Lett.* **66**(2), pp. 283–286, 1979.

[127] J. P. Toennies and A. F. Vilesov, "Superfluid helium droplets: A uniquely cold nanomatrix for molecules and molecular complexes," *Angewandte Chemie International Edition* **43**(20), pp. 2622–2648, 2004.

[128] M. Sanz, S. Blanco, J. López, and J. Alonso, "Rotational Probes of Six Conformers of Neutral Cysteine," *Angewandte Chemie International Edition* **47**(33), pp. 6216–6220, 2008.

[129] M. Alauddin, E. Gloaguen, V. Brenner, B. Tardivel, M. Mons, A. Zehnacker-Rentien, V. Declerck, and D. J. Aitken, "Intrinsic Folding Proclivities in Cyclic β-Peptide Building Blocks: Configuration and Heteroatom Effects Analyzed by Conformer-Selective Spectroscopy and Quantum Chemistry," *Chemistry - A European Journal* **21**(46), pp. 16479–16493, 2015.

[130] C.-M. Chang, Y.-G. Lau, J.-C. Tsai, and W.-T. Juan, "Relaxation of DNA on a supported lipid membrane," *Chem. Phys. Lett.* **113**(4), p. 48008, 2012.

[131] J. L. Alonso, M. a. Lozoya, I. Peña, J. C. López, C. Cabezas, S. Mata, and S. Blanco, "The conformational behaviour of free d-glucose at last," *Chemical Science* **5**(2), p. 515, 2014.

[132] H. B. Mayes, L. J. Broadbelt, and G. T. Beckham, "How sugars pucker: electronic structure calculations map the kinetic landscape of five biologically paramount monosaccharides and their implications for enzymatic catalysis," *Journal of the American Chemical Society* **136**(3), pp. 1008–1022, 2014.

[133] Y.-P. Chang, K. Dlugolecki, J. Küpper, D. Rösch, D. Wild, and S. Willitsch, "Specific chemical reactivities of spatially separated 3-aminophenol conformers with cold Ca+ ions.," *Science (New York, N.Y.)* **342**(6154), pp. 98–101, 2013.

[134] I. D. Reva, A. M. Plokhotnichenko, S. G. Stepanian, A. Y. Ivanov, E. D. Radchenko, G. G. Sheina, and Y. P. Blagoi, "The rotamerization of conformers of glycine isolated in inert gas matrices. an infrared spectroscopic study," *Chemical physics letters* **232**(1), pp. 141–148, 1995.

[135] H. Ihee, V. a. Lobastov, U. M. Gomez, B. M. Goodson, R. Srinivasan, C. Y. Ruan, and A. H. Zewail, "Direct imaging of transient molecular structures with ultrafast diffraction.," *Science* **291**(5503), pp. 458–462, 2001.

[136] A. G. Csaszar, "Conformers of gaseous glycine," *Journal of the American Chemical society* **114**(24), pp. 9568–9575, 1992.

[137] P. D. Godfrey, R. D. Brown, and F. M. Rodgers, "The missing conformers of glycine and alanine: relaxation in seeded supersonic jets," *Journal of molecular structure* **376**(1), pp. 65–81, 1996.

[138] G. M. Chaban, J. O. Jung, and R. B. Gerber, "Anharmonic vibrational spectroscopy of glycine: Testing of ab initio and empirical potentials," *The Journal of Physical Chemistry A* **104**(44), pp. 10035–10044, 2000.

[139] T. F. Miller Iii and D. C. Clary, "Quantum free energies of the conformers of glycine on an ab initio potential energy surface," *Physical Chemistry Chemical Physics* **6**(10), pp. 2563–2571, 2004.

[140] P. Felder and H. Gunthard, "Conformational Interconversions in Supersonic Jets: Matrix IR Spectroscopy and Model Calculations," *Chemical Physics* **71**, pp. 9–25, 1982.

[141] R. S. Ruoff, T. D. Klots, T. Emilsson, and H. S. Gutowsky, "Relaxation of conformers and isomers in seeded supersonic jets of inert gases," *The Journal of Chemical Physics* **93**(5), pp. 3142–3150, 1990.

[142] B. C. Dian, J. R. Clarkson, and T. S. Zwier, "Direct Measurement of Energy Thresholds to Conformational Isomerization in Tryptamine," *Science* **303**(5661), pp. 1169–1173, 2004.

[143] N. R. Pillsbury, C. W. Müller, W. L. Meerts, D. F. Plusquellic, and T. S. Zwier, "Conformational effects on excitonic interactions in a prototypical H-bonded bichromophore: bis(2-hydroxyphenyl)methane.," *The Journal of Physical Chemistry A* **113**(17), pp. 5000–12, 2009.

[144] J. Piskorski, D. Patterson, S. Eibenberger, and J. M. Doyle, "Cooling, Spectroscopy and Non-Sticking of *trans*-Stilbene and Nile Red," *ChemPhysChem* **15**(17), pp. 3800–3804, 2014.

[145] K. Maussang, D. Egorov, J. S. Helton, S. V. Nguyen, and J. M. Doyle, "Zeeman relaxation of caf in low-temperature collisions with helium," *Physical review letters* **94**(12), p. 123002, 2005.

[146] D. F. Plusquellic, F. J. Lovas, B. H. Pate, J. L. Neill, M. T. Muckle, and A. J. Remijan, "Distinguishing tunneling pathways for two chiral conformer pairs of 1,3-propanediol from the microwave spectrum," *Journal of Physical Chemistry A* **113**, pp. 12911–12918, 2009.

[147] I. D. Reva, A. J. Lopes Jesus, M. T. S. Rosado, R. Fausto, M. Ermelinda Eusébio, and J. S. Redinha, "Stepwise conformational cooling towards a single isomeric state in the four internal rotors system 1,2-butanediol," *Physical Chemistry Chemical Physics* **8**(45), p. 5339, 2006.

[148] PGOPHER. a Program for Simulating Rotational, Vibrational and Electronic Structure, C. M. Western, University of Bristol. http://pgopher.chm.bris.ac.uk.

[149] D. Patterson and J. M. Doyle, "Sensitive chiral analysis via microwave three-wave mixing," *Physical review letters* **111**(2), p. 023008, 2013.

[150] R. Noyori, "Asymmetric catalysis: science and opportunities (nobel lecture)," *Angewandte Chemie International Edition* **41**(12), pp. 2008–2022, 2002.

[151] S. G. Allenmark *et al.*, *Chromatographic enantioseparation*, E. Horwood; Halsted Press, 1988.

[152] Y.-M. Liu, P. Gordon, S. Green, and J. V. Sweedler, "Determination of salsolinol enantiomers by gas chromatography-mass spectrometry with cyclodextrin chiral columns," *Analytica chimica acta* **420**(1), pp. 81–88, 2000.

[153] H. Buschmann, R. Thede, and D. Heller, "New developments in the origins of the homochirality of biologically relevant molecules," *Angewandte Chemie International Edition* **39**(22), pp. 4033–4036, 2000.

[154] M. K. Oberthaler, S. Bernet, E. M. Rasel, J. Schmiedmayer, and A. Zeilinger, "Inertial sensing with classical atomic beams," *Physical Review A* **54**(4), p. 3165, 1996.

[155] S. Aghion, O. Ahlén, C. Amsler, A. Ariga, T. Ariga, A. Belov, K. Berggren, G. Bonomi, P. Bräunig, J. Bremer, *et al.*, "A moiré deflectometer for antimatter," *Nature communications* **5**, 2014.

[156] H. Ulbricht, M. Berninger, S. Deachapunya, A. Stefanov, and M. Arndt, "Gas phase sorting of fullerenes, polypeptides and carbon nanotubes," *Nanotechnology* **19**(4), p. 045502, 2008.

[157] M. Quack, "How important is parity violation for molecular and biomolecular chirality?," *Angewandte Chemie International Edition* **41**(24), pp. 4618–4630, 2002.

[158] C. Daussy, T. Marrel, A. Amy-Klein, C. Nguyen, C. J. Bordé, and C. Chardonnet, "Limit on the parity nonconserving energy difference between the enantiomers of a chiral molecule by laser spectroscopy," *Physical review letters* **83**(8), p. 1554, 1999.

[159] A. Lahamer, S. Mahurin, R. Compton, D. House, J. Laerdahl, M. Lein, and P. Schwerdtfeger, "Search for a parity-violating energy difference between enantiomers of a chiral iron complex," *Physical review letters* **85**(21), p. 4470, 2000.

[160] M. Quack, "Frontiers in spectroscopy," *Faraday discussions* **150**, pp. 533–565, 2011.

[161] B. Darquié, C. Stoeffler, A. Shelkovnikov, C. Daussy, A. Amy-Klein, C. Chardonnet, S. Zrig, L. Guy, J. Crassous, P. Soulard, *et al.*, "Progress toward the first observation of parity violation in chiral molecules by high-resolution laser spectroscopy," *Chirality* **22**(10), pp. 870–884, 2010.

[162] A. Bakasov, T.-K. Ha, and M. Quack, "Ab initio calculation of molecular energies including parity violating interactions," *The Journal of chemical physics* **109**(17), pp. 7263–7285, 1998.

[163] M. Bouchiat and C. Bouchiat, "Weak neutral currents in atomic physics," *Physics Letters B* **48**(2), pp. 111–114, 1974.

[164] C. Stoeffler, B. Darquié, A. Shelkovnikov, C. Daussy, A. Amy-Klein, C. Chardonnet, L. Guy, J. Crassous, T. R. Huet, P. Soulard, *et al.*, "High resolution spectroscopy of methyltrioxorhenium: towards the observation of parity violation in chiral molecules," *Physical Chemistry Chemical Physics* **13**(3), pp. 854–863, 2011.

[165] S. Sickafoose, P. Wikrent, B. Drouin, and S. Kukolich, "Microwave spectra and quadrupole coupling measurements for methyl rhenium trioxide," *Chemical Physics Letters* **263**(1), pp. 191–196, 1996.

[166] C. A. Taatjes, D. E. Shallcross, and C. J. Percival, "Research frontiers in the chemistry of criegee intermediates and tropospheric ozonolysis," *Physical Chemistry Chemical Physics* **16**(5), pp. 1704–1718, 2014.

[167] H. Matthews and W. M. Irvine, "The hydrocarbon ring c3h2 is ubiquitous in the galaxy," *The Astrophysical Journal* **298**, pp. L61–L65, 1985.

[168] S. Yamamoto and S. Saito, "Microwave spectrum and molecular structure of the cyclic c3h radical," *The Journal of chemical physics* **101**(7), pp. 5484–5493, 1994.